

Systems and Protocols for Quantum Metrology and Quantum Computation

A dissertation presented

by

Péter Kómár

to

The Department of Physics

in partial fulfillment of the requirements

for the degree of

Doctor of Philosophy

in the subject of

Physics

Harvard University

Cambridge, Massachusetts

December 2015

©2015 - Péter Kómár

All rights reserved.

Thesis advisor

Mikhail D. Lukin

Author

Péter Kómár

Systems and Protocols for Quantum Metrology and Quantum Computation

Abstract

Abstract about

- Quantum computation protocols
- and their use
- Quantum metrology protocols
- and their use
- systems capable of realizing them
- namely: optomechanical systems
- atomic systems

Contents

Title Page	i
Abstract	iii
Table of Contents	iv
List of Figures	vii
List of Tables	ix
Citations to Previously Published Work	x
Acknowledgments	xi
Dedication	xii
1 Introduction and Motivation	1
1.1 Overview and Structure	1
1.2 Optomechanical Systems	1
1.3 Atom-Cavity Systems	1
1.4 Rydberg Interactions	1
1.5 Quantum Repeaters	1
1.6 Atomic Clocks and Quantum Metrology	1
2 Single-photon nonlinearities in two-mode optomechanics	2
2.1 Introduction	2
2.2 Multimode optomechanics	5
2.3 Equal-time correlations	8
2.3.1 Average transmission and reflection	8
2.3.2 Intensity correlations	11
2.3.3 Absence of two-photon resonance at $\Delta = 0$	14
2.3.4 Finite temperature	16
2.4 Delayed coincidence and single phonon states	21
2.4.1 Driven mode	22
2.4.2 Heralded single phonon states	25
2.5 Reaching strong coupling	28
2.6 Conclusions	29

3 Optomechanical quantum information processing	31
3.1 Introduction	31
3.2 Model	33
3.3 Resonant strong-coupling optomechanics	34
3.4 An OM single-photon source	37
3.5 Single-phonon single-photon transistor	38
3.6 Phonon-phonon interactions	40
3.7 Conclusions	42
4 Heralded Quantum Gates with Integrated Error Detection	43
4.1 Introduction	43
4.2 Heralding gate	45
4.3 Performance	47
4.3.1 Model	47
4.3.2 Effective Hamiltonian	48
4.3.3 Success probability	49
4.3.4 Gate time	50
4.4 Additional errors	51
4.5 Possible implementation	53
4.6 Application	54
4.7 Conclusion	55
5 Remote entanglement distribution using individual atoms in cavities	56
5.1 Introduction	56
5.2 High-fidelity quantum repeater	59
5.2.1 Secret key rate	65
5.2.2 Repeater architecture	67
5.3 Other cavity based repeaters	69
5.3.1 Single-photon entanglement creation	69
5.3.2 Initial purification	71
5.3.3 CNOT gates	73
5.4 Numerical optimization	75
5.5 Conclusion	85
6 Heisenberg-Limited Atom Clocks Based on Entangled Qubits	88
6.1 Introduction	88
7 A quantum network of clocks	89
7.1 Introduction	89
8 Entangling collective Rydberg excitations of remote atomic ensembles	90
8.1 Introduction	90

A Appendices for Chapter 2	91
A.1 Derivation of reflected mode operator	91
A.2 Analytic model	92
B Appendices for Chapter 3	95
B.1 Phonon nonlinearities	95
B.1.1 Model	95
B.1.2 Displaced frame	96
B.1.3 Hybridized modes	97
B.1.4 Adiabatic elimination of the cavity mode	99
B.1.5 Simple perturbation theory	100
B.1.6 Corrections	101
B.1.7 Numerical simulation	102
B.2 Phonon-phonon interactions	104
C Appendices for Chapter 4	107
C.1 Perturbation theory	107
C.1.1 Success probability and fidelity	112
C.1.2 N -qubit Toffoli gate	112
C.1.3 CZ-gate	114
C.1.4 Two-photon driving	116
C.2 Gate time	119
C.3 Numerical simulation	121
C.4 Additional errors	124
D Appendices for Chapter 5	128
D.1 Error analysis of the single-photon scheme	128
D.2 Error analysis of the two-photon scheme	130
D.3 Deterministic CNOT gate	131
D.4 Rate analysis	133
D.4.1 Deterministic gates	136
D.4.2 Probabilistic gates	139
Bibliography	143

List of Figures

2.1	Two-mode optomechanical system	5
2.2	Lower level diagram of 2+1 optomechanical system	7
2.3	Photon statistics in mode anti-symmetric mode, a	9
2.4	Photon statistics in mode symmetric mode, s	10
2.5	Photon statistics in the reflected mode, R	10
2.6	Illustration of dominant processes	13
2.7	Aggregate photon statistics of both modes	16
2.8	Temperature dependence of the relevant levels	17
2.9	Effect of non-zero temperature on photon statistics of mode a	17
2.10	Effect of non-zero temperature on photon statistics of mode s	18
2.11	Autocorrelation of mode a	24
2.12	Autocorrelation of mode s	26
2.13	Diagram with metastable subspace	27
3.1	Model of two resonators	33
3.2	Behavior of the coupled system	35
3.3	A single-phonon single-photon transistor	38
3.4	Controlled phase gate	40
4.1	Level structures of qubit and control atoms	47
4.2	51
4.3	Level structure of auxiliary atom	52
5.1	The general architecture of a quantum repeater	60
5.2	Entanglement generation I	61
5.3	Schematics of the heralded CZ gate	63
5.4	Secret key fraction	66
5.5	Number of swap levels	68
5.6	Purification	72
5.7	CNOT gate structure II	73
5.8	CNOT gates comparison	76

5.9 Example of repeater architecture	78
5.10 Optimal secret key rate I	80
5.11 Optimal secret key rate II	81
B.1 Comparison of effective and exact description	103
C.1 Level structure of qubit an auxiliary atoms	109
C.2 Error and success probability vs cooperativity	115
C.3 Levels structure of auxiliary atom	116
C.4 Gate time and success probability vs driving strength	123
C.5 Conditional fidelity	124
C.6 Gate time and success probability vs detuning	125

List of Tables

5.1	The characteristics of the three gates considered for the cavity-based repeaters. C is the cooperativity of the atom-cavity system and η_d is the single photon detection efficiency in gate 2. The time of the single qubit rotations is assumed to be $10 \mu\text{s}$	75
5.2	Parameters in the numerical optimization	77
C.1	Comparison of CZ and Toffoli gates	108
C.2	Perturbation validity criteria	120

Citations to Previously Published Work

Most of the chapters of this thesis have appeared in print elsewhere. By chapter number, they are:

- Chapter 2: “Single-photon nonlinearities in two-mode optomechanics,” P. Kómár, S. D. Bennett, K. Stannigel, S. J. M. Habraken, P. Rabl, P. Zoller, and M. D. Lukin, *Phys. Rev. A* **87**, 013839 (2013).
- Chapter 3: “Optomechanical quantum information processing,” K. Stannigel, P. Kómár, S. J. M. Habraken, S. D. Bennett, M. D. Lukin, P. Zoller, and P. Rabl, *Phys. Rev. Lett.* **109**, 013603 (2012).
- Chapter 4: “Heralded Quantum Gates with Integrated Error Detection,” J. Borregaard, P. Kómár, E. M. Kessler, A. S. Sørensen, and M. D. Lukin, *Phys. Rev. Lett.* **114**, 110502 (2015).
- Chapter 5: “Remote entanglement distribution using individual atoms in cavities,” J. Borregaard, P. Kómár, E. M. Kessler, A. S. Sørensen, and M. D. Lukin, *Phys. Rev. A* **92**, 012307 (2015).
- Chapter 6: “Heisenberg-Limited Atom Clocks Based on Entangled Qubits,” E. M. Kessler, P. Kómár, M. Bishof, L. Jiang, A. S. Sørensen, J. Ye, and M. D. Lukin, *Phys. Rev. Lett.* **112**, 190403 (2014).
- Chapter 7: “A quantum network of clocks,” P. Kómár, E. M. Kessler, M. Bishof, L. Jiang, A. S. Sørensen, J. Ye, and M. D. Lukin, *Nature Physics* **10**, 582587 (2014).
- Chapter 8: “?Quantum network of netural atom clocks,” P. Kómár, T. Topcu, E. M. Kessler, A. Derevianko, A. S. Sørensen, and M. D. Lukin, ?? ??, ?? (2015?).

Acknowledgments

*Dedicated to my parents Erzsébet and Antal,
my sister Anna,
and my fiancée Szilvia.*

Chapter 1

Introduction and Motivation

1.1 Overview and Structure

1.2 Optomechanical Systems

1.3 Atom-Cavity Systems

1.4 Rydberg Interactions

1.5 Quantum Repeaters

1.6 Atomic Clocks and Quantum Metrology

Chapter 2

Single-photon nonlinearities in two-mode optomechanics

2.1 Introduction

Optomechanical systems (OMSs) involve the interaction between optical and mechanical modes arising from radiation pressure force, canonically in an optical cavity with a movable mirror [45, 57, 3, 33, 29]. Recent progress in optomechanical (OM) cooling techniques has been rapid [60, 34, 2, 46, 20, 81, 95, 101], and experiments have now demonstrated cooling to the mechanical ground state [64, 93, 13], OM induced transparency [100, 78], and coherent photon-phonon conversion [31, 99, 40]. These developments have attracted significant interest, and motivated proposals for applications exploiting OM interactions at the quantum level, ranging from quantum transducers [89, 79, 72, 91] and mechanical storage of light [104, 1, 15] to single-photon sources [69] and OM quantum information processing [88, 82]. Significant

advantages of OM platforms for these applications are the possibility for mass production and on-chip integration using nanofabrication technologies, wide tuneability and the versatility of mechanical oscillators to couple to a wide variety of quantum systems [83].

The force exerted by a single photon on a macroscopic object is typically weak; consequently, experiments have so far focused on the regime of strong optical driving, where the OM interaction is strongly enhanced but effectively linear [37, 92]. However, recent progress in the design of nanoscale OMSs [13, 28, 12, 22] and OM experiments in cold atomic systems [39, 8] suggests that the regime of single-photon strong coupling, where the OM coupling strength g exceeds the optical cavity decay rate κ , is within reach of the next generation of OM experiments. In this regime, the inherently nonlinear OM interaction is significant at the level of single photons and phonons [58, 53, 69, 63]. For example, the presence of a single photon can—via the mechanical mode—strongly influence or even block the transmission of a second photon, leading to photon blockade. This single-photon nonlinearity was recently analyzed for canonical OMSs consisting of a single optical mode coupled to a mechanical mode [69, 49, 52]. However, with a single optical mode, the OM coupling is highly off-resonant, leading to a suppression of effective photon-photon interactions by the large mechanical frequency $\omega_m \gg g$ [69].

In this paper we develop a quantum theory of a weakly driven *two-mode* OMS [61, 88, 54, 4] in which two optical modes are coupled to a mechanical mode. The key advantage of this approach is that photons in the two optical modes can be resonantly exchanged by absorbing or emitting a phonon via three-mode mixing. We

extend our earlier results [88], where we discussed possible applications of resonant optomechanics such as single-photon sources and quantum gates, by exploring one-time and two-time photon correlations of both optical modes. Specifically, we find that the photon-photon correlation function of the undriven optical mode exhibits delayed bunching for long delay times, arising from a heralded single mechanical excitation after detection of a photon in the undriven mode. Finally, we compare the two-mode OMS to the canonical atomic cavity QED system with a similar low-energy level spectrum [11, 7]. Despite several similarities we find that, in stark contrast to the atom-cavity system, the OMS studied here does *not* exhibit nonclassical correlations unless the strict strong coupling condition $g > \kappa$ is met. Our results serve as a guideline for OM experiments nearing the regime of single-photon nonlinearity, and for potential quantum information processing applications with photons and phonons.

The remainder of the paper is organized as follows. In Sec. 2.2, we introduce the system and details of the model. In Sec. 2.3, we calculate the equal-time intensity correlation functions of both transmitted and reflected photons, and discuss signatures of nonclassical photon statistics. In Sec. 2.4, we investigate two-time correlation functions of the transmitted photons, and discuss delayed coincidence correlations that indicate the heralded preparation of a single phonon state. Finally, we provide a brief outlook on the feasibility of strong OM coupling in Sec. 2.5, and conclude in Sec. 2.6 with a summary of our results. Appendix A.2 contains details of our analytic model used to derive several results discussed in the paper.

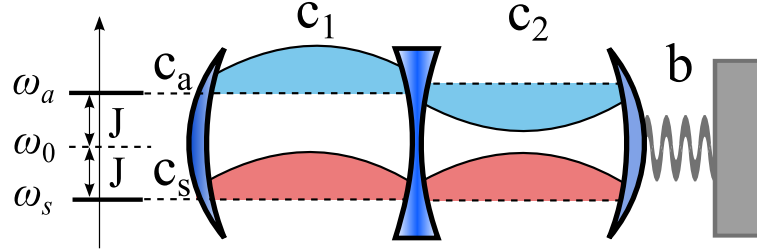


Figure 2.1: Optomechanical system consisting of two tunnel-coupled optical cavity modes c_1 and c_2 , and a mechanical oscillator b coupled to one of the cavity modes by radiation pressure. The coupled optical modes are diagonalized in terms of symmetric and antisymmetric modes, c_s and c_a .

2.2 Multimode optomechanics

We consider the setup shown schematically in Fig. 2.1, consisting of two optical cavities separated by a semitransparent mirror. The cavity modes are coupled by photons tunneling through the fixed mirror in the middle, and the mode on the right couples to the motion of a vibrating endmirror oscillator through radiation pressure. The Hamiltonian describing the system is ($\hbar = 1$)

$$\begin{aligned} H_0 = & \omega_0(c_1^\dagger c_1 + c_2^\dagger c_2) - J(c_1^\dagger c_2 + c_1^\dagger c_2) \\ & + \omega_m b^\dagger b - g(b^\dagger + b)c_2^\dagger c_2 + H_{\text{dr}}(t), \end{aligned} \quad (2.1)$$

where $c_{1,2}$ are annihilation operators for the two cavity modes, which we assume to be degenerate with frequency ω_0 , and J is the photon tunneling amplitude through the central mirror. The motion of the endmirror on the right is described by a single mechanical mode with annihilation operator b and frequency ω_m , and the parametric coupling strength g corresponds to the shift of the cavity frequency due to a single mechanical phonon. Finally, $H_{\text{dr}}(t) = \sum_{i=1,2} (\Omega_i c_i e^{i\omega_L t} + \text{h.c.})$ describes two coherent driving fields of amplitudes Ω_i and frequency ω_L , which are applied to the left and right cavities.

We are interested in a three-mode resonant interaction in which the two optical modes exchange a photon by absorbing or emitting a phonon in the mechanical mode. We begin by diagonalizing the optical part of H_0 in the first line of Eq. 2.1 in terms of the symmetric and antisymmetric combinations of the optical modes, $c_s = \frac{1}{\sqrt{2}}(c_1 + c_2)$ and $c_a = \frac{1}{\sqrt{2}}(c_1 - c_2)$, with eigenfrequencies $\omega_{a,s} = \omega_0 \pm J$. In the frame rotating at the laser frequency ω_L we obtain

$$\begin{aligned} H' = & -\Delta c_a^\dagger c_a - (\Delta + 2J)c_s^\dagger c_s + \omega_m b^\dagger b \\ & + \frac{g}{2} (c_a^\dagger c_s + c_s^\dagger c_a) (b + b^\dagger) + \sum_{\eta=s,a} \Omega_\eta (c_\eta^\dagger + c_\eta), \end{aligned} \quad (2.2)$$

where $\Delta = \omega_L - \omega_a$ is the laser detuning from the c_a mode, and $\Omega_{s,a} = (\Omega_1 \pm \Omega_2)/\sqrt{2}$.

Next, we focus on the case of three-mode resonance, $\omega_m = 2J$, and assume $\omega_m \gg g, |\Delta|, \Omega_i$. The third inequality here corresponds to a weak optical drive, the relevant limit for studying single-photon nonlinear effects in this work. This allows us to make a rotating wave approximation with respect to the remaining large frequency scale ω_m , and in the frame defined by the transformation $U = \exp[-i\omega_m t(b^\dagger b - c_s^\dagger c_s)]$, the Hamiltonian H' simplifies to

$$H = -\Delta(c_a^\dagger c_a + c_s^\dagger c_s) + \frac{g}{2}(c_a^\dagger c_s b + b^\dagger c_s^\dagger c_a) + \Omega_a(c_a^\dagger + c_a). \quad (2.3)$$

This is the starting point for our analysis discussed below. Note that the assumptions made in deriving Eq. (2.3) are fulfilled in most experimental systems of interest [38, 105], and H represents a generic description for resonant two-mode optomechanics [61, 23, 17, 54].

The nonlinear terms proportional to g in Eq. (2.3) describe coherent photon exchange between the two optical modes mediated by absorption or emission of a

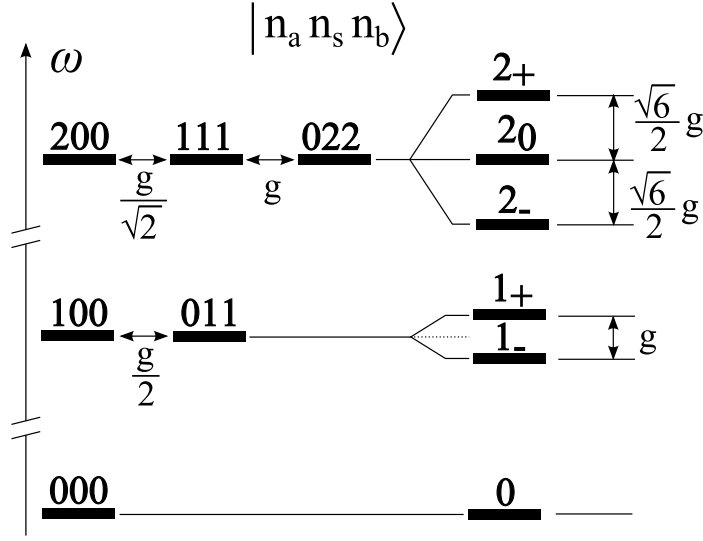


Figure 2.2: Level diagram showing the relevant zero-, one- and two-photon states at zero temperature and under the three-mode resonance condition $\omega_s - \omega_a = \omega_m$. States are labeled by $|n_a n_s n_b\rangle$ denoting the number n_a (n_s) of antisymmetric (symmetric) photons and the number of phonons n_b . The optomechanical coupling g splits the degeneracy of states $|n_a n_s n_b\rangle$ and $|n_a - 1, n_s + 1, n_b + 1\rangle$.

phonon. The resulting low energy level diagram is shown in Fig. 2.2, where $|n_a n_s n_b\rangle$ represents a state with n_a and n_s photons in the c_a and c_s modes, and n_b phonons in the mechanical mode. In the absence of a drive we diagonalize H in this few-photon subspace, yielding the eigenstates

$$|0\rangle = |000\rangle, \quad (2.4)$$

$$|1_{\pm}\rangle = \frac{1}{\sqrt{2}} (|100\rangle \pm |011\rangle), \quad (2.5)$$

$$|2_{\pm}\rangle = \frac{1}{\sqrt{6}} \left(|200\rangle \pm \sqrt{3} |111\rangle + \sqrt{2} |022\rangle \right), \quad (2.6)$$

$$|2_0\rangle = \frac{1}{\sqrt{3}} \left(\sqrt{2} |200\rangle - |022\rangle \right). \quad (2.7)$$

Note that in the diagonal basis the weak driving field couples all states with photon number differing by one. In the following sections we use this low energy Hilbert space to understand photon correlations in the system.

In addition to the coherent evolution modeled by the Hamiltonian H , we describe optical and mechanical dissipation using a master equation for the system density operator ρ ,

$$\dot{\rho} = -i[H, \rho] + \kappa\mathcal{D}[c_a]\rho + \kappa\mathcal{D}[c_s]\rho \quad (2.8)$$

$$+ \frac{\gamma}{2}(N_{\text{th}} + 1)\mathcal{D}[b]\rho + \frac{\gamma}{2}N_{\text{th}}\mathcal{D}[b^\dagger]\rho, \quad (2.9)$$

where H is given by Eq. 2.3, 2κ and γ are energy decay rates for the optical and mechanical modes, respectively, N_{th} is the thermal phonon population and $\mathcal{D}[\hat{o}]\rho = 2\hat{o}\rho\hat{o}^\dagger - \hat{o}^\dagger\hat{o}\rho - \rho\hat{o}^\dagger\hat{o}$. Below we study nonlinear effects at the level of single photons, both numerically and analytically, by solving Eq. 2.8 approximately in the limit of weak optical driving, $\Omega \equiv \Omega_a \ll \kappa$.

2.3 Equal-time correlations

2.3.1 Average transmission and reflection

Before focussing on photon-photon correlations, we first study the average transmission through the cavity, which is proportional to the mean intracavity photon number. In Fig. 2.3 and 2.4 we show the intracavity photon number of the two optical modes,

$$\bar{n}_i = \langle c_i^\dagger c_i \rangle, \quad (2.10)$$

where $i = a, s$, and angle brackets denote the steady state average. At $\Delta/g = \pm\frac{1}{2}$, both transmission curves exhibit a maximum, indicating that the driving field is in resonance with an eigenmode of the system. The position of these peaks can

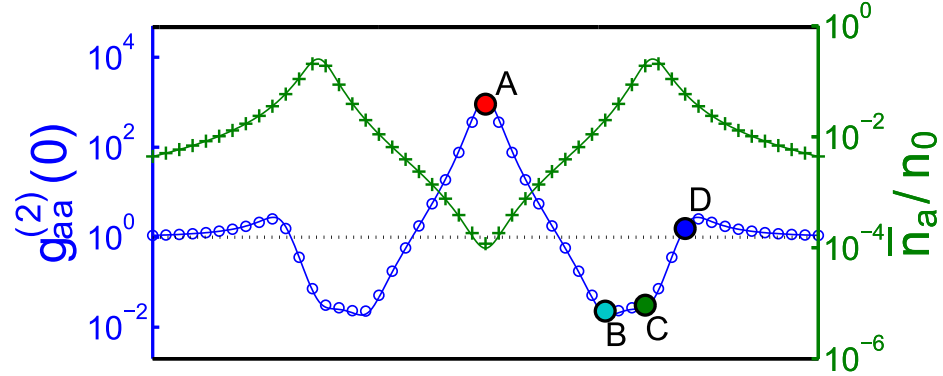


Figure 2.3: Normalized average photon number (green “+”) and photon-photon correlation function (blue “o”) for driven mode c_a as a function of laser detuning at zero temperature. Solid lines are calculated from analytic model (see Eqs. (2.19-2.24)) and points show full numerical calculation. The average photon number is normalized by $n_0 = (\Omega/\kappa)^2$. ($g/\kappa = 20$ and $\gamma/\kappa = 0.2$)

be understood from the level diagram shown in Fig. 2.2, which at finite g shows a splitting of the lowest photonic states into a doublet, $|1_{\pm}\rangle = (|100\rangle \pm |011\rangle)/\sqrt{2}$.

In addition to the transmission, we plot the mean reflected photon number in Fig. 2.5. As discussed below, the reflected photon statistics can also exhibit signatures of nonlinearity. We calculate properties of the reflected light using the annihilation operator $c_R = c_a + i\frac{\Omega}{\kappa}$, obtained from standard input-output relations for a symmetric two-sided cavity (see Appendix A.1). The mean reflected photon number $\bar{n}_R = \langle c_R^\dagger c_R \rangle$ is plotted in Fig. 2.5. At $\Delta/g = \pm\frac{1}{2}$, the average reflection has a minimum where the average transmission has a maximum. Note that in contrast to a single cavity, even on resonance the transmission probability is less than unity and the reflection probability remains finite.

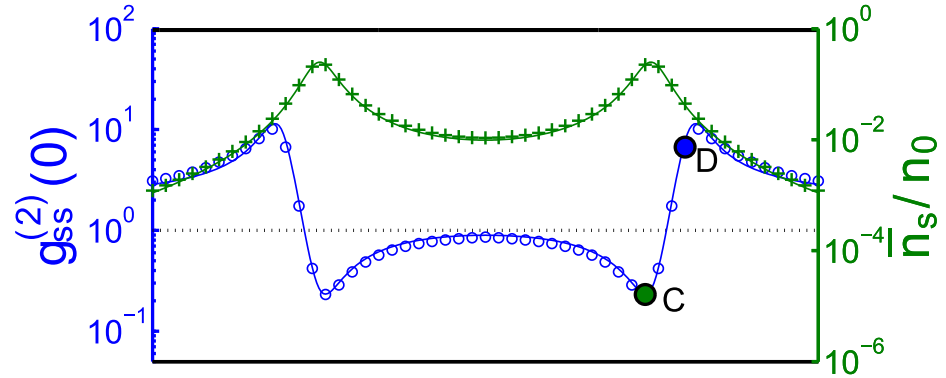


Figure 2.4: Normalized average photon number (green “+”) and photon-photon correlation function (blue “o”) for the undriven mode c_s as a function of laser detuning at zero temperature. Solid lines are calculated from analytic model (see Eqs. (2.19-2.24)) and points show full numerical calculation. The average photon number is normalized by $n_0 = (\Omega/\kappa)^2$. ($g/\kappa = 20$ and $\gamma/\kappa = 0.2$)

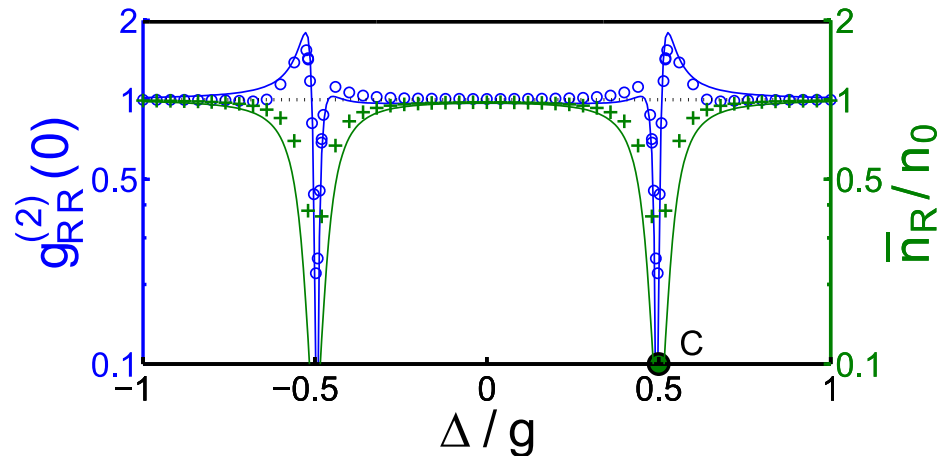


Figure 2.5: Normalized average photon number (green “+”) and photon-photon correlation function (blue “o”) for the reflected field c_R , as a function of laser detuning at zero temperature. Solid lines are calculated from analytic model (see Eqs. (2.19-2.24)) and points show full numerical calculation. The average photon number is normalized by $n_0 = (\Omega/\kappa)^2$. The small discrepancy between the analytic and numerical results is due to the approximation $g/\kappa \gg 1$ to simplify the expressions in Eqs. (2.19-2.24) ($g/\kappa = 20$ and $\gamma/\kappa = 0.2$)

2.3.2 Intensity correlations

To characterize nonclassical photon statistics in the light transmitted through the OMS we study the equal-time photon-photon correlation functions,

$$g_{ii}^{(2)}(0) = \frac{\langle c_i^\dagger c_i^\dagger c_i c_i \rangle}{\langle c_i^\dagger c_i \rangle^2}, \quad (2.11)$$

where all operators are evaluated at the same time and $i = a, s, R$. A normalized correlation of $g_{ii}^{(2)}(0) < 1$ indicates photon anti-bunching, and the limit $g_{ii}^{(2)}(0) \rightarrow 0$ corresponds to the complete photon blockade regime in which two photons never occupy the cavity at the same time. The solid curves show $g_{aa}^{(2)}(0)$ in Fig. 2.3, $g_{ss}^{(2)}(0)$ in Fig. 2.4 and $g_{RR}^{(2)}(0)$ in Fig. 2.5 as a function of the laser detuning and in the limit of weak driving $\Omega/\kappa \ll 1$. The most pronounced features of these correlation functions occur at $|\Delta|/g = 0, \frac{1}{\sqrt{8}}, \frac{1}{2}$ and $\frac{\sqrt{6}}{4}$, as marked by dots A, B, C and D, respectively. As we explain in detail in the following analysis, we find that the photon bunching at A and anti-bunching at B are the result of destructive quantum interference, while the features at points C and D arise from one- and two-photon resonances.

To gain insight into the two photon correlation functions shown in Fig. 2.3, 2.4 and 2.5, we develop an approximate analytic model for the system by considering only the six levels shown in Fig. 2.2. Assuming that the system is initially prepared in $|000\rangle$, these are the only levels significantly populated by weakly driving the c_a mode. We make the ansatz [11]

$$\begin{aligned} |\psi\rangle = & A_{000}|000\rangle + A_{100}|100\rangle + A_{011}|011\rangle \\ & + A_{200}|200\rangle + A_{111}|111\rangle + A_{022}|022\rangle, \end{aligned} \quad (2.12)$$

and describe the dynamics by evolving $|\psi\rangle$ under the action of the non-Hermitian

Hamiltonian, $\tilde{H} = H - i [\kappa c_a^\dagger c_a + \kappa c_s^\dagger c_s + \frac{\gamma}{2} b^\dagger b]$. This approach allows us to evaluate intensities up to order Ω^2 and two-point correlation up to order Ω^4 , since the neglected quantum jumps lead to higher order corrections. By neglecting the typically small mechanical decay rate $\gamma \ll \kappa$, the amplitudes in Eq. 2.12 then satisfy

$$\dot{A}_{000} = 0, \quad (2.13)$$

$$\dot{A}_{100} = -i\frac{g}{2}A_{011} - i\Omega A_{000} - \tilde{\kappa}A_{100}, \quad (2.14)$$

$$\dot{A}_{011} = -i\frac{g}{2}A_{100} - \tilde{\kappa}A_{011}, \quad (2.15)$$

$$\dot{A}_{200} = -i\frac{g}{\sqrt{2}}A_{111} - i\sqrt{2}\Omega A_{100} - 2\tilde{\kappa}A_{200}, \quad (2.16)$$

$$\dot{A}_{111} = -i\frac{g}{\sqrt{2}}A_{200} - igA_{022} - i\Omega A_{011} - 2\tilde{\kappa}A_{111}, \quad (2.17)$$

$$\dot{A}_{022} = -igA_{111} - 2\tilde{\kappa}A_{022}, \quad (2.18)$$

where $\tilde{\kappa} = \kappa - i\Delta$. It is straightforward to solve Eqs. (2.13–2.18) for the steady state amplitudes (see Appendix A.2). To lowest order in Ω/κ the mean occupation numbers are $\bar{n}_a = |\bar{A}_{100}|^2$, $\bar{n}_s = |\bar{A}_{011}|^2$ and $\bar{n}_R = |\bar{A}_{100} + i\Omega/\kappa|^2$, where \bar{A} denote steady state amplitudes. We obtain

$$\frac{\bar{n}_a}{n_0} = \frac{\kappa^2 [R_\kappa(0)]^{1/2}}{R_\kappa(\frac{g}{2})}, \quad (2.19)$$

$$\frac{\bar{n}_s}{n_0} = \frac{g^2 \kappa^2}{4R_\kappa(\frac{g}{2})}, \quad (2.20)$$

$$\frac{\bar{n}_R}{n_0} \approx \frac{[R_{\kappa/2}(\frac{g}{2})]^2}{[R_\kappa(\frac{g}{2})]^2}, \quad (2.21)$$

where $R_K(\omega) = [K^2 + (\Delta - \omega)^2] [K^2 + (\Delta + \omega)^2]$ and $n_0 = (\Omega/\kappa)^2$. From the factors $R_K(\omega)$ in the denominators (numerators) in these expressions, we obtain the positions of the resonances (antiresonances) in the average intracavity photon numbers, in

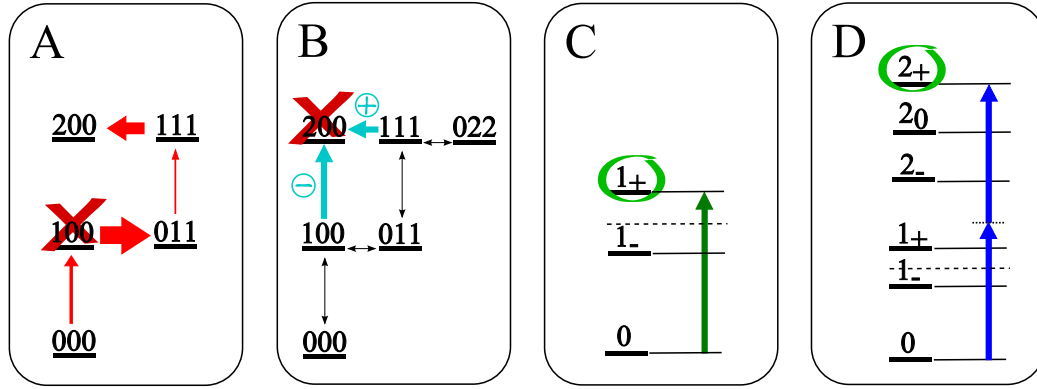


Figure 2.6: Illustration of the origin of the features marked with A,B,C and D on Fig. 2.3, 2.4 and 2.5 as explained in the text. Suppression (enhancement) of the steady state population of a specific level is indicated by a red X (green circle).

excellent agreement with the numerical results shown in Fig. 2.3, 2.4 and 2.5. Our six-level model also provides the equal-time correlations (see Appendix A.2),

$$g_{aa}^{(2)}(0) = \frac{R_\kappa\left(\frac{g}{\sqrt{8}}\right) R_\kappa\left(\frac{g}{2}\right)}{R_\kappa(0) R_\kappa\left(\frac{\sqrt{6}}{4}g\right)}, \quad (2.22)$$

$$g_{ss}^{(2)}(0) = \frac{2R_\kappa\left(\frac{g}{2}\right)}{R_\kappa\left(\frac{\sqrt{6}}{4}g\right)}, \quad (2.23)$$

$$g_{RR}^{(2)}(0) \approx \frac{R_\kappa\left(\frac{g}{2}\right) R_{16\kappa^3/g^2}\left(\frac{g}{2} - \frac{2\kappa^2}{g}\right)}{\left[R_{\kappa/2}\left(\frac{g}{2}\right)\right]^2}. \quad (2.24)$$

Again, these expressions are in agreement with the features seen in the numerical results in Fig. 2.3, 2.4 and 2.5. The positions of maxima and minima are seen directly by the arguments of the factors $R_K(\omega)$. Note that we assumed $g/\kappa \gg 1$ to obtain the simplified expressions in Eqs. (2.22-2.24), but we retained the shift of order $g(\kappa/g)^2$ in the argument in Eq. 2.24 because this shift is larger than the width of the antiresonance.

We now discuss each feature in Fig. 2.3, 2.4 and 2.5 in terms of our six-level model together with the diagonal basis in Eqs. (2.4-2.7). First, at detuning $\Delta = 0$ (point

A in Fig. 2.3) we see $g_{aa}^{(2)}(0) > 1$, indicating bunching. This is due to destructive interference that suppresses the population in $|100\rangle$ (panel A in Fig. 2.6), and can be understood as the system being driven into a dark state, $|d\rangle \propto g|000\rangle - \Omega|011\rangle$, similar to electromagnetically induced transparency (EIT) [55, 100]. In the dark state, $|011\rangle$ remains populated, allowing transitions to $|111\rangle$ which in turn is strongly coupled to $|200\rangle$. The net result is a relative suppression of the probability to have one photon compared to two photons in the driven mode, leading to bunching at $\Delta = 0$. Second, at detuning $\Delta = g/\sqrt{8}$ (point B), mode c_a shows anti-bunching due to a suppressed two-photon probability. Again, this is due to destructive interference, or the presence of a dark state in which $|200\rangle$ remains unpopulated (panel B). Third, at detuning $\Delta = \frac{g}{2}$ (point C), all modes show anti-bunching. This is due to a one-photon resonant transition $|0\rangle \rightarrow |1_+\rangle$ (panel C). Finally, at detuning $\Delta = \frac{\sqrt{6}}{4}g$ (point D), both c_a and c_s show bunching due to a two-photon resonant transition $|0\rangle \rightarrow |2_+\rangle$ (panel D).

2.3.3 Absence of two-photon resonance at $\Delta = 0$

At first glance, the level diagram in Fig. 2.2 together with bunching in Fig. 2.3 suggest a two-photon resonance at zero detuning $\Delta = 0$, where the energy of the eigenstate $|2_0\rangle$ is equal to the energy of two drive photons. However, as discussed above, the bunching at $\Delta = 0$ arises entirely from the suppression of a one-photon population; further, we find that the expected two-photon resonance is cancelled by interference. This can be seen from a second order perturbative calculation of the two-photon Rabi frequency $\Omega_{0,2_0}^{(2)}$ for the transition $|0\rangle \rightarrow |2_0\rangle$. The two-photon state

$|2_0\rangle$ can be populated by the drive $H_{\text{dr}} = \Omega(c_a^\dagger + c_a)$ from state $|0\rangle$ via two intermediate one-photon eigenstates, $|1_\pm\rangle$ given by Eq. 2.5, with energies $\omega_{1\pm} = -\Delta \pm \frac{g}{2}$ in the rotating frame. The resulting Rabi frequency is

$$\Omega_{0,20}^{(2)} = \sum_{n=1_-,1_+} \frac{\langle 2_0 | H_{\text{dr}} | n \rangle \langle n | H_{\text{dr}} | 0 \rangle}{\omega_n}, \quad (2.25)$$

which vanishes at $\Delta = 0$ as a consequence of destructive interference between the two amplitudes. The exact cancellation is lifted by including finite dissipation and the full spectrum; nonetheless this simple argument shows that the expected two-photon resonance at $\Delta = 0$ is strongly suppressed.

Further evidence of the absence of a two-photon resonance at $\Delta = 0$ is the lack of bunching in the undriven mode in Fig. 2.4. If there were a two-photon resonance, one would expect that bunching should also occur in the undriven mode, since the state $|2_0\rangle$ involves both c_a and c_s modes. This is indeed the case at detuning $\Delta = \frac{\sqrt{6}}{4}g$ (see point D in Fig. 2.4), where both modes show bunching as a result of two-photon resonance. In contrast, we see no bunching in the undriven mode at $\Delta = 0$. This supports our conclusion that the observed bunching at $\Delta = 0$ arises from suppression of population in $|100\rangle$ due to interference, as discussed in Section 2.3.2, and not from two-photon resonance. As discussed above, this interference does not suppress population in $|011\rangle$, so we do not expect bunching in the c_s mode from this effect.

Finally, to confirm our intuitive picture we plot the intensity correlation function, $g_{\text{tot}}^{(2)}(0) = \langle n_{\text{tot}}(n_{\text{tot}} - 1) \rangle / \langle n_{\text{tot}} \rangle^2$, of the total photon number, $n_{\text{tot}} = n_a + n_s$, in the coupled OM system in Fig. 2.7. The probability to find one photon in the combined cavity is maximal at $\Delta/g = \pm \frac{1}{2}$ due to one-photon resonance. Similarly, we observe antibunching at point C and bunching at point D, due to interference and two-photon

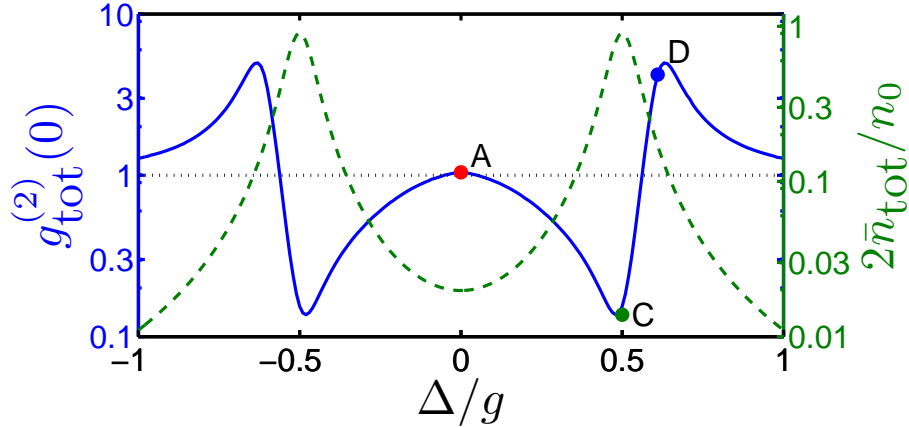


Figure 2.7: Average number (green dashed) and intensity correlation (blue solid) of total photon number in the coupled OM system. Parameters are the same as in Fig. 2.3, and dots mark the same detunings. One- and two-photon resonances are seen at C and D, but we see no bunching in the total photon number at $\Delta = 0$ (point A). This reflects the lack of two-photon resonance due to destructive interference (see Eq. 2.25).

resonance respectively, as discussed in Section 2.3.2. However, we find neither bunching nor antibunching at $\Delta = 0$, demonstrating the absence of a two-photon resonance despite the fact that $|2_0\rangle$ lies at twice the drive frequency.

2.3.4 Finite temperature

So far in our analysis we have focused on the case where the mechanical system is prepared in its vibrational ground state, $|0_m\rangle$. This condition can be achieved using high frequency resonators operated at cryogenic temperatures [64], and in the limit of weak driving $\Omega/\kappa \ll 1$ such that optical heating of the mechanical mode can be neglected. The mechanical groundstate could also be prepared using OM cooling [60, 34, 2, 46, 20, 81, 95, 101, 64, 93, 13], using an optical mode far-detuned from the ones we consider here for nonlinear interactions [88]. Nonetheless, in the following we

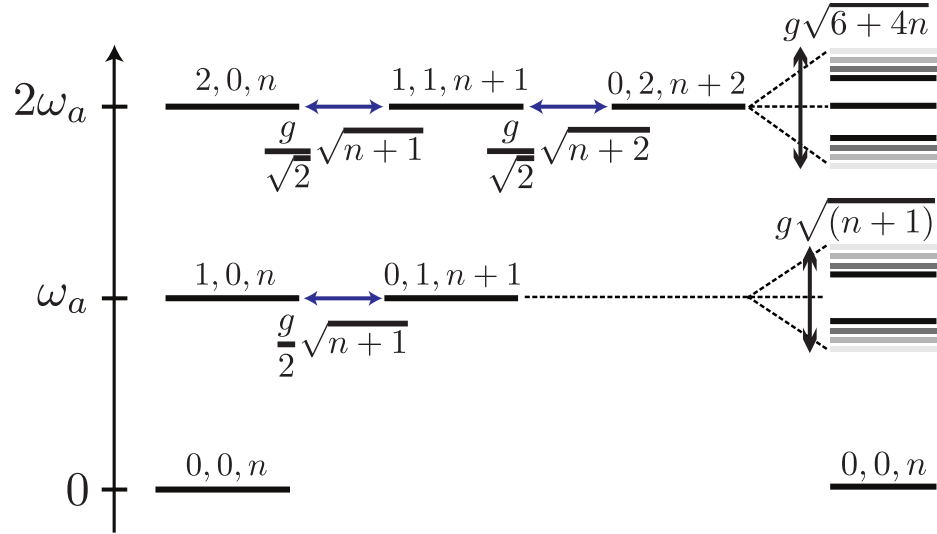


Figure 2.8: Level diagram showing the six states populated by the drive from level $|0,0,n\rangle$ (left), and the associated eigenmodes (right) with n -dependent splittings.

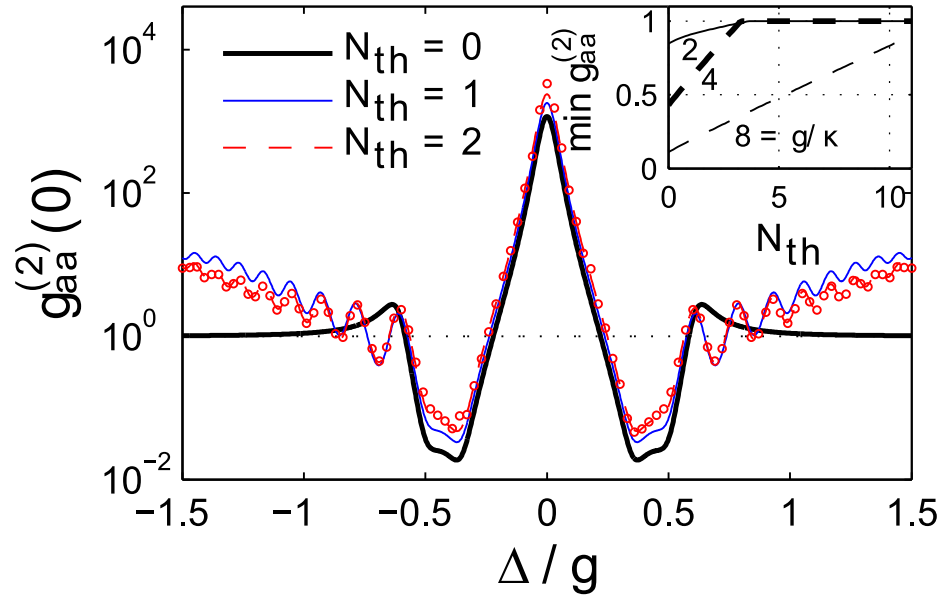


Figure 2.9: Driven mode correlation function $g_{aa}^{(2)}(0)$ for thermal mechanical occupation $N_{th} = 0, 1, 2$. Solid lines show the analytic calculation with $\gamma \rightarrow 0$, and dots show the full numerical results for $N_{th} = 2$ only. The inset shows the minimal $g_{aa}^{(2)}(0)$ as a function of N_{th} for several coupling strengths. Parameters are $g/\kappa = 20$, and (for numerics) $\gamma/\kappa = 10^{-3}$.

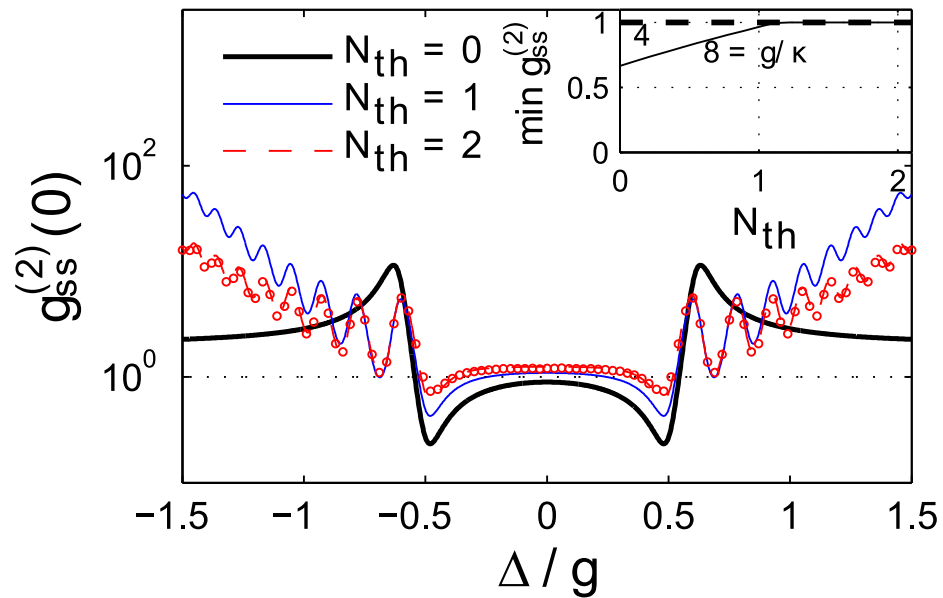


Figure 2.10: Undriven mode correlation function $g_{ss}^{(2)}(0)$ for thermal mechanical occupation $N_{th} = 0, 1, 2$. Solid lines show the analytic calculation with $\gamma \rightarrow 0$, and dots show the full numerical results for $N_{th} = 2$ only. The inset shows the minimal $g_{ss}^{(2)}(0)$ as a function of N_{th} for several coupling strengths. Parameters are $g/\kappa = 20$, and (for numerics) $\gamma/\kappa = 10^{-3}$.

extend our analytic treatment to the case of finite temperature, and show that many of the nonclassical features are robust even in the presence of small but finite thermal occupation of the mechanical mode.

To generalize our previous results we now consider a finite equilibrium occupation number $N_{\text{th}} > 0$ of the mechanical mode, but still assume that $\gamma(N_{\text{th}} + 1) \ll \kappa, g$. Within this approximation we proceed as above, and make a similar six-level ansatz as in Eq. (2.12) for each phonon number n ,

$$\begin{aligned} |\psi_n\rangle = & A_{0,0,n}|0,0,n\rangle + A_{1,0,n}|1,0,n\rangle \\ & + A_{0,1,n+1}|0,1,n+1\rangle + A_{2,0,n}|2,0,n\rangle \\ & + A_{1,1,n+1}|1,1,n+1\rangle + A_{0,2,n+2}|0,2,n+2\rangle, \end{aligned} \quad (2.26)$$

where $|\psi_n\rangle$ includes states up to two photons that are connected by the weak drive and coupling g , starting from the state $|00n\rangle$. As shown in Fig. 2.8 the coupling between the states within each six-level subspace depends explicitly on the phonon number n . Following the same approach as above, the amplitudes in Eq. (2.26) evolve according to

$$\dot{A}_{0,0,n} = 0, \quad (2.27)$$

$$\dot{A}_{1,0,n} = -i\frac{g}{2}\sqrt{n+1}A_{0,1,n+1} - i\Omega A_{0,0,n} - \tilde{\kappa}A_{1,0,n}, \quad (2.28)$$

$$\dot{A}_{0,1,n+1} = -i\frac{g}{2}\sqrt{n+1}A_{1,0,n} - \tilde{\kappa}A_{0,1,n+1}, \quad (2.29)$$

$$\dot{A}_{2,0,0} = -ig\sqrt{\frac{n+1}{2}}A_{1,1,n+1} - i\sqrt{2}\Omega A_{1,0,n} - 2\tilde{\kappa}A_{2,0,n}, \quad (2.30)$$

$$\dot{A}_{1,1,n+1} = -ig\sqrt{\frac{n+1}{2}}A_{2,0,n} - ig\sqrt{\frac{n+2}{2}}A_{0,2,n+2} - i\Omega A_{0,1,n+1} - 2\tilde{\kappa}A_{1,1,n+1}, \quad (2.31)$$

$$\dot{A}_{0,2,n+2} = -ig\sqrt{\frac{n+2}{2}}A_{1,1,n+1} - 2\tilde{\kappa}A_{0,2,n+2}. \quad (2.32)$$

We solve for the steady state amplitudes within each subspace n and average the result over the initial thermal phonon distribution, assuming no coupling between subspaces due to the small phonon relaxation rate. We obtain the average photon numbers

$$\bar{n}_a = \sum_n \zeta_n |\bar{A}_{1,0,n}|^2, \quad \bar{n}_s = \sum_n \zeta_n |\bar{A}_{0,1,n+1}|^2, \quad (2.33)$$

where $\zeta_n = e^{-\beta \hbar \omega_m n} (1 - e^{-\beta \hbar \omega_m})$ and $\beta^{-1} = k_B T$. Similarly, the $g_{ii}^{(2)}(0)$ functions are given by

$$g_{aa}^{(2)}(0) = 2 \sum_n \zeta_n |\bar{A}_{2,0,n}|^2 / \bar{n}_a^2, \quad (2.34)$$

$$g_{ss}^{(2)}(0) = 2 \sum_n \zeta_n |\bar{A}_{0,2,n+2}|^2 / \bar{n}_s^2. \quad (2.35)$$

We provide the expressions for the steady state amplitudes $\bar{A}_{2,0,n}$ and $\bar{A}_{0,2,n+2}$ in the Appendix A.2.

We plot the correlation functions, $g_{aa}^{(2)}(0)$ in Fig. 2.9 and $g_{ss}^{(2)}(0)$ in Fig. 2.10 for different thermal phonon numbers, N_{th} . Solid lines were calculated from the above analytic approach with $\gamma \rightarrow 0$, and we find excellent agreement with the full numerical results including small but finite γ (dots, shown only for thermal occupation $N_{\text{th}} = 2$). We see that the zero temperature features such as antibunching survive at finite temperature for sufficiently strong coupling [88]. In the insets we plot the minimum antibunching as a function of thermal occupation number for several ratios g/κ . Antibunching remains visible up to a critical thermal phonon number, set by g/κ , beyond which the contributions from different phonon numbers smear out the effect and antibunching vanishes. In addition, for detunings $|\Delta| > g/2$, a series of

new resonances appear in the correlation functions, and for small but finite occupation numbers we find new antibunching features that are absent for $N_{\text{th}} = 0$. These new features can be understood from the n -dependent splitting of the one- and two-photon manifolds as indicated in Fig. 2.8. For higher temperatures the individual resonances start to overlap, and we observe an overall increase over a broad region of large positive and negative detunings due to the cumulative effect of different phonon numbers.

2.4 Delayed coincidence and single phonon states

In addition to the equal-time correlations discussed above, quantum signatures can also be manifested in photon intensity correlations with a finite time delay. We now turn to a discussion of delayed coincidence characterized by the two-time intensity correlations functions,

$$g_{ii}^{(2)}(\tau) = \frac{\langle c_i^\dagger(0)c_i^\dagger(\tau)c_i(\tau)c_i(0) \rangle}{\langle c_i^\dagger c_i \rangle^2}, \quad (2.36)$$

for both driven and undriven modes, $i = a, s$. Expressing this correlation in terms of a classical light intensity I , $g^{(2)}(\tau) = \langle I(\tau)I(0) \rangle / \langle I \rangle^2$, and using the Schwarz inequality, we obtain the inequalities [11, 7],

$$g^{(2)}(\tau) \leq g^{(2)}(0), \quad (2.37)$$

$$|g^{(2)}(\tau) - 1| \leq |g^{(2)}(0) - 1|. \quad (2.38)$$

Similar to the classical inequality $g^{(2)}(0) > 1$ at zero delay, violation of either of these inequalities at finite delay is a signature of quantum light. We calculate the delayed

coincidence correlation functions for both the driven and undriven modes.

2.4.1 Driven mode

The correlation function $g_{aa}^{(2)}(\tau)$ is shown in Fig. 2.11(a) for two values of the detuning Δ . The most striking feature is the apparent vanishing of $g_{aa}^{(2)}(\tau)$ at several values of τ when the detuning is $\Delta = 0$ (curve A in Fig. 2.11(a)). These are due to Rabi oscillations at frequency $g/2$ following the detection of a photon. This vanishing of the finite delay correlation function is reminiscent of wavefunction collapse that occurs in a cavity containing an atomic ensemble [11], and while its origins are similar, there are important differences as we now discuss.

We can understand the finite delay intensity correlations in terms of the simple six-level model discussed in the previous section. We extend this model to describe finite delay correlations by considering the effect of photodetection on the steady state of the system. Detection of a photon in the driven mode projects the system onto the conditional state [32],

$$|\psi^a\rangle = \frac{c_a|\psi\rangle}{\|c_a|\psi\rangle\|}, \quad (2.39)$$

where $|\psi\rangle$ is given by Eq. 2.12 with steady state amplitudes and $\|\cdot\|$ denotes normalization after the jump. The conditional state $|\psi^a\rangle$ has an *increased* amplitude A_{100} after the jump (see jump at $\tau = 0$ in Fig. 2.11 (b)). Following this initial photodetection, the amplitude A_{100} subsequently undergoes Rabi oscillations with frequency $g/2$, and decays back to its steady state at rate 2κ . For sufficiently large bunching at zero delay and strong coupling $g > \kappa$, the Rabi oscillations of the amplitude $A_{100}(\tau)$ can cause it to cross zero several times before it decays back to steady state. As the

probability to detect a second photon is dominated by A_{100} , its zeros are responsible for the zeros in the correlation function $g_{aa}^{(2)}(\tau)$ zero at these delay times.

The zeros in $g^{(2)}(\tau)$ appear similar to those exhibited in a cavity strongly coupled to an atomic ensemble [11, 75, 7] or a single atom [16]. However, in stark contrast to the atomic case, the zeros in Fig. 2.11(a) are the result of Rabi oscillations following the initial quantum jump. This is qualitatively different from the atomic case, where the change in sign of the relevant amplitude (the analogy of A_{100}) occurs *immediately* after the jump itself, and the amplitude is damped back to steady state at the atomic decay rate Γ , without Rabi oscillation. As a consequence, the vanishing correlation function in the atomic case occurs at a delay set by $\tau_0 \sim \gamma^{-1} \ln C$, requiring only strong cooperativity $C = g^2/\kappa\gamma > 1$ to be visible. On the other hand, the zeros in Fig. 2.11(a) occur at delay times set by $\tau \sim 1/g$, requiring strictly strong coupling $g > \kappa$.

Before moving on to correlations of the undriven mode, we briefly discuss the correlations of the driven mode at the other value of detuning shown in Fig. 2.11(a). At detuning $\Delta = \frac{g}{\sqrt{2}}$ (curve E), which shows bunching at zero time, $g_{aa}^{(2)}(0) \gtrsim 1$, increases above its initial value at finite delay. This is a violation of the classical inequality in Eq. 2.37, and is an example of “delayed bunching,” or an increased probability to detect a second photon at a finite delay time. A similar effect was recently studied in a single mode OMS [49]. However, like the Rabi oscillations, the increased correlation function decays back to its steady state value of 1 on the timescale of κ^{-1} .

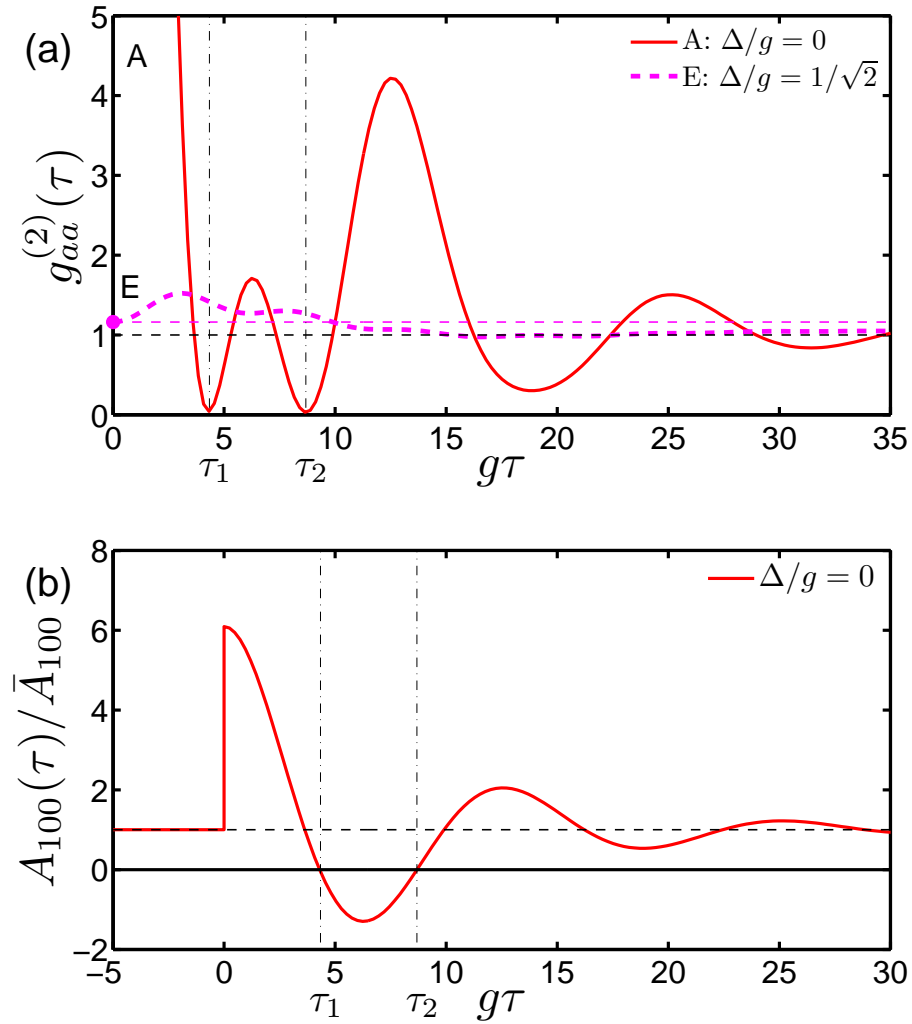


Figure 2.11: (a) Finite time delay intensity correlation function $g_{aa}^{(2)}(\tau)$ for detunings $\Delta/g = 0$ (A) and $\frac{1}{\sqrt{2}}$ (E). Detuning for curve A is the same as marked in Fig. 2.3, while E shows a new effect not seen at equal times. Thin dashed line indicates the classical bound (see Eq. 2.37) for curve E. (b) Evolution of amplitude A_{100} (normalized by its steady state value) at detuning A, $\Delta/g = 0$, after detecting a driven c_a photon at $\tau = 0$. Vertical dash-dotted lines mark delay times (τ_1, τ_2) where this amplitude vanishes resulting in the vanishing of $g_{aa}^{(2)}(\tau)$ in (a). Parameters are $g/\kappa = 8$ and $\gamma/\kappa = 0.02$.

2.4.2 Heralded single phonon states

We now turn to a discussion of the delayed coincidence correlations of the undriven mode c_s . We note that correlations of the driven and undriven modes can be measured separately provided sufficient frequency resolution, smaller than the mechanical frequency. The correlation function $g_{ss}^{(2)}(\tau)$ of the undriven mode is shown in Fig. 2.12 for several values of detuning. Similar to the driven mode, the correlation function of the undriven mode exhibits Rabi oscillations that decay on the short optical timescale $1/\kappa$. For detuning $\Delta = 0$ and $\Delta/g = \frac{\sqrt{6}}{4}$ (curves A and D in Fig. 2.12), the correlation $g_{ss}^{(2)}(\tau)$ is described by our previous six-level model of Eqs. (2.13–2.18). However, at detuning $\Delta = \frac{g}{\sqrt{2}}$ (curve E), we see that $g_{ss}^{(2)}(\tau)$ has a long tail that decays on the much longer mechanical timescale $1/\gamma$. This is due to the heralded preparation of a single phonon by detection of a photon in the undriven mode, as we now discuss.

The increase in delayed coincidence can be understood by extending the above analytic six-level model to account for the conditional state of the system after detection of a photon in the undriven mode. To do this, we simply add three additional states to the six-level ansatz in Eq. 2.12,

$$|\psi\rangle = \dots + A_{001}|001\rangle + A_{101}|101\rangle + A_{012}|012\rangle, \quad (2.40)$$

since these are the states populated by detection of a c_s photon from the original six states (see Fig. 2.13). Using the same approach as before, we obtain the following

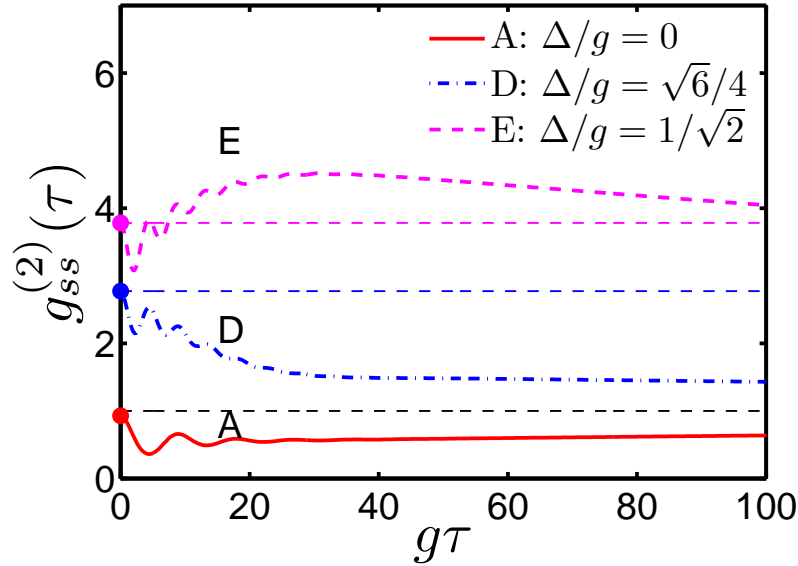


Figure 2.12: Finite time delay intensity correlation function $g_{ss}^{(2)}(\tau)$ for detunings $\Delta/g = 0$ (A), $\sqrt{6}/4$ (D) and $1/\sqrt{2}$ (E). Thin dashed lines indicate the classical bounds (see Eq. 2.37). Labels A, D, E correspond to the same detunings marked in Fig. 2.3 and Fig. 2.11. Parameters are $g/\kappa = 8$, and $\gamma/\kappa = 0.02$.

equations for the amplitudes,

$$\dot{A}_{001} \approx -\frac{\gamma}{2}A_{001}, \quad (2.41)$$

$$\dot{A}_{101} = -i\frac{g}{\sqrt{2}}A_{012} - i\Omega A_{001} - \tilde{\kappa}A_{101}, \quad (2.42)$$

$$\dot{A}_{012} = -i\frac{g}{\sqrt{2}}A_{101} - \tilde{\kappa}A_{012}, \quad (2.43)$$

where we used $\gamma \ll \kappa$ and kept the leading term in Eq. 2.41. We obtain $g_{ss}^{(2)}(\tau)$ by solving these equations for initial conditions determined by the conditional state $|\psi^s\rangle$ after a quantum jump,

$$|\psi^s\rangle = \frac{c_s|\psi\rangle}{||c_s|\psi\rangle||}, \quad (2.44)$$

which is a superposition of states $|001\rangle, |101\rangle, |012\rangle$ (see Appendix A.2 for details),

but in the limit of weak driving consist mainly of $|001\rangle$.

Detection of a photon in the undriven mode implies that the three-wave mixing interaction converted a photon from the driven mode into the undriven mode by simultaneously adding a phonon. The relevant three-level subspace after the jump (see Fig. 2.13) has a similar structure as in the steady state, but the presence of an extra phonon modifies the splitting of the one-photon states $|1'_{\pm}\rangle = (|101\rangle \pm |012\rangle)/\sqrt{2}$ to $\frac{g}{\sqrt{2}}$ (instead of $g/2$ without a phonon). This changes the one-photon resonance

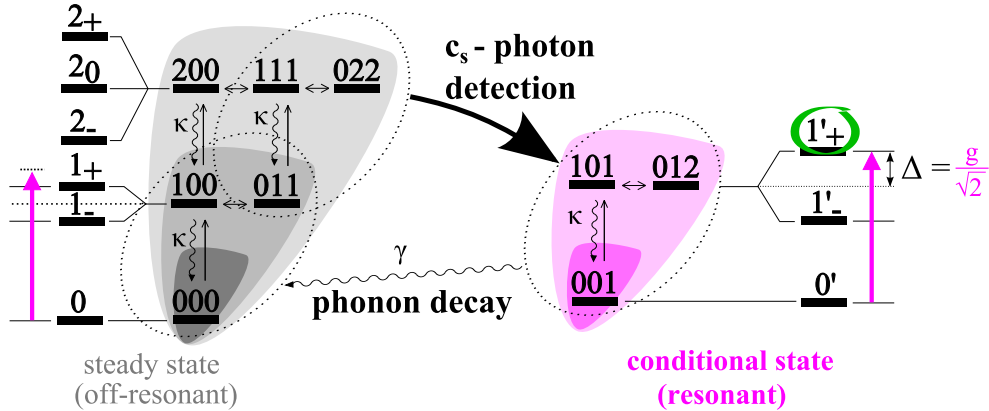


Figure 2.13: Effect of detection of a c_s photon at detuning Δ ($\Delta/g = \frac{1}{\sqrt{2}}$). In steady state (gray region on left), the drive is far off-resonant. However, after detection of a c_s photon the system jumps into the conditional subspace (pink region on right). Due to the presence of an extra phonon in this subspace, the drive is resonant and the probability to detect a second photon is much higher than in steady state. This increased probability persists as long as the extra phonon, which decays slowly at rate γ .

condition for the drive to $\Delta = \frac{g}{\sqrt{2}}$. Therefore, at this value of the detuning, the process of exciting the system and emitting a single c_s photon is off-resonant; while after the detection of a first c_s photon the system is prepared in $|001\rangle$, bringing it into resonance with the drive. This *enhances* the probability for subsequent excitation and emission of a second c_s photon, increasing the correlation function at finite delay.

The maximum delayed coincidence occurs after a delay of $\tau \sim 1/\kappa$, when the photons have reached the metastable steady state in the conditional subspace with one extra phonon. Eventually, the delayed coincidence returns to its true steady state value of one on the timescale $\tau \sim 1/\gamma$, which is the mechanical decay time of the state $|001\rangle$. The long tails observed for other values of detuning (curves A and D) are also due to the presence of an extra phonon, but in these cases the system remains off-resonant after the initial c_s photon and the effect is less pronounced. Note that the probability to detect a photon from the *driven* mode also increases in the conditional state, so a similar effect is seen in the delayed cross-correlation function $g_{as}^{(2)}(\tau)$, where the photon in the undriven mode is detected first.

2.5 Reaching strong coupling

The nonclassical correlations predicted in this paper require strong optomechanical coupling, $g > \kappa$, as well as sideband resolution, $\omega_m \gg \kappa, \gamma$. While the combination of these conditions has not yet been demonstrated, several experimental efforts are currently directed at reaching this regime. By using micro- and nano-fabricated OMSs such as microtoroids or photonic crystal beams, high frequency mechanical systems with $\omega_m \approx 50$ MHz - 5 GHz can be combined with low loss optical modes, such that the condition $\omega_m \gg \kappa \gg \gamma$ is satisfied [79, 81, 28]. At the same time the mechanical system can already be prepared close to the quantum ground state by working at cryogenic temperatures. In micro-fabricated OMSs, single-photon couplings of about $g/\kappa \approx 0.001$ have been demonstrated [28, 22, 99] The largest value to date of $g/\kappa \approx 0.007$ has been reached in photonic crystal beam resonators [14], where colocalized

optical and vibrational resonances are highly confined to maximize coupling while the surrounding structure is engineered to minimize loss. Conversely, in cold atomic experiments the effective strong OM coupling regime has been reached [68], while sideband resolution remains a challenge [87].

There are several existing proposals for how to meet the challenge of $g/\kappa > 1$ in the photonic crystal beam setup. First, the single-photon optomechanical coupling can be increased by making use of nanoslots in the structure [77, 21] to further localize the electric field at the position of the mechanical mode. This could improve g by a factor of 10 [54]. Second, numerical studies suggest that κ can be further decreased by fine tuning the size and position of the slots in the photonic crystals [62, 90]. Finally, new materials are currently being tested for an overall improvement of the OM properties of nano-fabricated devices [103]. Thus by using these ultrahigh Q photonic crystals or similar designs, an increase of g/κ by a factor of ~ 100 is realistic. Note that once the strong coupling condition has been achieved, the implementation of two or multimode OMSs with adjustable tunneling $2J \sim \omega_m$ can be realized via evanescent field coupling, as has already been demonstrated in the weak coupling regime [79, 28, 38].

2.6 Conclusions

We have studied nonclassical intensity correlations in a driven, near-resonant optomechanical system with one mechanical and two optical modes. In the regime of strong coupling $g > \kappa$, this system allows for nonlinear quantum optics through a resonant three-mode interaction in which the exchange of two photons is mediated by

a phonon. We have identified several different processes that can lead to nonclassical antibunching and delayed bunching, and we have derived a simple analytic model that allows us to describe and interpret photon-photon correlations in this system both at zero and at finite temperature. Our findings will be important as experiments approach the regime of strong OM coupling, and for potential applications of OMSs for quantum information processing. In particular, the long-lived correlation found for the undriven mode raises the intriguing possibility to exploit such a setup as a quantum memory. The generation of heralded single phonons on detection of a photon from the undriven mode may have implications for building OM quantum repeaters and quantum communication devices.

Chapter 3

Optomechanical quantum information processing

3.1 Introduction

Optomechanics describes the radiation pressure interaction between an optical cavity mode and the motion of a macroscopic mechanical object, as it appears, for example, in a Fabry-Pérot cavity with a moveable mirror [45, 57, 3]. First demonstrations of optomechanical (OM) laser cooling [60, 34, 2, 46, 20, 95, 81, 101] have recently attracted significant interest and led to tremendous progress in the development of new fabrication methods and experimental techniques for controlling OM interactions at the quantum level. Apart from ground-state cooling [93, 13], this includes the demonstration of slow light [100, 78], and the coherent interconversion of optical and mechanical excitations [31, 99]. These achievements pave the way for a new type of quantum light-matter interface and give rise to interesting perspec-

tives for novel OM-based quantum technologies. As a solid-state approach, such an all-OM platform would benefit directly from advanced nanofabrication and scalable integrated photonic circuit techniques. At the same time, long mechanical lifetimes comparable to those of atomic systems allow us to combine optical nonlinearities with a stationary quantum memory for light.

In this work we study strong OM coupling effects in *multimode* OM systems (OMSs) and describe how resonant or near-resonant interactions in this setting allow us to exploit the intrinsic nonlinearity of radiation pressure in an optimal way. Our approach is based on the resonant exchange of photons between two optical modes mediated by a single phonon. This resonance induces much stronger nonlinearities than achievable in single-mode OMSs, where nonlinear effects are suppressed by a large mechanical frequency [58, 53, 69, 63]. Consequently, multimode OMSs provide a promising route for accessing the single-photon strong-coupling regime, where the coupling g_0 as well as the mechanical frequency ω_m exceeds the cavity decay rate κ [69]. This regime is within reach of state-of-the-art nanoscale OM devices [13, 28, 12, 22] or analogous cold atom OMSs [39, 8], and here we discuss how strong OM interactions in a multimode setup can be used to generate single photons and to perform controlled gate operations between photonic or mechanical qubits. Combined with very recently developed photon-phonon interfaces and quantum memories based on linearized OM couplings [31, 99, 79], our results provide a basis for efficient OM classical and quantum information processing with applications ranging from photon transistors to quantum repeaters and networks.

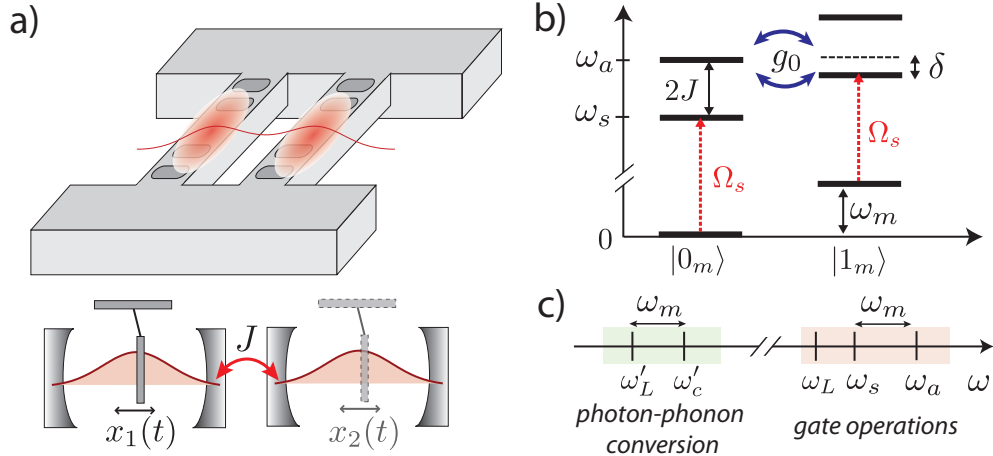


Figure 3.1: a) Setup of two tunnel-coupled OM crystal cavities (see Ref. [28, 13] for more details). b) Level diagram showing the lowest mechanical and optical excitations in a two mode OMS. Resonant coupling ($\delta = 0$) occurs when the tunnel splitting $2J$ between the optical modes is comparable to the mechanical frequency ω_m . c) Different sets of strongly and weakly coupled optical modes and control laser fields can be used for nonlinear interactions ($\omega_s, \omega_a, \omega_L$) and purely linear photon storage and retrieval operations (ω'_c, ω'_L).

3.2 Model

We consider a setup of two tunnel-coupled OMSs [61, 38, 23, 79, 17] as schematically shown in Fig. 3.1, focusing on the OM crystal design [28, 13] as a specific example. Each OMS $i = 1, 2$ is represented by an optical mode of frequency ω_c and a bosonic operator c_i , which is coupled via optical gradient forces to the motion of an isolated mechanical mode b_i with vibrational frequency ω_m^i . The Hamiltonian for this system is ($\hbar = 1$)

$$H = \sum_{i=1,2} \omega_m^i b_i^\dagger b_i + \omega_c c_i^\dagger c_i + g_0 c_i^\dagger c_i (b_i + b_i^\dagger) - J(c_1^\dagger c_2 + c_1 c_2^\dagger) + \sum_{i=1,2} \Omega_i (c_i e^{i\omega_L t} + \text{H.c.}), \quad (3.1)$$

where J is the tunneling amplitude between the optical modes and g_0 denotes the single-photon OM coupling; Ω_i are the local amplitudes of external control laser fields of frequency ω_L . Below we also consider an additional set of cavity modes and driving fields with frequencies ω'_c and ω'_L , respectively. As indicated in Fig. 3.1(c), we assume these modes to be separated in frequency and used for cooling the mechanical modes [102, 56], and linear photon storage and retrieval operations [31, 99, 104, 1] only.

Apart from the coherent dynamics described by Eq. (3.1), we include dissipation through cavity decay and mechanical damping and model the evolution of the system density operator ρ by a master equation (ME)

$$\dot{\rho} = -i[H, \rho] + \sum_i \kappa \mathcal{D}[c_i]\rho + \mathcal{L}_\gamma\rho, \quad (3.2)$$

where $\mathcal{D}[c]\rho = 2c\rho c^\dagger - \{c^\dagger c, \rho\}_+$, and $\mathcal{L}_\gamma = \sum_i \frac{\gamma}{2}(N_{\text{th}} + 1)\mathcal{D}[b_i] + \frac{\gamma}{2}N_{\text{th}}\mathcal{D}[b_i^\dagger]$. Here, κ is the optical field decay rate, $\gamma = \omega_m/Q$ the mechanical damping rate for a quality factor Q and $N_{\text{th}} = (e^{\hbar\omega_m/k_B T} - 1)^{-1}$ the mechanical equilibrium occupation number for temperature T . Below we identify $\Gamma_m = \frac{\gamma}{2}(3N_{\text{th}} + \frac{1}{2})$ as the characteristic decoherence rate for mechanical qubit states¹.

3.3 Resonant strong-coupling optomechanics

We focus on the strong coupling regime $\omega_m, g_0 \gg \kappa, \Gamma_m$, and our main goal is to show how the multimode OMS described by Eq. (3.1) can be used for implementing controlled interactions between qubits encoded in photonic or phononic de-

¹ Γ_m corresponds to the initial decoherence rate of a phonon superposition $(|0_m\rangle + |1_m\rangle)/\sqrt{2}$.

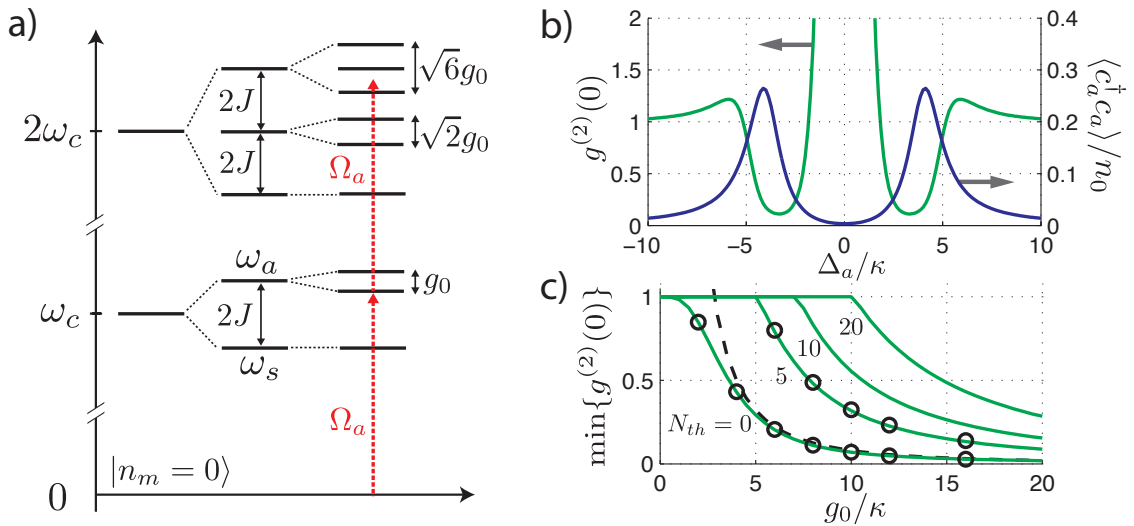


Figure 3.2: a) Energy level diagram of a resonantly coupled OMS, $\delta = 2J - \omega_m = 0$, and for a single mechanical mode in the ground state. b) Excitation spectrum and $g^{(2)}(0)$ for a weak coherent field exciting the c_a mode, where $g_0/\kappa = 8$ and $n_0 = \Omega_a^2/\kappa^2$. c) Minimal value of $g^{(2)}(0)$ as a function of the OM coupling strength g_0 and for different values of N_{th} . The analytical results (solid lines) given in the text are in good agreement with exact numerics (circles). The dashed line shows the asymptotic scaling $\sim 8\kappa^2/g_0^2$ at zero temperature.

grees of freedom. To illustrate this we first consider a single mechanical resonator, $b \equiv b_1$, $\omega_m \equiv \omega_m^1$. We introduce symmetric and antisymmetric optical modes $c_{s,a} = (c_1 \pm c_2) / \sqrt{2}$ with eigenfrequencies $\omega_{s,a}$ split by $2J$. Further, we assume that $\omega_m \sim 2J \gg g_0, \kappa, |\delta|$, where $\delta = 2J - \omega_m$ (see Fig. 3.1(b)). This condition can be achieved in nanoscale OMSs where $\omega_m \sim \text{GHz}$ [28, 13, 12, 22] and a matching tunnel splitting can be designed by appropriately adjusting the spacing between the cavities [28, 38]. In this regime we can make a rotating wave approximation with respect to the large frequency scale $\omega_m \sim 2J$ and after changing into a frame rotating with ω_L we obtain [38]

$$H = -\Delta_s c_s^\dagger c_s - \Delta_a c_a^\dagger c_a + \omega_m b^\dagger b + \frac{g_0}{2} (c_a c_s^\dagger b^\dagger + c_a^\dagger c_s b) + H_\Omega(t). \quad (3.3)$$

Here $\Delta_{s,a} = \omega_L - \omega_{s,a}$ are the detunings of the driving field from the c_s and c_a mode, respectively, and $H_\Omega(t) = \sum_{\eta=s,a} (\Omega_\eta(t) c_\eta + \text{H.c.})$ accounts for the external driving fields with slowly varying amplitudes $\Omega_{s,a}(t) = (\Omega_1(t) \pm \Omega_2(t)) / \sqrt{2}$.

The two-mode OM coupling in Eq. (3.3) describes photon transitions between the energetically higher mode c_a to the lower mode c_s , while simultaneously absorbing or emitting a phonon. For $(\Delta_s - \Delta_a - \omega_m) = \delta = 0$, this leads to a resonant interaction between states $|n_a, n_s, n_m\rangle$ and $|n_a - 1, n_s + 1, n_m + 1\rangle$, where n_a , n_s and n_m label the occupation numbers of the two optical modes and the mechanical mode, respectively. In analogy to atomic cavity quantum electrodynamics (QED) [70], the nonlinear scaling of the corresponding transition amplitudes $\frac{g_0}{2} \sqrt{n_a(n_s + 1)(n_m + 1)}$ results in an anharmonic level diagram as shown in Fig. 3.2(a). If g_0 exceeds the cavity linewidth κ , one and two photon transitions can be spectrally resolved, indicating the onset of strong single-photon nonlinearities.

3.4 An OM single-photon source

As a potential first application of the nonlinear OM interaction we discuss the use of the OMS as a single-photon source, which is characterized by a vanishing equal time two-photon correlation function $g^{(2)}(0)$. In Fig. 3.2(b) we plot the excitation spectrum $\langle c_a^\dagger c_a \rangle$ and $g^{(2)}(0) = \langle c_a^\dagger c_a^\dagger c_a c_a \rangle / \langle c_a^\dagger c_a \rangle^2$, for the case where only the c_a mode is weakly driven. Around the single-photon resonances $\Delta_a = \pm g_0/2$ we observe strong anti-bunching $g^{(2)}(0) < 1$ as a clear signature of non-classical photon statistics. To quantify this effect we assume that $\Gamma_m \ll \kappa$, which allows us to treat subspaces connected to different $|n_m\rangle$ separately. For weak driving fields $\Omega_a \ll \kappa$, the system dynamics can then be restricted to the six states $|0_a, 0_s, n_m\rangle, |1_a, 0_s, n_m\rangle, |0_a, 1_s, n_m + 1\rangle, |2_a, 0_s, n_m\rangle, |1_a, 1_s, n_m + 1\rangle, |0_a, 2_s, n_m + 2\rangle$ and we calculate the relevant occupation probabilities $p_{1,0,n_m}$ and $p_{2,0,n_m}$ to leading order in Ω_a [11]. We obtain

$$p_{1,0,n} = \left| \frac{4\Omega_a d}{X_n} \right|^2, \quad p_{2,0,n} = 8 \left| \frac{\Omega_a^2 (8d^2 - g_0^2)}{(X_n (2X_n - g_0^2))} \right|^2, \quad (3.4)$$

where $d = \Delta_a - i\kappa$ and $X_n = d^2 - g_0^2(n + 1)$. By taking the appropriate thermal averages, $\langle n_a \rangle = \sum_n \zeta_n p_{1,0,n}$ and $g^{(2)}(0) = 2 \sum_n \zeta_n p_{2,0,n} / \langle n_a \rangle^2$, where $\zeta_n = (1 - e^{-\beta \hbar \omega_m}) e^{-\beta \hbar \omega_m n}$ and $\beta^{-1} = k_B T$, the two photon correlation function can be evaluated for arbitrary temperatures T .

In Fig. 3.2(c) we plot the minimal value of $g^{(2)}(0)$ as a function of the coupling strength g_0 and for different N_{th} . As the OM coupling increases we find that for $T = 0$ the minimum of the correlation function scales as $\min_{\Delta_a} \{g^{(2)}(0)\} \simeq 8\kappa^2/g_0^2$. This demonstrates an improved scaling over off-resonant photon blockade effects in single-mode OMSs, where for large ω_m only a small reduction $g^{(2)}(0) \simeq 1 - g_0^2/(\kappa \omega_m)$ can

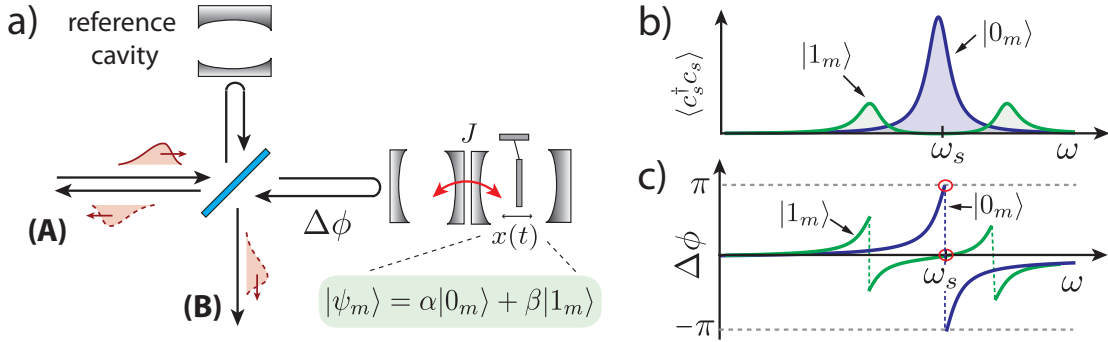


Figure 3.3: a) An incoming photon in port (A) passes through the interferometric setup and leaves through port (A) or (B), depending on the phase shift $\Delta\phi$ acquired upon reflection from the two-mode OMS. b), c) For a mechanical system in state $|0_m\rangle$, the OMS exhibits a single resonance at ω_s ($\Delta\phi = \pi$), while for state $|1_m\rangle$ the resonance splits by $g_0 \gg \kappa$ and the photon does not enter the cavity ($\Delta\phi = 0$).

be obtained [69]. Since the positions of the single and two-photon resonances depend explicitly on the mechanical state $|n_m\rangle$, finite temperature degrades the quality of the single-photon source. Nevertheless, with increasing coupling strength the anti-bunching effect becomes surprisingly robust and when combined with cooling cycles to achieve $\langle n_m \rangle \sim 1$ [13], allows the operation of OM single-photon sources even at environmental temperatures of a few Kelvin.

3.5 Single-phonon single-photon transistor

Given the ability to generate single photons, Fig. 3.3 illustrates a basic scheme for using the same resonant OMS to implement a two-qubit gate [24]. First, we assume that the state of a control photon is mapped onto a mechanical superposition state $\alpha|0_m\rangle + \beta|1_m\rangle$. This can be achieved with conventional cooling followed by photon-phonon conversion techniques using linearized OM interactions with an aux-

iliary mode ω'_c (see Fig. 3.1(c)). Next, a single target photon of central frequency $\sim \omega_s$ is sent through the interferometric setup as described in Fig. 3.3. If the mechanical mode is in the state $|0_m\rangle$, the incoming photon couples to a single resonant state $|0_a, 1_s, 0_m\rangle$ (see Fig. 3.1(b)), such that it enters the cavity and picks up a phase before being reflected. Instead, if the mechanical resonator is in the state $|1_m\rangle$, the resonant coupling between $|0_a, 1_s, 1_m\rangle$ and $|1_a, 0_s, 0_m\rangle$ splits the cavity resonance, and for $g_0 > \kappa$ the photon is reflected without a phase shift. Under ideal conditions, the final result is an entangled state

$$|\psi\rangle = \alpha|0_m, 1_A, 0_B\rangle + \beta|1_m, 0_A, 1_B\rangle, \quad (3.5)$$

where A and B are the two ports of the interferometer. This state can be converted back into an entangled state between the initial control and target photon.

Assuming that the storage and retrieval of the control photon can be achieved with high fidelity, the error for producing the entangled state (3.5) with $\alpha = \beta = 1/\sqrt{2}$ is approximately given by

$$\epsilon \approx \frac{4\kappa^2}{g_0^2} + \frac{1}{(\tau_p \kappa)^2} + \tau_p \Gamma_m, \quad (3.6)$$

where τ_p is the duration of the single-photon pulse. The individual contributions in Eq. (3.6) arise from an imperfect photon reflection, the finite spectral width of the photon pulse, and mechanical decoherence, respectively. A minimal error is achieved for $\tau_p^{-1} \approx \sqrt[3]{\kappa^2 \Gamma_m}$ where we obtain $\epsilon \approx \max\{4\kappa^2/g_0^2, \sqrt[3]{\Gamma_m^2/\kappa^2}\}$. Assuming an OM crystal device with $\omega_m/(2\pi) = 4$ GHz and $Q = 10^5$ as discussed in Ref. [13], but with an improved OM coupling $g_0/(2\pi) = 50$ MHz and a lower decay rate $\kappa/(2\pi) = 5$ MHz, we obtain gate errors $\epsilon \approx 0.1$ for environmental temperatures around $T \approx 100$ mK.

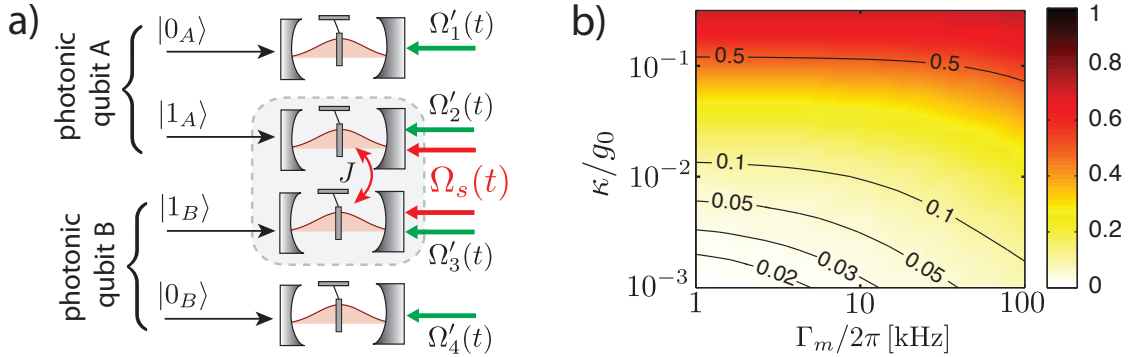


Figure 3.4: a) OM quantum memory, where ‘path-encoded’ photonic qubits are stored in long-lived mechanical states using tunable linearized OM interactions $\sim \Omega'_i(t)$. Deterministic gate operation between stationary qubits are implemented by a controlled phonon-phonon interaction $\sim \Omega_s(t)$ as described in the text. b) The total error ϵ_g for implementing a controlled phase gate between two phononic qubits is minimized with respect to Δ_s and plotted as a function of κ and Γ_m (see text). The parameters for this plot are $g_0/(2\pi) = 50$ MHz, $\gamma/(2\pi) = 4$ kHz, $\alpha = 1$ and $g_0/\delta = 1/3$.

3.6 Phonon-phonon interactions

Finally, we consider the possibility to perform a controlled gate operation between two qubits stored in long-lived mechanical modes. Our approach is depicted in Fig. 3.4(a), and combines the long coherence times of an OM quantum memory [31, 99, 104, 1] with the practical utility of exploiting interactions between stationary phononic qubits. We focus on the limit $\Gamma_m \ll \kappa$, and assume that optical (e.g. ‘path encoded’) qubits are first mapped onto long-lived states $|0_m\rangle$ and $|1_m\rangle$ of two or more mechanical modes. The OM coupling is then employed to generate nonlinear interactions between the phonons only.

We consider nonlinear interactions between two mechanical modes b_1 and b_2 described by Eq. (3.1), detuned from resonance such that $g_0 < |(2J - \omega_m^i)|$ and direct transitions between photons and phonons are suppressed. To obtain the effective

phonon-phonon interactions, we first diagonalize H to second order in $\xi_i = g_0/(2J - \omega_m^i)$ with the transformation $H \rightarrow e^{iS}He^{-iS}$, where $S = \frac{i}{2}(c_s^\dagger c_a(\xi_1 b_1^\dagger - \xi_2 b_2^\dagger) - \text{H.c.})$. This yields $H = H_0 + H_g + H_\Omega(t)$, where $H_0 = -\Delta_s c_s^\dagger c_s - \Delta_a c_a^\dagger c_a + \sum_i \omega_m^i b_i^\dagger b_i$,

$$H_g = \frac{g_0}{4} [(c_s^\dagger c_s + 1)c_a^\dagger c_a(\xi_1 + \xi_2) + (c_a^\dagger c_a - c_s^\dagger c_s)\mathcal{N}_b], \quad (3.7)$$

and we have neglected small corrections to the driving Hamiltonian $H_\Omega(t)$. The phonon operator in Eq. (3.7) is given by $\mathcal{N}_b = \xi_1 b_1^\dagger b_1 + \xi_2 b_2^\dagger b_2 - (\xi_1 + \xi_2)(b_1^\dagger b_2 + b_2^\dagger b_1)/2$. For simplicity we focus on symmetric detuning, $\omega_m^{1,2} = 2J \mp \delta$, where $\mathcal{N}_b = \frac{g_0}{\delta}(b_1^\dagger b_1 - b_2^\dagger b_2)$. The transformation also modifies the dissipative terms in the Eq. (3.2); most importantly, we find an optically-induced decay channel for the mechanical modes, $\mathcal{L}_\gamma \rightarrow \mathcal{L}_\gamma + \kappa g_0^2/(4\delta^2)\mathcal{D}[c_s(b_1 + b_2)]$.

We assume that only the c_s mode is weakly driven by a slowly-varying control field $\Omega_s(t)$. In this case the c_a mode remains unpopulated and we neglect it. Next, we shift the driven mode, $c_s \rightarrow \alpha + c_s$, by the classical amplitude α , yielding an effective ME for c_s , b_1 and b_2 . Finally, we adiabatically eliminate the c_s mode, valid in the limit $|\alpha| \sim \mathcal{O}(1)$ and $(g_0^2|\alpha|/4\delta) \ll |\Delta_s + i\kappa|$, to obtain an effective ME for the mechanical modes (see Appendix B for more details),

$$\begin{aligned} \dot{\rho}_m = & -i[H_m + \Lambda(b_1^\dagger b_1 - b_2^\dagger b_2)^2, \rho_m] + \mathcal{L}_\gamma \rho_m \\ & + \Gamma_\phi \mathcal{D}[(b_1^\dagger b_1 - b_2^\dagger b_2)]\rho_m + \frac{\gamma'}{2} \sum_i \mathcal{D}[b_i]\rho_m. \end{aligned} \quad (3.8)$$

Here, $\gamma' = \kappa|\alpha|^2 g_0^2/(2\delta^2)$, and the phonon-phonon interaction and the phonon dephasing rate are given by

$$\Lambda = \frac{g_0^4 |\alpha|^2 \Delta_s}{16\delta^2(\Delta_s^2 + \kappa^2)}, \quad \Gamma_\phi = \frac{g_0^4 |\alpha|^2 \kappa}{16\delta^2(\Delta_s^2 + \kappa^2)}. \quad (3.9)$$

The effective Hamiltonian in Eq. (3.8) describes a phonon nonlinearity with a tunable strength $\Lambda(t) \sim |\alpha(t)|^2$. The relevant cross-coupling is given by

$$H_{\text{int}} \simeq 2\Lambda b_1^\dagger b_1 b_2^\dagger b_2, \quad (3.10)$$

and when acting for a time $t_g = \pi/(2\Lambda)$, this Hamiltonian implements a controlled-phase gate between two qubits encoded in states $|0_m\rangle$ and $|1_m\rangle$. During this time, phonons experience intrinsic and optically-induced decoherence as seen in Eq. (3.8). In Fig. 3.4, we plot the resulting gate error $\epsilon_g = 1 - \langle \psi_0 | \rho_m(t_g) | \psi_0 \rangle$ for an initial state $|\psi_0\rangle = \frac{1}{2}(|0_m\rangle + |1_m\rangle)^{\otimes 2}$ optimized with respect to Δ_s . Using the total decoherence rate of this state, $\Gamma_{\text{decoh}} = 2\Gamma_m + \Gamma_\phi + \gamma'/2$, we find that $\epsilon_g \propto \Gamma_{\text{decoh}}/\Lambda$ is minimized for $|\Delta_s| \simeq g_0/2$, where $\epsilon_g \propto 4(\kappa/g_0)$. While this scaling with g_0 is weaker than for a gate based on photon reflection (see Eq. (3.6)), the ability to perform a gate between stationary qubits represents an important advantage of this approach.

3.7 Conclusions

We have described single-photon and single-phonon nonlinear effects in strongly coupled multimode OMSs. We have shown how induced nonlinearities on or near resonance can be used for controlled quantum gate operations between flying optical or stationary phononic qubits. Our results provide a realistic route towards the quantum nonlinear regime of OMSs, and a framework for future OM information processing applications.

Chapter 4

Heralded Quantum Gates with Integrated Error Detection

4.1 Introduction

Exploiting quantum systems for information processing offers many potential advantages over classical information processing like highly secure quantum networks [19, 44, 26] and powerful quantum computers [51, 84, 30]. One of the main challenges for the realization of functional quantum computers is to perform gates with sufficiently high quality so that the remaining errors can be suppressed by error correction codes, which makes the computation fault tolerant [47]. At the same time, applications to long distance quantum communication can be enabled by quantum repeaters, which combine probabilistic entanglement generation over short distances with subsequent entanglement connection steps [26]. For these protocols, the probabilistic nature of the entanglement generation is acceptable, but it is essential that

high fidelity entanglement is achieved conditioned on a heralding measurement. Experimentally, such high fidelity entanglement is often much easier to implement and may be realized in situations where it is impossible to perform any quantum operations deterministically. Here we introduce a similar concept for gate operations and develop the concept of heralded quantum gates with integrated error detection. In the resulting gate, the infidelity, which would be present for a deterministic gate is converted into a failure probability, which is heralded by an auxiliary atom. Once successful, the resulting gate can have an arbitrarily small error. Such heralded gates could facilitate fault tolerant quantum computation since detectable errors may be easier to correct than undetectable errors [36, 71, 98]. Alternatively it can be directly incorporated into quantum repeater architectures for long distance quantum communication.

Optical cavities are ideal for conversion between the stationary gate qubits and flying qubits (photons), which is fundamental for quantum networks [76, 48, 67]. Quantum gates can, in principle, also be directly implemented in optical cavities [66], but the experimental requirements for this are very challenging due to spontaneous emission and cavity loss. The essential parameter quantifying this is the cooperativity of the atom-cavity system, C . It has been argued that directly implementing gates in optical cavities leads to a poor error scaling $1 - F \propto 1/\sqrt{C}$, where F is the fidelity of the gate [42, 85]. However, as a result of the integrated error detection, the heralded gates that we propose exhibit high fidelities when successful. This enables efficient entanglement swapping and removes the necessity of intermediate entanglement purification in quantum repeaters thus increasing the distribution rate

significantly. Compared to using other deterministic, cavity based gates, an increase in the rate of up to two orders of magnitude can be achieved for modest cooperativities (< 100) and a distance of 1000 km [6].

4.2 Heralding gate

The basic idea is to use a heralding auxiliary atom in addition to qubit atoms in the same cavity. One of the atomic qubit states, e.g., state $|1\rangle$ couples to the cavity mode while $|0\rangle$ is completely uncoupled (see Fig. 4.1(a)). Such a system has previously been considered for two-qubit gates [27, 25, 86, 85, 73], multi-qubit gates [27, 106] and photon routing [96]. If any of the qubit atoms is in state $|1\rangle$ the cavity resonance is shifted compared to the bare cavity mode, which can be exploited to make a gate between two or more qubits by reflecting single photons off the cavity [27]. The efficiency of such schemes, however, is limited by photon losses, inefficient detectors and non-ideal single photon sources [96, 73]. We circumvent these problems by introducing an auxiliary atom in the cavity to serve as both an intra-cavity photon source and a detector. As opposed to previous heralded gates in optical cavities, which relied on the null detection of photons leaving the cavity [65, 5, 35], the final heralding measurement on the atom can then be performed very efficiently.

In our approach, the auxiliary atom has two metastable states $|g\rangle, |f\rangle$, which can be coupled through an excited state $|E\rangle$ (see Fig. 4.1(a)). We assume the $|E\rangle \leftrightarrow |f\rangle$ transition to be energetically close to the cavity frequency and to be a nearly closed transition, so that we need to drive the $|g\rangle \rightarrow |E\rangle$ transition, e.g with a two-photon process, (see below). The gate can be understood through the phase evolution

imposed on the atoms. We consider adiabatic excitation of the auxiliary control atom via Stimulated Raman Adiabatic Passage [80, 50], driven by an external driving pulse with Rabi frequency $\Omega(t)$ and a coupling to the cavity photon g_f . In the case when all the qubit atoms are in the non-coupled states $|00..0\rangle$, an adiabatic excitation will result in a dark state $\sim g_f|0,g\rangle - \Omega|1,f\rangle$ with zero energy and vanishing phase. Here the number refers to the number of cavity photons. However, the qubit states Ψ with at least one of the qubit atoms in the coupled state, results in a cavity-induced shift of the state $|1,f,\Psi\rangle$, which in turn, causes an AC Stark shift and dynamical phase to be imprinted into the $|g,\Psi\rangle$ state after the driving pulse is turned off. All states but the completely uncoupled qubit state $|00...0\rangle$ will thus acquire a phase, the magnitude of which depends on the length of the driving pulse. With an appropriate pulse length and simple single qubit rotations, we can use this to realize a general N -qubit Toffoli gate or a control-phase (CZ) gate.

Naively, the gates will be limited by errors originating from cavity decay and spontaneous emission from the atoms, which carry away information about the qubit state. These errors are, however, detectable since the auxiliary atom will be trapped in state $|f\rangle$ if either a cavity excitation or an atomic excitation is lost. Conditioning on detecting the auxiliary atom in state $|g\rangle$ at the end of the gate thus rules out the possibility of any dissipative quantum jumps having occurred during the gate. As a result, the conditional fidelity of the gate is greatly enhanced at the modest cost of a finite but potentially low failure probability.

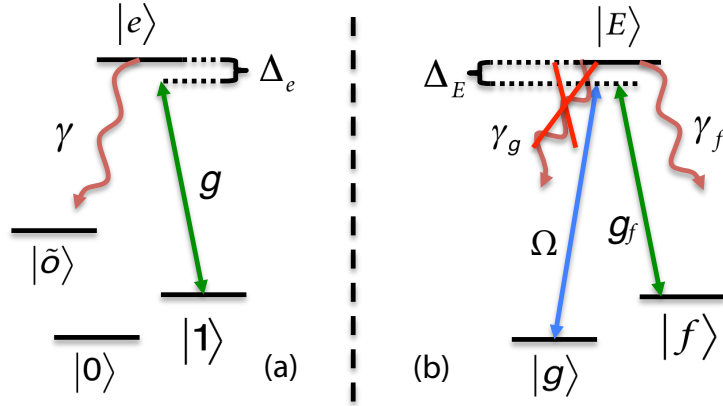


Figure 4.1: (a) Level structure of the qubit atoms. Only state $|1\rangle$ couples to the cavity and we assume that the excited level decays to some level $|\tilde{o}\rangle$, possibly identical to $|f\rangle$ or $|0\rangle$. (b) Level structure of the auxiliary atom and the transitions driven by the weak laser (Ω) and the cavity (g_f). We assume that $|E\rangle \leftrightarrow |f\rangle$ is a closed transition, i.e. $\gamma_g = 0$.

4.3 Performance

4.3.1 Model

We now analyze the performance of the gates and derive the success probabilities, gate times and gate errors (see Tab. S1 in Appendix C) The Hamiltonian in a proper rotating frame is (see Fig. 4.1)

$$\begin{aligned} \hat{H} = & \Delta_E |E\rangle\langle E| + g_f (\hat{a}|E\rangle\langle f| + H.c) + \hat{V} + \hat{V}^\dagger \\ & + \sum_k \Delta_e |e\rangle_k\langle e| + g (\hat{a}|e\rangle_k\langle 1| + H.c), \end{aligned} \quad (4.1)$$

where k labels the qubit atoms ($\hbar = 1$), $2\hat{V} = \Omega|E\rangle\langle g|$ and we have assumed that all couplings (g, Ω) are real. We have defined $\Delta_E = \omega_E - \omega_g - \omega_L$, and $\Delta_e = \omega_e - \omega_g - \omega_L + \omega_f - \omega_1$, where ω_L is the laser frequency and otherwise ω_x is the frequency associated with level x . We describe the cavity decay and atomic spontaneous emission with Lindblad operators so that $\hat{L}_0 = \sqrt{\kappa}\hat{a}$ corresponds to the

cavity decay, $\hat{L}_f = \sqrt{\gamma_f}|f\rangle\langle E|$ to the decay of the excited state of the auxiliary atom and $\hat{L}_k = \sqrt{\gamma}|\tilde{o}\rangle_k\langle e|$ describes the decay of the excited qubit states to some arbitrary ground state $|\tilde{o}\rangle$. The nature of $|\tilde{o}\rangle$ is not important for the dynamics of the gates and it may or may not coincide with $|0\rangle$ or $|1\rangle$.

4.3.2 Effective Hamiltonian

We assume a weak driving pulse justifying for a perturbative treatment of \hat{V} using the formalism of Ref. [74]. In the perturbative description we adiabatically eliminate the coupled excited states of the atoms and the cavity (assuming $\Omega^2/\Delta_E \ll \Delta_E$ and $\Omega \ll g$), which leads to an energy shift of the ground states but otherwise conserves them since the Hamiltonian cannot connect different unexcited states without decay. The dynamics are therefore described by an effective Hamiltonian, $\hat{H}_{\text{eff}} = |g\rangle\langle g| \sum_n \Delta_n \hat{P}_n$ where

$$\Delta_n = \text{Re} \left\{ \frac{-\frac{\Omega^2}{4\gamma}((\frac{\Delta_e}{\gamma}-i/2)i+2nC)}{(2\frac{\Delta_e}{\gamma}-i)((2\frac{\Delta_E}{\gamma}-i)i/4+C)+(2\frac{\Delta_E}{\gamma}-i)nC} \right\} \quad (4.2)$$

and \hat{P}_n projects on the states with n qubits in state $|1\rangle$. For simplicity, we have assumed that the auxiliary atom is identical to the qubit atoms such that $g_f = g$ and $\gamma_f = \gamma$ (see Appendix C for a more general treatment) and we have defined the cooperativity $C = g^2/\gamma\kappa$. We consider the limit $C \gg 1$ and from Eq. (4.2) we find that the energy shift, in the case when all qubit atoms are in $|0\rangle$, becomes very small $\Delta_0 \sim \Delta_E \Omega^2 / (16\gamma^2 C^2) \rightarrow 0$, i.e., we drive into a zero energy dark state as mentioned in the description above. On the contrary, for $n > 0$, the C in the nominator of Δ_n reflects that the coupling of the qubit atoms shifts the cavity resonance and as a result an AC stark shift of $\sim \Omega^2/\Delta_E$ is introduced. Furthermore, we find that in the

effective evolution, errors caused by spontaneous emission or cavity decay ($\hat{L}_0, \hat{L}_f, \hat{L}_k$) project the system out of the effective space into orthogonal subspaces, which allows for an efficient error detection by measuring the ancilla atom.

4.3.3 Success probability

The dynamics described by \hat{H}_{eff} can be used to implement a Toffoli gate. Assuming the qubit atoms to be on resonance ($\Delta_e = 0$) and having $\Delta_E \sim \gamma\sqrt{C}$ gives energy shifts $\Delta_{n>0} \sim \Omega^2/(4\gamma\sqrt{C})$ while $\Delta_0 \sim \mathcal{O}(\Omega^2/C^{3/2})$. Hence, $|00\dots0\rangle$ is the only state, which remains unshifted and we can choose a gate time of $t_{\text{T}} \sim 4\pi\sqrt{C}\gamma/\Omega^2$ to make a Toffoli gate. By conditioning on measuring the auxiliary atom in state $|g\rangle$ at the end of the gate, the detectable errors from cavity decay and spontaneous emission only reduce the success probability instead of reducing the fidelity. Consequently, the fidelity becomes limited by more subtle, undetectable errors (see Appendix C). The dominant error originates from the qubit dependent decay rate, Γ_n , of $|g\rangle \rightarrow |f\rangle$. As we demonstrate in Appendix C), this leads to a fidelity lower bounded by $1 - F \lesssim 0.3/C$, with a success probability of $P_s \sim 1 - 3/\sqrt{C}$. Thus is a substantial improvement over the leading error in the case of deterministic cavity-assisted gates. For generic states, the fidelity can even be markedly higher, and improving with increasing particle number N , see Appendix C.

In the special case of only two qubits, the Toffoli gate is referred to as a CZ-gate, and in this case, we can even improve the gate to have an arbitrarily small error by combining it with single qubit rotations. For the general Toffoli gate discussed above, we needed $\Delta_e = 0$ to ensure the correct phase evolution, but making the single

qubit transformations $|0\rangle \rightarrow e^{-i\Delta_0 t/2}|0\rangle$ and $|1\rangle \rightarrow e^{-i(\Delta_1 - \Delta_0)t/2}|0\rangle$, at the end of a driving pulse of length $t_{\text{CZ}} = |\pi/(\Delta_2 - 2\Delta_1 + \Delta_0)|$, ensures the right phase evolution of the CZ-gate without any constraints on Δ_e . Hence, it is possible to tune Δ_e to eliminate the detrimental effect of having a qubit dependent decay rate. Choosing $\Delta_E = \frac{\gamma}{2}\sqrt{4C+1}$ and $\Delta_e = \frac{1}{2}C\gamma^2/\Delta_E$ ensures $\Gamma_0 = \Gamma_1 = \Gamma_2$, and thus removes all dissipative errors from the heralded gate. The conditional error is then limited only by non-adiabatic effects, that can in principle be made arbitrarily small by reducing the driving strength. The success probability is $1 - P_s \sim 6/\sqrt{C}$ in the limit $C \gg 1$ (see Fig. 4.2). We thus have a heralded two qubit gate with arbitrarily small error with a success probability that can approach 1 (it is possible to decrease the scaling factor of the probability from ~ 6 to ~ 3.4 at the expense of an error scaling as $1/C$ by tuning Δ_E, Δ_e).

4.3.4 Gate time

We now consider the gate time. The gate time of the Toffoli gate is $t_T \sim 4\pi\sqrt{C}\gamma/\Omega^2$ and for the CZ-gate we have $t_{\text{CZ}} \sim 15\pi\sqrt{C}\gamma/(2\Omega^2)$ for $C \gg 1$. Since $t_{\text{CZ}} > t_T$ we focus on t_{CZ} . The gate time is set by the strength (Ω) of the driving pulse, which is limited by non-adiabatic errors. This is investigated in the supplemental material where we also verify our analytical results numerically in Appendix C. Assuming realistic parameters of $\kappa = 100\gamma$ [94, 96], we find that a driving of $\Omega = \sqrt{C}\gamma/4$ keeps the non-adiabatic error of the gate below $4 \cdot 10^{-5}$ for $C \leq 1000$. The gate times decreases as $1/\sqrt{C}$ as shown in Fig. 4.2. For a cooperativity of 100 the gate time is $\approx 1 \mu\text{s}$ for typical atomic decay rates.

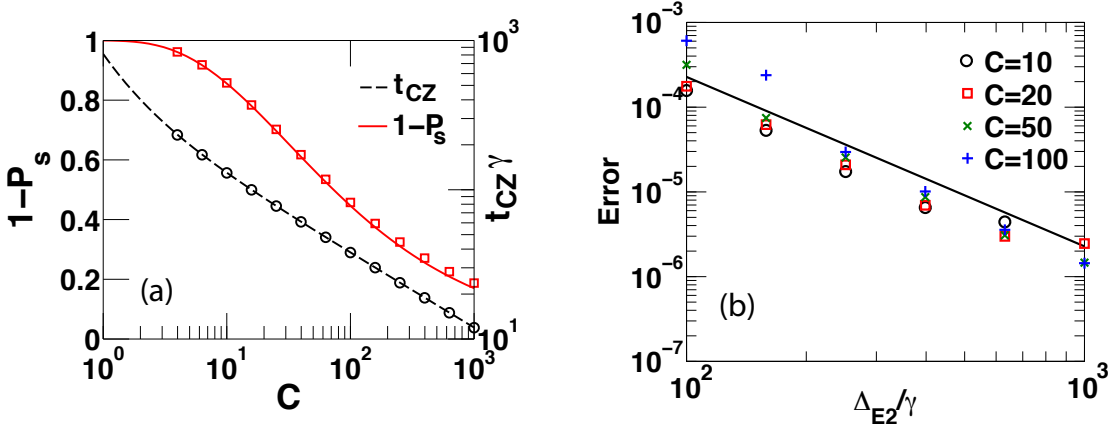


Figure 4.2: (a) Failure probability ($1 - P_s$ - left axis) and gate time (t_{CZ} - right axis) as a function of the cooperativity (C) for the CZ gate. The gate time is in units of the inverse linewidth $1/\gamma$ of the qubit atoms. We have assumed a driving of $\Omega = \sqrt{C}\gamma/4$. (b) Gate error as a function of the detuning Δ_{E2} in the two-photon-driven CZ-gate for $C = 10, 20, 50$, and 100 . We have assumed that $\Omega_{MW} = 4\gamma C^{1/4}$ and that $\gamma_g = \gamma$. The gate error decreases as γ^2/Δ_{E2}^2 and is independent of C . We have assumed $\Omega \sim \Delta_{E2}/8$ resulting in a gate time $\sim 400/\gamma$. Solid/dashed lines are analytical results and symbols are numerical simulations (see Appendix C). For both plots, we have assumed $\kappa = 100\gamma$.

4.4 Additional errors

So far, we have assumed a model where there is no decay from $|E\rangle \rightarrow |g\rangle$. In real atoms, there will, however, always be some decay $|E\rangle \rightarrow |g\rangle$ with a decay rate $\gamma_g > 0$. The result of such an undetectable decay is that both the CZ-gate and the Toffoli gate will have an error $\sim \gamma_g/(\gamma\sqrt{C})$. To make this error small, it is thus essential to suppress the branching ratio γ_g/γ . Below we show how to suppress γ_g by driving the $|g\rangle \rightarrow |E\rangle$ transition with a two photon process. As a result, we realize a CZ gate with an error arbitrary close to zero and a Toffoli gate with an error scaling as $1/C$ even for a realistic atomic system.

Specifically we think of a level structure for the auxiliary atom, shown in Fig. 4.3,

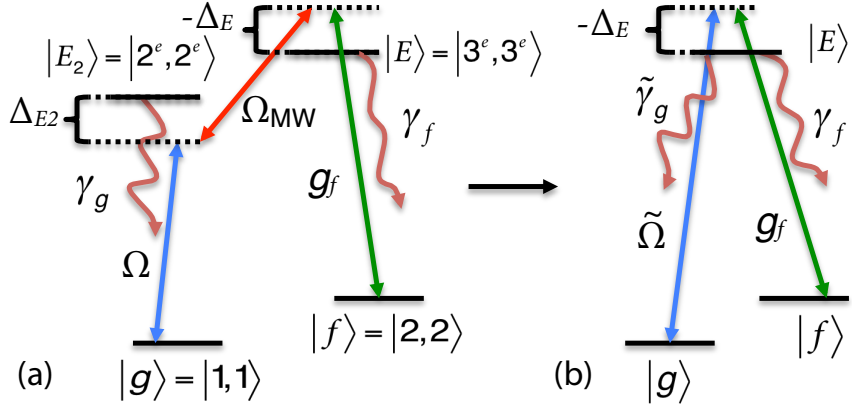


Figure 4.3: (a) Level structure of the auxiliary atom and the transitions driven by a weak laser (Ω), a microwave field (Ω_{MW}) and the cavity (g_f). We assume that $|E\rangle \leftrightarrow |f\rangle$ is a closed transition and, for simplicity, we also assume that $|E_2\rangle \leftrightarrow |g\rangle$ is a closed transition but this is not a necessity. Here $|r^{(e)}, r^{(e)}\rangle$ with $r = 1, 2, 3$ refers to how the atom may be realized in the $(5^2P_{3/2})$ states $|F^{(e)} = r, m^{(e)} = r\rangle$ $5^2S_{1/2}$ of Rb⁸⁷. (b) Effective three-level atom realized by mapping the two-photon drive to give an effective decay rate $\tilde{\gamma}_g$ and an effective drive $\tilde{\Omega}$.

where we still assume $|E\rangle \leftrightarrow |f\rangle$ to be a closed transition. For simplicity, we have also assumed $|E_2\rangle \leftrightarrow |g\rangle$ to be a closed transition. Such a level structure could, e.g. be realized in ⁸⁷Rb as shown in Fig. 4.3. We assume that a microwave field couples the two excited states such that we can have a two photon transition from $|g\rangle \rightarrow |E\rangle$ and that Ω is small, allowing for a perturbative treatment of the coupling. Thus we can map the system to a simple three-level atom with levels $|g\rangle$, $|E\rangle$ and $|f\rangle$ and a decay rate $\tilde{\gamma}_g$ and drive $\tilde{\Omega}$ between $|g\rangle$ and $|E\rangle$, determined by the two photon driving process as shown in Fig. 4.3. The dynamics are thus similar to what we have already described for the simple three level atom except that we have the extra decay $\tilde{\gamma}_g$ that introduces an error in the gates $\sim (\tilde{\gamma}_g/\gamma)/\sqrt{C}$, as previously described. In the limit $C \gg 1$, we find $\tilde{\gamma}_g/\gamma \sim \frac{\gamma_g \Omega_{\text{MW}}^2}{4\gamma \Delta_{E2}^2}$. Thus by increasing Δ_{E2} , we can in principle make these errors arbitrarily small. The error of the CZ-gate for different Δ_{E2} is shown in

Fig. ??, assuming an initial state of $(|0\rangle + |1\rangle)^{\otimes 2}$. Note that in order to prevent an increasing scattering probability of level $|E2\rangle$, we need to have $\Omega_{MW} \propto C^{1/4}$ resulting in a gate error that is independent of the cooperativity, see Appendix C. The success probability and time of the gates are the same as before with $\Omega \rightarrow \tilde{\Omega} \sim \frac{\Omega_{MW}\Omega}{2\Delta_{E2}}$. With similar considerations about the validity of our perturbation as before, we find that for realistic parameters, we can use $\Omega = \Delta_{E2}/8$, $\Omega_{MW} \sim 4\gamma C^{1/4}$ resulting in a gate time of $\sim 10 \mu s$ for typical atomic decay rates and $C \lesssim 1000$, see Appendix C.

4.5 Possible implementation

As an example implementation, we consider ultra-cold ^{87}Rb atoms coupled to nanophotonic cavities [94, 96]. There are some additional errors originating from the extra states in the ^{87}Rb atoms in this case. In Appendix C, we treat these errors and find that with a detuning of $\Delta_{E2} = 100\gamma$ and a cooperativity of $C \approx 100$, a heralded CZ gate with $\sim 67\%$ success probability and a heralded error of $\approx 10^{-3}$ can be realized in $\approx 10 \mu s$ time. This justifies neglecting atomic decoherence which is typically much slower. Alternatively the gate can be implemented with atom-like solid-state qubits such as NV and SiV centers in diamond [18]. These systems can exhibit closed transitions and long-lived electronic spin states which are the essential requirement for the gate [97], while high cooperativities are possible in diamond nanocavities [10]. A particular advantage of such system is the long-lived nuclear spin degrees of freedom, which allows each of the color centers to act as a multi-qubit quantum network node [59]. By entangling electronic spins via the heralded gate, a high-fidelity, fully deterministic gate can subsequently be performed on qubits stored

in nuclear spins [85].

4.6 Application

As a particular application, we consider a quantum repeater where entanglement is first created in small segments (links), which are subsequently connected using entanglement swapping [9]. By organizing the repeater in a tree structure, the probabilistic nature of the gate can be efficiently circumvented. The success rate of distributing entanglement across the total distance L , scales as $\sim (L/L_0)^{1-\log_2(3/p)}$, where $p < 1$ is the success probability of the swap, L is the total distribution distance and L_0 is the length between the links [6] (note that in the limit $p \rightarrow 1$, the above expression underestimates the rate, e.g., for $p = 1$ the actual rate is ~ 3 times faster for 128 links). This is a substantial improvement over direct transmission where the success rate scales exponentially with L . For a realization with nuclear spin memories where the swap can be performed deterministically the rate can scale even better as $\sim \log_2(L/L_0)^{-1}$. In order to maintain the favorable scaling without resorting to time consuming purification, the total number of links, N_{\max} should be kept below $N_{\max} \sim -\ln(F_{\text{final}})/(\epsilon_0 + \epsilon_g)$, where F_{final} is the required fidelity of the final distributed pair and $\epsilon_0, \epsilon_g \ll 1$ are the errors of the initial entanglement generation and the entanglement swapping respectively. Thus, it is essential that the errors are kept small, which can be obtained with the heralded gate.

4.7 Conclusion

In conclusion, we have introduced a heralded two-qubit quantum gate with a conditional fidelity arbitrarily close to unity and an N -qubit Toffoli gate with an error scaling as $1/C$. The gates have a built-in error detection process, which removes the necessity of extracting the error by the more complicated process of entanglement purification or quantum error correction. Our gate is designed for the specific case of optical cavities, and allows exploiting realistic systems for quantum communication, even though the error rate would inhibit this with deterministic gates. Similar advantages can be realised in other systems such as those based on circuit QED, where certain errors could be heralded and thus alleviate the daunting requirements of fault tolerant computation.

Chapter 5

Remote entanglement distribution using individual atoms in cavities

5.1 Introduction

Distribution of entanglement is an essential task in quantum communication [44, 19, 67]. Entanglement can be used to make highly secure communication channels due to the sensitivity of entangled quantum systems to external influences [?]. While this sensitivity makes it possible to detect any attack from an eavesdropper, it also makes it hard to distribute entanglement over large distances since any noise from the environment quickly destroys the entanglement. Direct transmission of a quantum signal suffers from loss and decoherence from the transmission channel, which results in an exponential decrease of the rate with distance [9]. To overcome this problem, it has been proposed to use quantum repeaters, where entanglement is first created over short distances by direct transmission and then stored in quantum memories until it

can be swapped to larger distances [9, 26] (See Fig. 5.1). Much effort has been devoted to the construction of quantum repeaters based on atomic ensembles, where the large number of atoms, in principle, enables highly efficient quantum memories [?, ?]. Nonetheless, the limited efficiencies demonstrated in current experiments with atomic ensembles [?, ?] prevents the construction of a practical quantum repeater based on currently existing setups.

Single emitter systems such as color centers and trapped ions have also been considered for quantum repeaters [?, ?]. The long coherence times demonstrated with, e.g. trapped ions make them desirable as quantum memories. Nonetheless, entanglement needs to be created non-locally between two memories in the initial step of a repeater. This requires efficient transfer of information from the quantum memories onto light in the form of single photons. To this end, it is an advantage to place the emitter inside a cavity, which can greatly enhance the light-emitter coupling [67, 76]. Entanglement swapping can then be performed with a cavity mediated CNOT gate [?, ?] but in this case, the detrimental effect of cavity loss and spontaneous emission from the emitters may prevent obtaining efficient entanglement swapping. The parameter characterizing the effect of dissipation in the emitter-cavity system is the cooperativity, C . It has been argued that a direct implementation of gates in a cavity will make the gate fidelity, F , have a poor scaling of $F \sim 1 - 1/\sqrt{C}$ [42, 85]. To overcome this problem for current cavities with limited C , it has been suggested to employ entanglement purification after each swap operation to boost the entanglement but this either requires a large number of resources or a time consuming sequential generation of purification pairs [?, ?, ?, ?].

Here we analyze and compare a number of cavity-based quantum repeaters which combines various proposals for entanglement generation and cavity-assisted CNOT gates. We find that the best scheme is where high-fidelity entanglement is generated using a two-photon detection scheme similar to Ref. [?] and swapped to large distances using the heralded CZ-gate proposed in Ref. [?]. The heralded gate enables nearly perfect entanglement swapping when successful allowing for many swaps without the need of entanglement purification. As a result, high-rate entanglement distribution is achieved even for low cooperativities.

Compared to the other cavity-based repeaters, this high-fidelity repeater achieves up to two orders of magnitude higher secret key rate (see below) for realistic parameters and large distances (1000 km). Specifically, we have compared to repeaters where entanglement is generated using a single-photon detection scheme similar to Ref. [?], which allows for a better rate at the expense of fidelity. Furthermore we have considered schemes where entanglement swapping is achieved using the deterministic CNOT gate suggested in Ref. [85], combining it with the local entanglement generation scheme of Ref. [86]. The advantage of this gate is that the fidelity scales as $F \sim 1 - 1/C$, which is a significant improvement of the $1/\sqrt{C}$ scaling characterizing the performance of a direct implementation of gates in a cavity. As a result, long-distance entanglement distribution can also be achieved with this gate but it requires cooperativities above 100, which might be challenging to achieve experimentally. Furthermore, we include the possibility of initial purification in repeaters based on the single-photon detection scheme in order to allow for the higher rate of this scheme to compensate for the lower fidelity compared to the two-photon detection scheme.

To reflect a realistic near-term approach to quantum repeaters, we only consider scenarios with 2 or 4 qubits per repeater station. For the same reason, we also do not consider the possibility of intermediate entanglement purification. Here, initial purification refers to purification in the elementary links (see Fig. 5.1) while intermediate purification refers to purification in the subsequent stages of a repeater. We have numerically optimized all the considered repeater schemes for a range of cooperativities and distances to find the highest achievable secret key rate (see below). Note that a similar optimization of repeater schemes based on dynamical programming was described in Ref. [?]. In that work, both initial and intermediate entanglement purification was considered assuming high-fidelity operations. Our optimization is less detailed since we do not consider intermediate purification. On the other hand, we include how the errors of the operations depend on the physical parameters such as the cooperativity and investigate concrete physical implementations. Finally, we compare the high-fidelity repeater considered here to both an ion-trap repeater and one of the best repeaters based on atomic ensembles [?]. For a distance of 1000 km, the high-fidelity repeater outperforms both of these schemes for $C \gtrsim 30$.

5.2 High-fidelity quantum repeater

We will first describe the details of the high-fidelity quantum repeater, which we find to have the best performance and later discuss and compare with the various other schemes. The first step in any quantum repeater is to create non-local entanglement in the elementary links (see Fig. 5.1). To this end, a two-photon detection scheme, as proposed in Ref. [?], is considered. The basic setup is shown in Fig. 5.2(a). Both

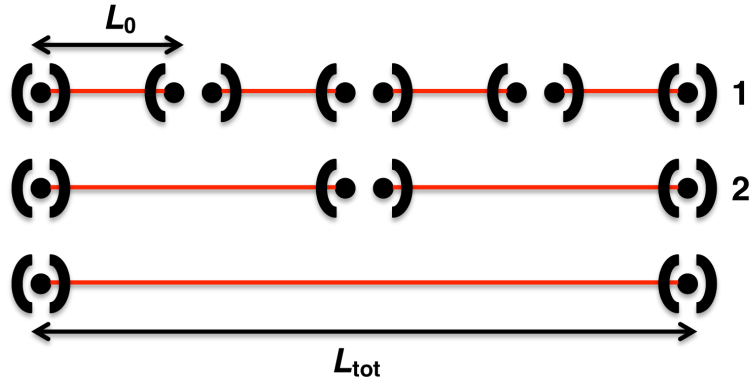


Figure 5.1: The general architecture of a quantum repeater. The total distance, over which entanglement should be distributed, is divided into elementary links of length L_0 connected by repeater stations pictured as cavities containing single emitters. After creating entanglement in the elementary links the entanglement is swapped to larger distances by combining the elementary links. The numbers to the right in the figure refers to the swap level of the repeater. In the first swap level, the four elementary links are connected pairwise to make two longer links. In the second swap levels these two links are connected to create entanglement over the total distance. The total number of swap levels is thus 2 for this depicted setup.

emitters are initially prepared in the excited state $|e\rangle$ by a strong excitation pulse and the cavity is assumed to couple both the $|e\rangle \rightarrow |1\rangle$ and $|e\rangle \rightarrow |0\rangle$ transitions with equal coupling strength $g/\sqrt{2}$ (see Fig. 5.2(b)). The two transitions are, however, assumed to produce photons with different polarizations such that the emission of a cavity photon creates an entangled state between the photon and the emitter of the form $\frac{1}{\sqrt{2}}(|0\rangle|1_1\rangle_L + |1\rangle|1_2\rangle_L)$ where $|1_1\rangle_L$ ($|1_2\rangle_L$) is the single photon state with polarization 1 (2). The probability of one of the emitters to emit a photon of either polarization through the cavity, into an optical fiber transmitting it to the detection stage during a time interval $[0; T]$ is

$$P_{\text{phot}} = \frac{4C}{1+4C} \left(1 - e^{-\gamma(1+4C)T}\right), \quad (5.1)$$

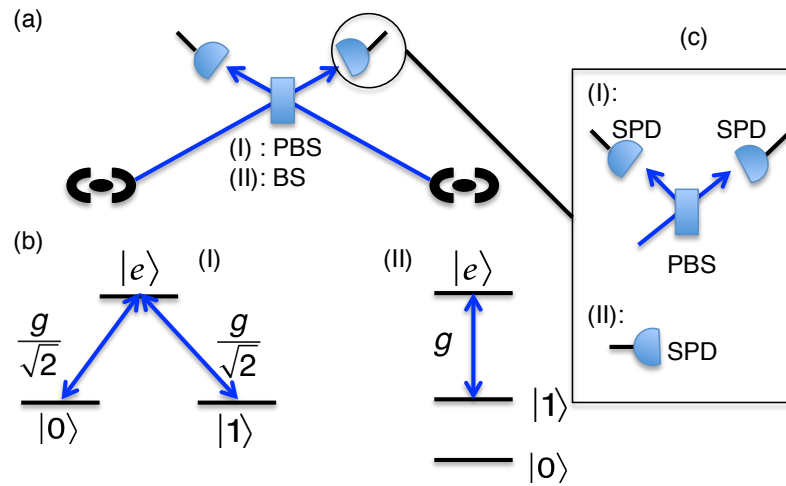


Figure 5.2: Entanglement generation in the elementary links where emission from two cavities are combined on a beam splitter. (a) shows the basic setup, (b) shows the level structure of the emitters and (c) shows the detection setup. (I) refers to the two-photon detection scheme and (II) refers to the single-photon detection scheme. Both schemes use a central station with either (I) three polarizing beam splitters (PBS) and four single-photon detectors or (II) a single balanced beam splitter (BS) and two single-photon detectors. g denotes the cavity coupling. For the two-photon scheme the levels $|0\rangle$ and $|1\rangle$ are assumed to have equal coupling of $g/\sqrt{2}$ to the excited state $|e\rangle$.

assuming perfect outcoupling to the fiber and that the decay rate of the cavity, κ , is much larger than the cavity coupling, g . We have here introduced the cooperativity $C = g^2/\kappa\gamma$, where γ is the spontaneous emission rate of the emitters into modes other than the cavity. This is the key parameter characterizing the performance of the cavity-based repeaters. The photons are sent from the cavities to a central polarizing beam splitter (PBS). If two photons of the same polarizations are incident on the PBS, they leave in different output ports, while photons of different polarization leave in the same output port. The outputs are then sent to a second set of polarizing beam splitters and all four outputs of these are finally measured with single photon detectors (SPD). A click in a detector in each arm heralds the creation of the Bell state $|\Phi^+\rangle = (|00\rangle + |11\rangle)/\sqrt{2}$ between the emitters up to a local qubit rotation. Neglecting dark counts of the detectors, the heralded fidelity is unity (see App. D.2) while the success probability of the scheme is $P_{\text{2click}} = \frac{1}{2}\eta^2 P_{\text{phot}}^2$ with η being the total detection efficiency including inefficient outcoupling of the cavity light, losses in the transmission fibers and imperfect detectors. Compared to schemes based on single-photon detection (see below) the rate of this two-photon detection scheme decreases rapidly with decreasing η . On the other hand it has a high fidelity, which is desirable for the subsequent stages of entanglement swapping as we will show below.

For entanglement swapping we find that the best performance is achieved using the heralded CZ-gate described in Ref. [?]. The gate was described in detail for ^{87}Rb atoms in Ref. [?] but it can be easily generalized to any set of emitters, which have the appropriate level structure (see Fig. 5.3). Note that the gate operation relies on only qubit state $|1\rangle$ coupling to the cavity while the states $|0\rangle$ and $|1\rangle$

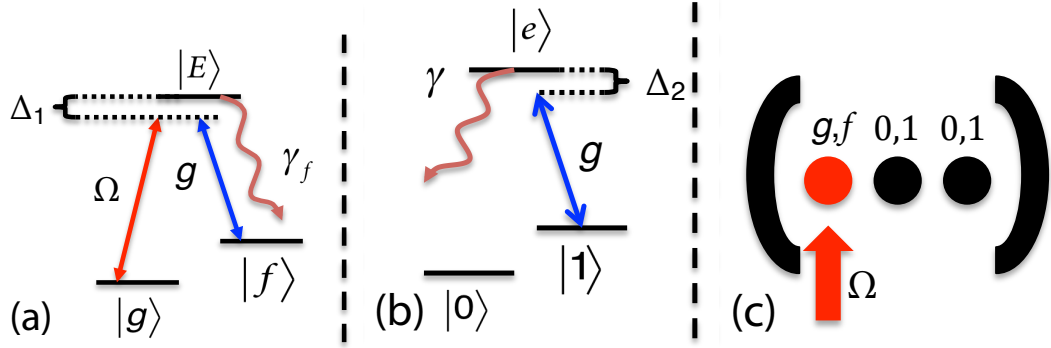


Figure 5.3: Schematics of the heralded CZ gate [?]. (a) is the level structure of the auxiliary atom, (b) is the level structure of the qubit atoms and (c) shows the cavity containing the auxiliary atom and the two qubit atoms. Assuming that $|E\rangle$ only decays to $|f\rangle$ by e.g. driving the transition $|g\rangle \rightarrow |E\rangle$ with a two photon process, any spontaneous emission or cavity decay will change the state of the auxiliary atom from the initial state $|g\rangle$ to $|f\rangle$. The gate is thus conditioned on measuring the auxiliary atom in state $|g\rangle$ at the end of the gate.

had equal cavity couplings in the entanglement generation scheme. To achieve this change in couplings, the state $|0\rangle$ should be mapped to another level in between the entanglement generation and the gate operation. For a realization with alkali atoms where the qubit states would be realized in the hyperfine ground states, this could be achieved by applying a magnetic field to resolve the hyperfine states and applying a microwave pulse resonant with only the $|0\rangle$ state.

In the heralded gate, the cavity is assumed to contain two qubit atoms and one auxiliary atom to facilitate the gate. The auxiliary atom is initialized in a state $|g\rangle$ that does not couple to the cavity and it would therefore not interfere with the entanglement generation scheme. By addressing the auxiliary atom with a weak laser pulse, an AC Stark shift is introduced, which gives a phase that depends on the state of the qubit atoms. Together with single qubit rotations, this enables a CZ-gate between the two qubit atoms. Furthermore, the auxiliary atom can function as an

error detector in the sense that any cavity decay or spontaneous emission changes the state of the atom. Performing a heralding measurement of the state of the auxiliary atom at the end of the driving pulse removes all dissipative errors. As a consequence, the gate gets limited only by non-adiabatic effects. As shown in Ref. [?], a heralded error below $4 \cdot 10^{-5}$ is possible with a gate time of $\sim 377/(\gamma\sqrt{C})$, where γ is the atomic linewidth. The failure probability of the gate scales as $1/\sqrt{C}$ and the high fidelity thus comes at the cost of a finite but possibly low failure probability. A CZ gate combined with single qubit rotations is sufficient to perform direct entanglement swapping. For simplicity, we assume perfect single qubit rotations and 100% efficient measurement of atomic states for all schemes considered. Relaxing this assumption will in general decrease the rate of all the considered repeater schemes but schemes with a high number of swap levels like the high-fidelity repeater will be influenced more on the rate than schemes with a low number of swap levels.

The advantage of the high-fidelity repeater can be understood by considering the requirement for reaching a certain threshold fidelity, F_{final} of the distributed pair. In this case, the maximum number of swap levels is $N_{\max} \sim -\log_2(F_{\text{final}}/(\epsilon_0 + \epsilon_g))$, where $\epsilon_0, \epsilon_g \ll 1$ are the errors of the initial entanglement generation and the entanglement swapping respectively. The combination of the high-fidelity two-photon detection scheme and the heralded gate thus makes it possible to have a repeater with many elementary links while maintaining a high fidelity of the final distributed pair even for low cooperativities since the error of the heralded gate is still high in this regime.

5.2.1 Secret key rate

We imagine that the distributed entanglement is used to generate a secret key between two parties referred to as Alice and Bob. There exist various quantum key distribution schemes [?, ?, ?, ?], however, the general idea is that Alice and Bob can exclude that an eavesdropper has any information about the key by measuring their qubits and comparing results. We will assume that a six-state version of the BB84 protocol described in Ref. [?] is used to generate the secret key. This protocol consists of three main steps. First Alice and Bob picks a basis according to some probability distribution and measure the state of their qubits thereby producing two bit strings referred to as the *raw key*. Afterwards they compare their choice of basis and only keep the bits where they chose the same measurement basis thereby producing a *sifted key*. Finally, Alice and Bob estimate the information that some eavesdropper could possibly have obtained about their key and perform privacy amplification [?]. If the errors are not too big, they can obtain a shorter but completely secure key. For the six-state protocol, the secret key rate, r_{secret} can be defined as

$$r_{\text{secret}} = r_{\text{dist}} p_{\text{sift}} f_{\text{secret}}, \quad (5.2)$$

where r_{dist} is the distribution rate of the entangled pairs, p_{sift} is the probability that Alice and Bob choose the same measurement basis and f_{secret} is the secret key fraction, which depends on the fidelity of the distributed pairs. We assume a worst case scenario where the distributed pairs are Werner states of the form

$$\rho = F|\Phi^+\rangle\langle\Phi^+| + \frac{1-F}{3}\left(|\Phi^-\rangle\langle\Phi^-| + |\Psi^+\rangle\langle\Psi^+| + |\Psi^-\rangle\langle\Psi^-|\right). \quad (5.3)$$

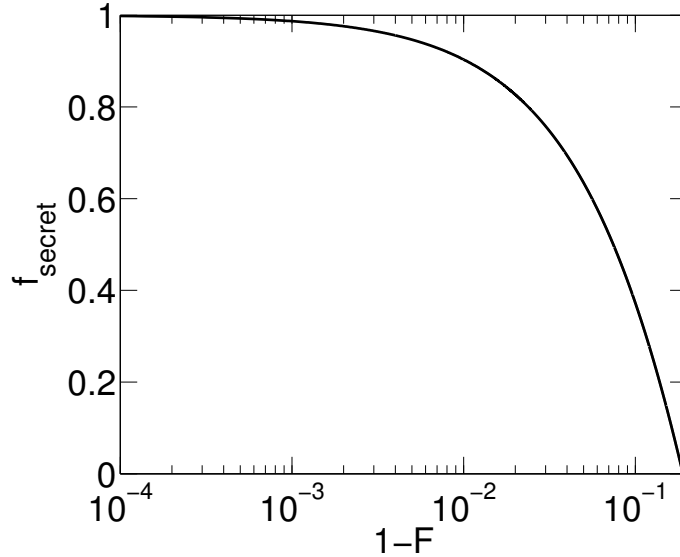


Figure 5.4: Secret key fraction (f_{secret}) as a function of the infidelity, $1 - F$, of the final entangled pair. For $1 - F \gtrsim 19\%$ it is no longer possible to extract a secret key from the raw keys.

For such states, it is shown in Ref. [?] that the secret key fraction in the six-state protocol can be estimated in the limit of infinitely long raw keys to be

$$f_{\text{secret}} = 1 - h(\epsilon) - \epsilon + (1 - \epsilon)h\left(\frac{1 - 3\epsilon/2}{1 - \epsilon}\right), \quad (5.4)$$

where $\epsilon = 2(1 - F)/3$ and $h(p) = -p \log_2(p) - (1 - p) \log_2(1 - p)$ is the binary entropy.

Eq. (5.4) is valid in the limit of perfect sifting and privacy amplification, which we assume to be the case. Furthermore, we assume an asymmetric version of the six state protocol, where one basis is used almost all the time such that $p_{\text{sift}} \approx 1$ [?]. Fig. 5.4 shows how the secret key fraction depends on the fidelity of the distributed pairs. As shown in the figure, high-fidelity pairs are required in order to have a non-vanishing secret key fraction. Again this points to the high-fidelity two-photon detection scheme and the nearly error-free heralded entanglement swapping as the best choice for the repeater.

5.2.2 Repeater architecture

The main goal of the quantum repeater is to overcome the effect of fiber losses. We model the fiber losses with a transmission efficiency $\eta_f = e^{-L_0/2L_{att}}$, where L_0 is the length of the elementary links of the repeater and L_{att} is the fiber attenuation length. η_f enters in the total detection efficiency η as described above. For a given resource of $2^n + 1$ repeater stations, one can either use all stations in a single repeater with n swap levels or one can construct a number of parallel, independently operated chains of repeaters with less swap levels. Increasing the number of swap levels, decreases the fiber losses in the elementary links and thus increases the rate of entanglement generation. If, however, the length of the elementary links is already small, such that, e.g. imperfect SPD dominates the rate, then increasing the number of swap levels does not lead to any improvement. In this case it is advantageous to use the extra repeater stations to make another repeater with less swap levels, which runs in parallel with the already existing one. To make a proper assessment of the performance of repeater one should therefore include that adding swap levels costs resources in the form of additional repeater stations. In our comparison, we therefore consider a normalized secret key rate, $\tilde{r}_{secret} = r_{secret}/(\# \text{ of stations})$, which is the secret key rate divided by the total number of repeater station instead of the bare secret key rate. To evaluate the performance of the repeater we calculate the achievable rate \tilde{r}_{secret} as described in Appendix D.4 with the assumptions summarized in Tab. 5.2 about fiber losses etc.. The resulting rate for various swap level used in the repeater is shown in Fig. 5.5 as a function of distance. As seen in the figure, the optimal number of swap level changes with distance while considering the normalized secret key rate. The rate was

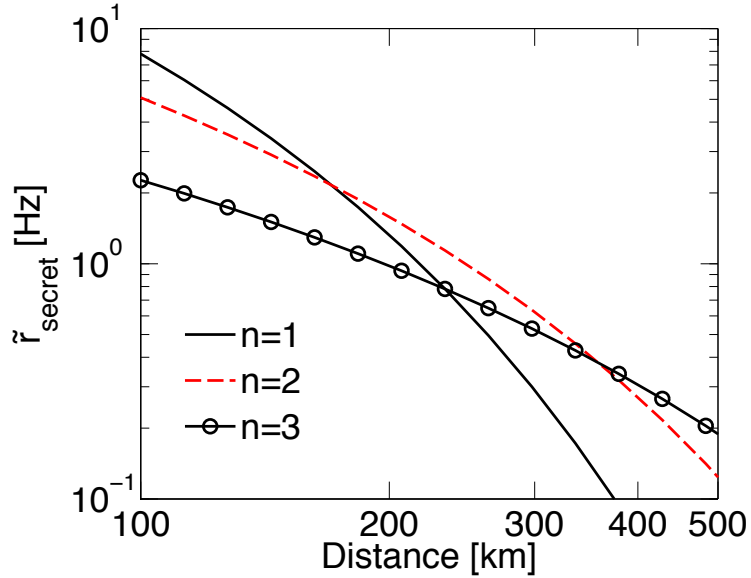


Figure 5.5: Normalized secret key rate per station ($\tilde{r}_{\text{secret}}$) as a function of the distribution distance for a high-fidelity repeater consisting of the two-photon entanglement generation scheme and the heralded gate for entanglement swapping. We have considered $n = 2, 3$ and 4 swap levels and have assumed a cooperativity of $C = 100$ and two qubits per repeater station. The secret key rate was calculated as described in App. D.4 with the assumptions summarized in Tab. 5.2.

calculated as described in App. D.4 for a cooperativity of 100 with the assumptions summarized in Tab. 5.2 about fiber losses, detection efficiencies etc. For distances $\lesssim 150$ km, only a single swap level is needed since the fiber losses are relatively small while more swap levels are needed as the distance increases.

In most repeater schemes, the qubits in each repeater station are assumed to be operated simultaneously with half of the qubits being used to generate entanglement with the neighbouring station to each side such that entanglement attempts in all the elementary links are done simultaneously. We will refer to this as a *parallel* repeater. We will, however, also consider another sequential way of operating the qubits, where all qubits in a station are first used to make entanglement in one elementary link.

After this has been obtained, all but one qubit are then used to make entanglement over the neighboring link in the opposite direction. This is referred to as a *sequential* repeater. The advantage of the sequential repeater is that the rate of the lowest level in the repeater, the entanglement generation, is increased. This comes at the cost of a waiting time between entanglement attempts in neighboring links. As the number of qubits per repeater station increases the sequential repeater will start to outperform the parallel repeater. We find that this happens with 4 qubits per repeater station (see Sec. 5.4).

5.3 Other cavity based repeaters

We have found that the high-fidelity repeater that we have described above outperforms a number of other cavity-based repeater schemes, which can be constructed with different schemes of entanglement generation and CNOT gates. Below, we describe the constituents of these other schemes and compare them to those of the high-fidelity repeater

5.3.1 Single-photon entanglement creation

It has also been suggested to use single-photon detection schemes similar to Ref. [?] to generate entanglement in the elementary links. The setup of a single-photon detection scheme is also shown in Fig. 5.2. We assume that the two emitters are initially prepared in a state

$$(1 - \epsilon^2)|00\rangle + \epsilon^2|ee\rangle + \epsilon\sqrt{1 - \epsilon^2}(|0e\rangle + |e0\rangle) \quad (5.5)$$

by a weak excitation pulse such that the excitation probability is ϵ^2 . An emitter can then go from state $|e\rangle$ to state $|1\rangle$ by emitting a cavity photon. The emitted photons are collected from the cavities and combined on a balanced beam splitter (BS) on a central station between the two cavities. Neglecting losses, the detection of a single photon after the BS will project the state of the emitters into the Bell state $|\Psi^+\rangle = \frac{1}{\sqrt{2}}(|01\rangle + |10\rangle)$ up to a single qubit rotation in the limit $\epsilon^2 \ll 1$ where we can neglect the possibility of double excitations. The probability of an emitter to go from $|e\rangle$ to $|1\rangle$, by emission of a cavity photon during a time interval $[0; T]$, is P_{phot} (see Eq. (5.1)) under similar assumptions as in the two-photon scheme described above. Neglecting dark counts but including losses, the total probability of a single click at the central station is $P_{\text{1click}} = 2\eta P_{\text{phot}}\epsilon^2(1 - \epsilon^2) + (2\eta - \eta^2)P_{\text{phot}}^2\epsilon^4$ with η being the total detection efficiency as for the two-photon scheme. The first term is the probability to emit and detect a single photon while the second term is the probability of emitting two cavity photons but only getting a single click (we assume that we do not have access to number-resolving detectors). The probability, to have a single click and have created the state $|\Psi^+\rangle$, is $P_{\text{correct}} = 2\eta P_{\text{phot}}\epsilon^2(1 - \epsilon^2)$. The average heralded fidelity conditioned on a single click is thus $F_1 = P_{\text{correct}}/P_{\text{1click}}$. To lowest order in ϵ , $F_1 \sim 1 - (1 - \eta/2)P_{\text{phot}}\epsilon^2$ while the success probability is $P_{\text{1click}} \sim 2\eta P_{\text{phot}}\epsilon^2$. There is thus a tradeoff set by ϵ^2 between the success probability and the fidelity for the single-photon detection scheme. This is in contrast to the two-photon detection scheme where $F = 1$ regardless of success probability.

The success probability of the single-photon detection scheme is not as sensitive to the detection efficiency η as the two-photon detection scheme as shown in Fig. 5.6. If

the detection efficiency η is large, the two-photon scheme is desirable since it will have both a high success probability and a high fidelity. However, if η is small, the single-photon scheme will be advantageous since it has a relatively high success probability. Due to the possible high success probability but limited fidelity of the single-photon scheme, it might be desirable to combine it with entanglement purification to increase the final fidelity. In this way the higher success probability of the single-photon scheme may compensate the lower fidelity. We have therefore considered the possibility of initial entanglement purification in repeaters based on the single-photon detection scheme as described below.

5.3.2 Initial purification

Based on a detailed analysis of the various errors that limit the fidelity for the single-photon scheme including dark counts of the detectors (see App. D.1 for details), we find that the purification protocol of Ref. [?] effectively corrects for the errors in the single-photon scheme and we assume that this is used for the initial purification. However, as pointed out in Ref. [?] an improved fidelity, at the expense of a factor of ~ 2 in the success probability, can be obtained by only accepting outcomes where the two heralding qubits are found in state $|1\rangle|1\rangle$ instead of also accepting $|0\rangle|0\rangle$ outcomes. We will also consider this modification to the purification protocol in Ref. [?]. The protocol relies on a CNOT operation, which we assume to be made with the same gate used to perform the subsequent entanglement swapping (see below). To reflect the most realistic near-term quantum repeaters we consider at most 4 qubits per repeater stations. We therefore assume that the purification is performed in a

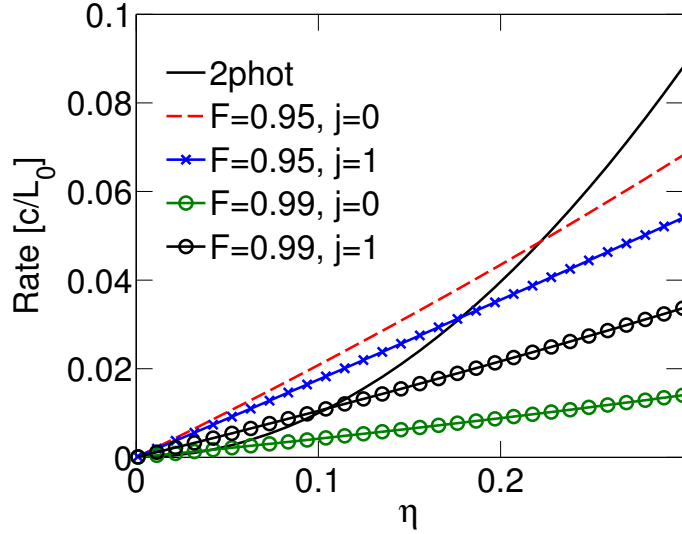


Figure 5.6: Rate of entanglement generation for the two-photon scheme and the single-photon scheme with target fidelity $F \geq 0.95$ and $F \geq 0.99$ both without purification ($j = 0$) and with one round of purification ($j = 1$). The rate is shown as a function of the total detection efficiency η . We have neglected dark counts and assumed that the CNOT gate is deterministic and have perfect fidelity. The rate has been calculated as described in App. D.4. Furthermore, we have assumed that each repeater station contains 4 qubits, which are either used for purification or to increase the rate of the entanglement generation.

pumping scheme [?], where the fidelity of a single pair is pumped by combining it with pairs of lower fidelity since this requires the lowest number of qubits per station.

The effect of combining the single-photon scheme with initial purification is shown in Fig. 5.6 where, for simplicity, the purification is assumed to be performed with a deterministic gate with perfect fidelity and without the modification of Ref. [?]. If high fidelity pairs are desired for, e.g., a repeater with many swap levels, entanglement purification can increase the rate of the entanglement generation. For high collection efficiencies it is, however, desirable to use the two photon scheme since this has a higher rate. In particular the two photon scheme becomes desirable if high fidelity pairs are required.

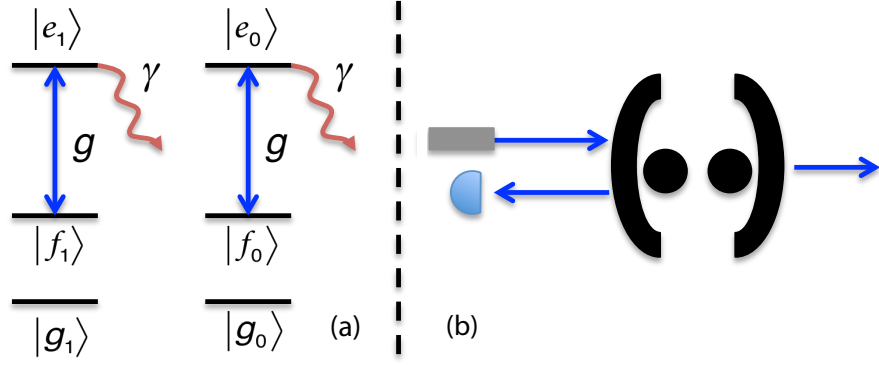


Figure 5.7: Deterministic gate based on reflection and teleportation based CNOT operation [86, 85](a) Level structure of the qubit atoms. The levels $|r_0\rangle$ and $|r_1\rangle$ where $r = g, f$ or e are assumed to be degenerate such that the quantum information is encoded in the horizontal degrees of freedom. (b) The setup to create entanglement between the level states $|g\rangle, |f\rangle$ of the atoms. Weak coherent light is sent onto the cavity and any reflected light is measured with a SPD.

5.3.3 CNOT gates

In our analysis, both the initial purification and the subsequent entanglement swapping involves a cavity-based CNOT gate. Besides the heralded CNOT gate used in the high-fidelity repeater, which we will refer to as *gate 1*, a deterministic cavity-based gate proposed in Ref. [85] could be used. Combining the gate scheme of Ref. [85] with the local entanglement generation scheme of Ref. [86] results in a deterministic CNOT gate with an error scaling as $1/C$. We will refer to this gate as *gate 2*. This gate does not require an auxiliary atom as gate 1 but rather two auxiliary levels in the qubit atoms as shown in Fig. 5.7(a). In this scheme, the quantum information is stored in the horizontal/qubit degree of freedom (subscripts 0 and 1) and the vertical/level degree of freedom (denoted g and f) is used to make an entanglement assisted CNOT gate between the atoms. Separating the qubit degree of freedom from

the level degree of freedom, the gate works by ideally making the transformation

$$|q1\rangle|q2\rangle \otimes |gg\rangle \rightarrow |q1\rangle|q2\rangle \otimes \frac{1}{\sqrt{2}}(|gf\rangle + |fg\rangle), \quad (5.6)$$

where $|g\rangle, |f\rangle$ denote the vertical states and $|q1\rangle$ ($|q2\rangle$) is the qubit state of the first (second) qubit, which could be entangled with atoms at neighboring repeater stations. The entanglement between the levels $|g\rangle$ and $|f\rangle$ can be used to make a CNOT gate, if the levels of the atoms can be measured non-destructively, i.e. without revealing any information about the qubit state as described in Ref. [85]. Both the transformation shown in Eq. (5.6) and the non-destructive measurements can be obtained by sending a weak coherent pulse onto a two-sided cavity and detecting any reflected light (see Fig. 5.7(b) and App. D.3). If the light is resonant with the empty cavity mode, atoms in $|f\rangle$ will shift the cavity resonance. Consequently, photons will be reflected and constitutes a QND measurement of the presence of atoms in $|f\rangle$. Spontaneous emission from the atoms will limit the fidelity of the gate to $F \sim 1 - 1.2/(\eta_a C)$, where η_a is the detection efficiency and $C = g^2/\kappa\gamma$ is the cooperativity. The gate time is limited by the time of the single qubit rotations and the coherent pulses. We assume that this gives a gate time on the order of $10 \mu s$.

As a benchmark, we also consider a naive approach where a direct gate between two qubits is made in a cavity without the use of an auxiliary atom or auxiliary atomic states. To characterize such a gate we consider a situation where the setup of gate 1 is used to make a deterministic gate by simply ignoring the heralding condition. We will refer to this gate as *gate 3*. For such a gate, we find that the gate fidelity will scale as $1 - F \sim 3/\sqrt{C}$ and the time of the gate will be limited by the time of the single qubit rotations which we assume to be $\sim 10 \mu s$.

Gate	Fidelity	Probability	Gate time
1	$F = 4 \cdot 10^{-5}$	$P_g \sim 1 - 6/\sqrt{C}$	$377/(\gamma\sqrt{C}) + 10 \mu\text{s}$
2	$F \sim 1 - 1.2/(\eta_d C)$	$P_g = 1$	$10 \mu\text{s}$
3	$F \sim 1 - 3.6/\sqrt{C}$	$P_g = 1$	$10 \mu\text{s}$

Table 5.1: The characteristics of the three gates considered for the cavity-based repeaters. C is the cooperativity of the atom-cavity system and η_d is the single photon detection efficiency in gate 2. The time of the single qubit rotations is assumed to be $10 \mu\text{s}$.

The characteristics of the three gates we consider are summarized in Tab. 5.1 and illustrated in Fig. 5.8. It is clear, that a repeater based on gate 3 will never be advantageous but we consider it as a reference since the physical requirements for implementing this gate are less than for gate 1 and 2, which requires either an auxiliary atom or auxiliary atomic levels.

5.4 Numerical optimization

We have numerically optimized the secret key rate per repeater station for both the high-fidelity repeater and all other cavity-based repeaters consisting of the elements considered in Sec. 5.3. The secret key rate is calculated as described in Sec. 5.2.1 and App. D.4. It depends on some experimental parameters such as the efficiency of single photon detectors, dark count rates etc. The values of these parameters are assumed fixed and are thus not part of the optimization. All the experimental parameters are summarized in Tab. 5.2 together with the values assumed in the optimizations. We have assumed fiber transmission losses for telecom wavelengths, which may require

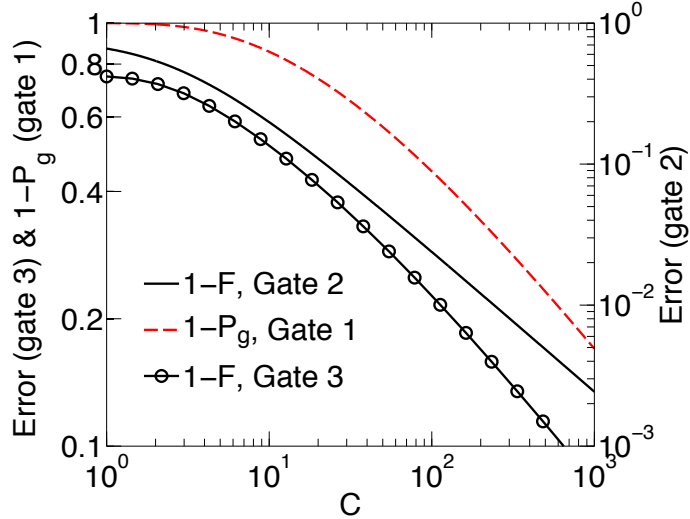


Figure 5.8: Characteristics of the three gates described in the text. The errors of gate 2 (black/solid line, right axis) and gate 3 (black/circled line, left axis) are shown as a function of the cooperativity. The error is defined as $1 - F$ where F is the fidelity of the gate. We have assumed $\eta_d = 0.5$ for the error of gate 2. Gate 1 has conditional fidelity ~ 1 but a finite failure probability $1 - P_g$ which is also shown as a function of cooperativity (red/dashed line, left axis).

wavelength conversion techniques [?]. The free parameters in the optimizations are the number of swap levels, the number of purifications with/without the modification of Ref. [?] and whether a parallel or sequential repeater protocol is used. In the optimizations, we calculate the secret key rate on a grid of all these parameters and pick the combination giving the highest rate. Fig. 5.9 shows a specific example where the combination of the single-photon scheme with gate 2 is investigated for a parallel repeater and a cooperativity of 100. The number of swap levels and purifications, giving the highest rate for a specific distance, can be directly read off from the figure. The same calculations are then done for a sequential repeater protocol and compared to the parallel repeater protocol with/without the modified purification in order to find the highest rate for this specific combination of entanglement generation scheme and

Parameter	Value	Description
γ	$2\pi \cdot 6$ MHz	Spontaneous emission rate of atoms. This enters in the probability of emitting a photon in the entanglement generation schemes (see Eq. (5.1)) and in the gate time of gate 1 and 2.
η_d	50%	Combined efficiency of SPD detectors and outcoupling of light from the cavities. This enters in the total detection efficiency η in the entanglement generation schemes since $\eta = \eta_d \eta_f$. It also enters the fidelity of gate 2.
L_{att}	22 km	Attenuation length of the fibers. The total transmission probability over a length L is assumed to be $\eta_f = e^{-L/L_{att}}$. The value assumed corresponds to telecom wavelengths.
τ_{local}	10 μ s	Time of local qubit operations
r_{dark}	25 Hz	Dark count rate of SPD detectors. We include dark counts in the entanglement generation step but not in the gate operations since the gate operations are assumed to be fast.
c	$2 \cdot 10^5$ km/s	Reduced speed of light in the transmission fibers [?].

Table 5.2: Experimental parameters which influence the rate and fidelity of the repeaters. The second column gives the values used in all optimizations.

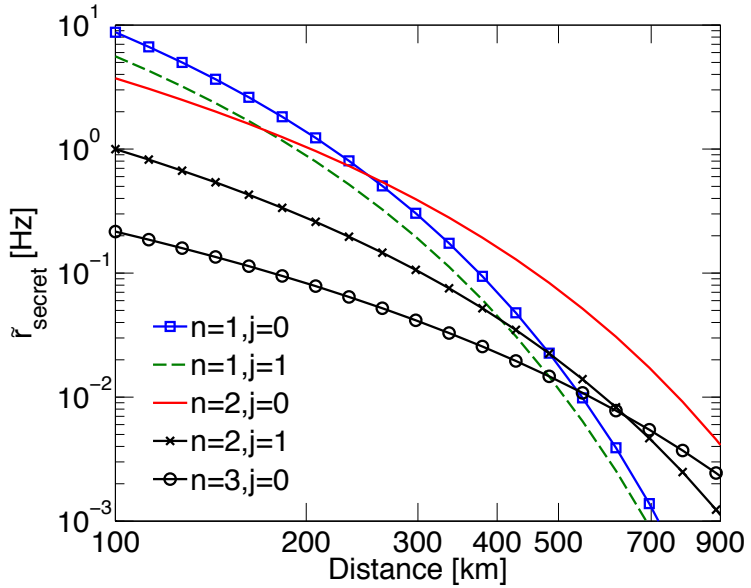


Figure 5.9: Normalized secret key rate per station (\tilde{r}_{secret}) as a function of the distribution distance (Distance) for a parallel repeater based on the single photon generation scheme and gate 2. The cooperativity was assumed to be 100 and we assumed 4 qubits per repeater station. The optimal number of swap levels (n) and purification rounds (j) for a given distance can be directly read off from the plot as the combination giving the highest rate. Note that because the gate fidelity is limited, curves with $j = 2$ and $n = 3, j = 1$ are not shown since they result in a much lower secret key rate. The purification schemes was considered to be without the modification of Ref. [?].

CNOT gate. This is done for all combinations of entanglement generation schemes and CNOT gates. The optimal evolution time, T , and excitation probability, ϵ , in the entanglement generation schemes are found for each grid point using a built-in numerical optimization in the program MATLAB. The key parameter, determining the performance of the CNOT gates, is the cooperativity (see Tab. 5.1). We therefore optimize for cooperativities $C \in [10; 1000]$ and distances between 100 km and 1000 km. Finally, the optimizations are performed for both 2 qubits per repeater station and 4 qubits per repeater station. Note that the auxiliary atom used in gate 1 is not counted as a qubit and schemes based on this gate thus in principle contain an additional atom per repeater station.

We model the effect of the non-perfect gates, as depolarizing channels such that the output of a gate operation described by a unitary $U_{\mathcal{S}}$ working on a set \mathcal{S} of two qubits is

$$\tilde{\rho} = F' U_{\mathcal{S}} \rho U_{\mathcal{S}}^\dagger + \frac{1 - F'}{4} (\text{Tr}\{\rho\}_{\mathcal{S}} \otimes \mathbb{1}_S), \quad (5.7)$$

where $F = F' + (1 - F')/4$ is the fidelity of the gate, $\mathbb{1}_{\mathcal{S}}$ is the identity matrix of the set, $\text{Tr}\{\dots\}_{\mathcal{S}}$ is the trace over the set and ρ is the initial density matrix describing the system before the gate operation. We use Eq. (5.7) to propagate the density matrix from the entanglement generation (see App. D.1-D.2) through the steps of initial purification and entanglement swapping and calculate the average fidelity of the distributed pairs. To calculate the secret key fraction, we treat the distributed pairs as Werner states as described in section 5.2.1.

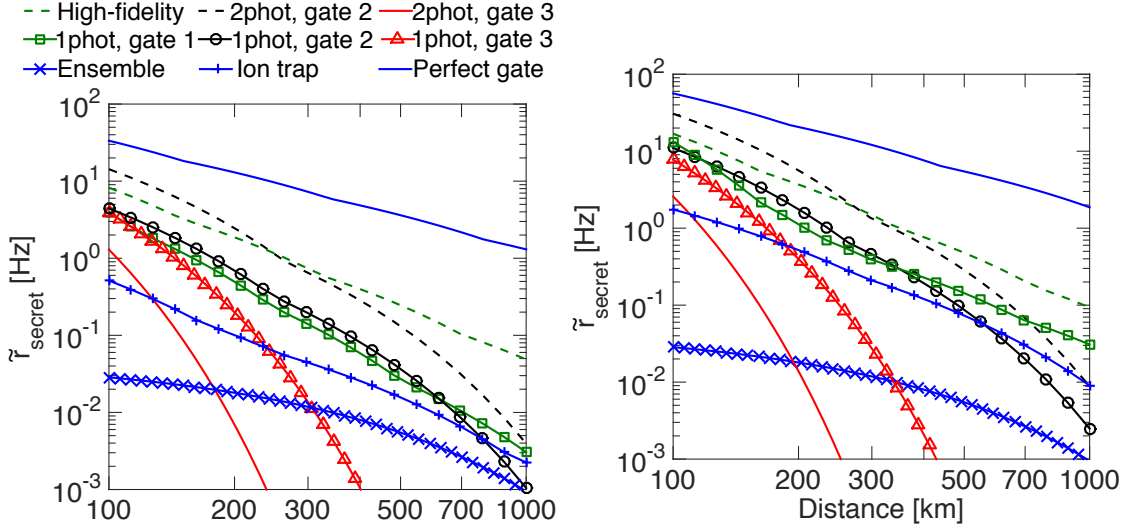


Figure 5.10: Normalized secret key rate per station ($\tilde{r}_{\text{secret}}$) as a function of the distribution distance (Distance) for the high-fidelity repeater and other cavity-based repeaters assuming a cooperativity of $C = 100$. (a) is for 2 qubits per repeater station while (b) is for 4 qubits per repeater station. The other cavity-based repeaters are labelled as, e.g., “1phot, gate 2”, which indicates that it is a repeater based on the single-photon detection scheme and gate 2. The rate of an ensemble-based repeater (“Ensemble”) is also shown [?]. For simplicity, we have assumed a fixed number of four swap levels in the ensemble-based repeater even though a smaller number of swap levels might increase the rate for small distances ($\lesssim 400$ km). Finally, we have plotted the rate of an ion trap repeater scheme (“Ion trap”) with a collection efficiency of 10% and gate fidelity of 99.3% and the ultimate rate obtainable with perfect deterministic gates and perfect entanglement generation with the two-photon scheme (“Perfect gate”) for comparison. For the ion trap repeater we have plotted the highest rate obtainable with either the one-photon or two-photon scheme.

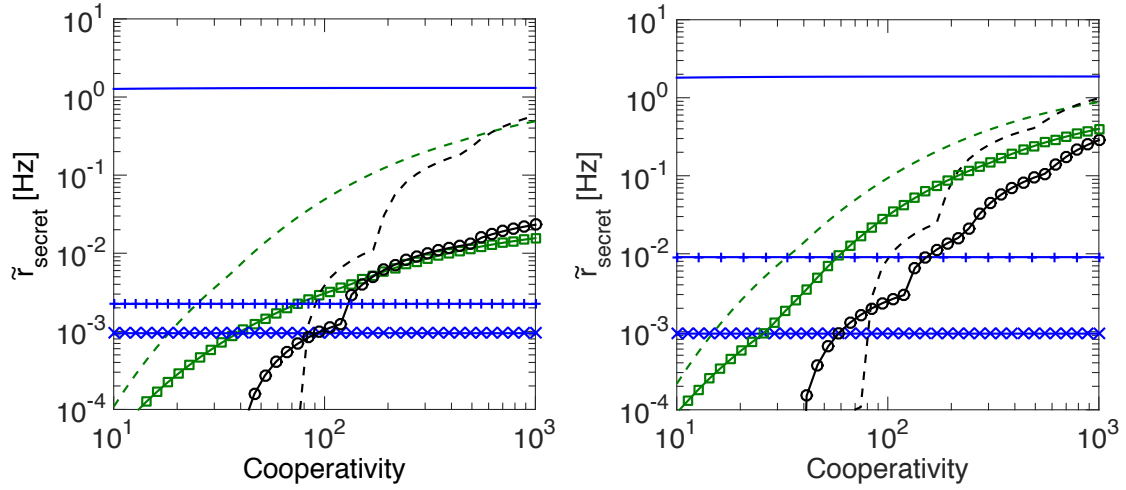


Figure 5.11: Normalized secret key rate per station ($\tilde{r}_{\text{secret}}$) as a function of the cooperativity (C) for the high-fidelity repeater and other repeaters assuming a distribution distance of 1000 km. (a) is for 2 qubits per repeater station while (b) is for 4 qubits per repeater station. The labels are the same as in Fig. 5.10

The secret key rates per repeater station of the high-fidelity repeater and the other cavity-based repeaters are shown in Fig. 5.10 for distances $[100; 1000]$ km and a cooperativity of 100 and in Fig. 5.11 for a distance of 1000 km and cooperativities in the interval $[10; 1000]$. As shown in Fig. 5.10, the repeaters based on gate 3 are simply not able to distribute entanglement over large distances for realistic cooperativities. As a consequence, repeaters based on gate 3 do not appear on Fig. 5.11 since their secret key rate is simply too low.

In general, the high-fidelity repeater (2-photon, gate 1) achieves the highest secret key rate for a broad range of cooperativities and long distances $\gtrsim 300$ km. This reflects both that this protocol allows for a higher number of swap levels and that the secret key rate favors the distribution of high-fidelity pairs since these gives the highest secret fraction (see Fig. 5.4). It is also apparent from Fig. 5.11 that while

repeaters based on gate 2 need cooperativities above 100 for a distance of 1000 km, repeaters based on gate 1 are able to function with much lower cooperativities around $30 - 40$. This is because the heralded gate has nearly unit fidelity independent of the cooperativity. For high cooperativities and/or low distances, a repeater based on the two-photon detection scheme and gate 2 can give a slightly higher secret key rate than the high-fidelity repeater. This improvement is, however, less than a factor of 2 in the secret key rate. The steps in the rates of the schemes based on gate 2 in Fig. 5.11 originate from the fact that as the cooperativity increases, the fidelity of gate 2 increases and at some point the fidelity is high enough to allow for another swap level, which makes the rate increase abruptly. From the optimizations, we find that the sequential repeater architecture achieves slightly higher rates (less than a factor 2) than the parallel repeater architecture for 4 qubits per repeater station, while the opposite is the case for 2 qubits per repeater station.

In general, repeaters based on the two-photon detection schemes outperform repeaters based on the single-photon detection scheme except for repeaters based on gate 3. This reflects that repeaters based on gate 3 cannot perform many swap levels since the fidelity simply decreases too rapidly with the number of swap levels. The result of the optimization was that no swap levels were actually preferred for repeaters based on gate 3 for $C \leq 1000$. As a result, the elementary links in these repeaters are long and fiber losses therefore significantly decrease the total detection probability η in the entanglement generation schemes. In the limit of very low η , the one-photon scheme is advantageous since the success probability only depend linearly on η . For the optimizations, we have assumed that the combined efficiency of the SPD detectors

and outcoupling of light from the cavities is $\eta_d = 50\%$. If this efficiency is smaller, repeaters based on single-photon detection may be desirable. We also find that the purification protocol, in general, performs better with than without the modification of Ref. [?]. The improvement is, however, limited to a factor of $\lesssim 2$ for the parameters considered in Figs. 5.10-5.11.

It is important to stress that the rates plotted in Figs. 5.10-5.11, are the secret key rates divided by the total number of repeater stations. The actual distribution rate can thus be obtained by multiplying with the number of repeater stations. For the high-fidelity repeater, we find a secret key rate of ~ 16 Hz over 1000 km for 33 repeater stations and a cooperativity of 1000 assuming 2 qubits per repeater station. For a more modest cooperativity of 100, a secret key rate of ~ 1.5 Hz over 1000 km can be obtained.

We can compare the rate found here to the rate obtainable with repeaters based on atomic ensembles. In Ref. [?] an efficient repeater based on atomic ensembles is described, which achieves one of the highest distribution rates for repeaters based on atomic ensembles [?]. The fidelity of the distributed pair and the distribution rate are derived in Ref. [?] for a repeater with four swap levels corresponding to 17 repeater stations. Based on this, we have calculated the secret key rate assuming an optimistic, basic repetition rate of the ensembles of 100 MHz and memory and SPD efficiencies of 90%. The rate of the ensemble-based repeater is also shown in Figs. 5.10-5.11 for similar assumptions about fiber losses etc. as for the cavity-based repeaters. We have assumed that the repeater uses four swap levels for all distances even though a smaller number of swap levels may be desirable for smaller distances

($\lesssim 400$ km) [?]. For a distance of 1000 km, we find a rate of ~ 0.03 Hz for 33 repeater stations. This shows that repeaters based on individual atoms in cavities may be very promising candidates for realizing efficient quantum repeaters with rates exceeding those obtainable with atomic ensembles. The main reason for this is that very efficient entanglement swapping can be realized in the cavity-based repeaters which greatly enhances the distribution rates for long distances. On the contrary, repeaters based on atomic ensembles and linear optics have an upper limit on the swapping efficiency of 50%.

For comparison we have also considered a repeater based on ion traps where there is no cavity to collect the light. Non-local entanglement can still be created by collecting the emitted light with a lens as demonstrated in Ref. [?] where a collection efficiency of 10% was reported. The entanglement swapping can be realized using a gate, which has been demonstrated experimentally with a fidelity of 99.3% and a gate time of $50 \mu\text{s}$ [?]. Note that this fidelity was measured for the generation of a single state in Ref. [?] but we will assume it to be the fidelity of the entanglement swap. The rate of such a ion-trap repeater is shown in Figs. 5.10-5.11 with assumptions about fiber losses etc. summarized in Tab. 5.2. We have assumed a collection efficiency of 10% and as a result, the one photon scheme with modified purification performs better than the two-photon scheme for 4 qubits per repeater station. However for two qubits, where purification is not possible, the two-photon scheme is in general advantageous except for small distances (< 200 km). We have assumed a gate fidelity of 99.3% and have plotted the highest rate obtainable with either the one-photon or two-photon scheme.

It is seen that the high-fidelity repeater outperforms the ion-trap repeater for $C \gtrsim 30$, which is mainly due to the low collection efficiency in the entanglement generation. The ultimate rate obtainable with a repeater with perfect deterministic entanglement swapping and entanglement generation based on the two-photon detection scheme with a collection efficiency set by $4C/(1 + 4C)$ is also shown in Figs. 5.10-5.11 under our assumptions about fiber loss, detection efficiency etc.. A similar repeater was considered in Ref. [?] to demonstrate the feasibility of repeaters based on trapped ions. For $C = 1000$, the high-fidelity repeater achieves only a factor of ~ 2 slower rate than this ultimate limit for a distance of 1000 km.

5.5 Conclusion

In conclusion, we have performed a detailed analysis of quantum repeaters based on individual emitters in optical cavities. We have found that a high-fidelity repeater based on the heralded gate described in Ref. [?] combined with a two-photon detection scheme is the best option over a large parameter regime and enables high secret key rates over large distances even for limited cooperativities < 100 . Compared with a number of other cavity based repeaters it achieves rates, which are up to two orders of magnitude faster for long distances (1000 km) and cooperativities < 100 . For small distances or higher cooperativities, a repeater based on the deterministic CNOT gate described in Ref. [85] combined with a two-photon detection scheme can achieve rates which are slightly higher than the high-fidelity repeater but the improvement is less than a factor of 2.

We have also compared the high-fidelity repeater to the repeater in Ref. [?], which

is based on atomic ensembles. For a distance of 1000 km and $C \gtrsim 20$ the high-fidelity repeater begins to outperform the ensemble-based repeater and an improvement of more than two orders of magnitude in the secret key rate is possible for $C \gtrsim 100$. The main reason for the advantage of the high-fidelity repeater is that entanglement can be swapped very efficiently using the heralded CNOT gate described in Ref. [?]. Consequently, the number of swap levels in the repeater can be increased without the need of intermediate purification which greatly enhances the rate for large distances. A similar advantage could in principle be achieved by resorting to a trapped ion system where efficient gates can be implemented. For current systems, the collection efficiencies are, however, so low that a trapped ion system could be outperformed by a cavity system with a limited finesse of $C \gtrsim 30$. If the collection efficiency could be overcome, e.g. by placing the ions in a cavity with a high cooperativity, the rate can be substantially improved, but with $C > 1000$ the high fidelity repeater investigated here is within a factor of two of this ideal repeater. It should, however, be noted that we have compared schemes with strong physical differences in our analysis. The high-fidelity repeater requires an extra auxiliary atom while auxiliary atomic levels are required to decrease the error of the deterministic cavity-based CNOT gates. The ensemble-based and ion-trap repeaters are also very different physical systems compared to the cavity-based repeaters with individual atoms. The different experimental difficulties in realizing the physical requirements for the various repeater schemes should be included in a more advanced assessment.

Finally, we note that while we have investigated a number of different possible repeater protocols there may be even more advantages procedures. Hence the results

that we have derived here should be seen as lower limits to the achievable communication rates. A particular interesting possibility could be to investigate proposals along the lines of Ref. [?, ?], which also rely on heralding measurements to detect errors during entanglement generation and two qubit operations. Possibly some of the ideas from these schemes could be used to improve the communication beyond what we have found here.

Chapter 6

Heisenberg-Limited Atom Clocks Based on Entangled Qubits

6.1 Introduction

From [43]

Chapter 7

A quantum network of clocks

7.1 Introduction

From [48]

Chapter 8

Entangling collective Rydberg excitations of remote atomic ensembles

8.1 Introduction

From []

Appendix A

Appendices for Chapter 2

A.1 Derivation of reflected mode operator

We obtain the reflected mode operator c_R using input-output relations for a two-sided cavity. By assuming that the two endmirrors have the same transmittivity ($\propto \kappa$), we can write the input-output relation for cavity mode c_a on the driven mirror as

$$c_{a,\text{out}} = \sqrt{\kappa} c_a - c_{a,\text{in}}, \quad (\text{A.1})$$

where $c_{a,\text{in}} = -i\frac{\Omega}{\sqrt{\kappa}}$ is the incoming field operator on the mirror and $c_{a,\text{out}}$ is the output field operator. For direct comparision with c_a we divide by $\sqrt{\kappa}$ and define the reflection mode operator as $c_R \equiv c_{a,\text{out}}/\sqrt{\kappa} = c_a + i\frac{\Omega}{\kappa}$.

A.2 Analytic model

In this appendix we provide the analytic solutions used to calculate one- and two-time correlation functions in steady state. First, one-time correlations are calculated from the steady state solutions of Eqs. (2.13–2.18). We set the time derivatives to zero and solve the equations iteratively, order by order in the weak drive. This procedure yields

$$\bar{A}_{000} \approx 1, \quad (\text{A.2})$$

$$\bar{A}_{100} = -i\alpha \frac{1}{1+4x^2}, \quad (\text{A.3})$$

$$\bar{A}_{011} = -\alpha \frac{2x}{1+4x^2}, \quad (\text{A.4})$$

$$\bar{A}_{200} = -\frac{\alpha^2}{\sqrt{2}} \frac{1+2x^2}{(1+4x^2)(1+6x^2)}, \quad (\text{A.5})$$

$$\bar{A}_{111} = i\alpha^2 \frac{2x}{(1+4x^2)(1+6x^2)}, \quad (\text{A.6})$$

$$\bar{A}_{022} = \alpha^2 \frac{4x^2}{(1+4x^2)(1+6x^2)}, \quad (\text{A.7})$$

where $\alpha = \Omega/\tilde{\kappa}$ ($|\alpha|^2 \ll 1$), $x = g/(4\tilde{\kappa})$ and $\tilde{\kappa} = \kappa - i\Delta$. Using these amplitudes, we can express all equal time averages. The mean photon numbers are

$$\bar{n}_a = |\bar{A}_{100}|^2, \quad (\text{A.8})$$

$$\bar{n}_s = |\bar{A}_{011}|^2, \quad (\text{A.9})$$

$$\bar{n}_R = \left| \bar{A}_{100} + i\frac{\Omega}{\kappa} \right|^2, \quad (\text{A.10})$$

and the photon-photon correlation functions are

$$g_{aa}^{(2)}(0) = \frac{2|\bar{A}_{200}|^2}{|\bar{A}_{100}|^4}, \quad (\text{A.11})$$

$$g_{ss}^{(2)}(0) = \frac{2|\bar{A}_{022}|^2}{|\bar{A}_{011}|^4}, \quad (\text{A.12})$$

$$g_{RR}^{(2)}(0) = \frac{\left| -\left(\frac{\Omega}{\kappa}\right)^2 + 2i\frac{\Omega}{\kappa}\bar{A}_{100} + \sqrt{2}\bar{A}_{200} \right|^2}{\left|i\frac{\Omega}{\kappa} + \bar{A}_{100}\right|^4}. \quad (\text{A.13})$$

To leading order in κ/g these yield Eqs. (2.19–2.24).

At finite temperature we calculate steady state amplitudes within each phonon subspace n similarly in the ansatz of Eq. 2.26. Using the notation $R_\kappa(\omega)$ introduced in Section 2.3.2, the steady state amplitudes within the subspace with n phonons in the optical groundstate are

$$|\bar{A}_{10n}|^2 = \frac{\Omega^2 \sqrt{R_\kappa(0)}}{R_\kappa\left(\frac{g}{2}\sqrt{n+1}\right)}, \quad (\text{A.14})$$

$$|\bar{A}_{01n+1}|^2 = \frac{\Omega^2 g^2 (n+1)}{4R_\kappa\left(\frac{g}{2}\sqrt{n+1}\right)}, \quad (\text{A.15})$$

$$|\bar{A}_{20n}|^2 = \frac{\Omega^4 R_\kappa(g/\sqrt{8})}{R_\kappa\left(g\sqrt{(2n+1)/8}\right) R_\kappa\left(\frac{g}{2}\sqrt{n+1}\right)}, \quad (\text{A.16})$$

$$|\bar{A}_{02n+2}|^2 = \frac{\Omega^4 g^4 (n+1)(n+2)}{32R_\kappa\left(g\sqrt{(2n+1)/8}\right) R_\kappa\left(\frac{g}{2}\sqrt{n+1}\right)}. \quad (\text{A.17})$$

Two-time correlation functions are calculated similarly, using the conditional state after a jump (see Eqs. (2.39) and (2.44)) as the initial condition. For example the unnormalized state after detection of a photon in the c_a mode is $c_a|\psi\rangle = \bar{A}_{100}|000\rangle + \sqrt{2}\bar{A}_{200}|100\rangle + \bar{A}_{111}|011\rangle$. We solve Eqs. (2.13–2.15) for the amplitudes with this state as initial condition. The finite delay correlation of the driven mode is

$$g_{aa}^{(2)}(\tau) = \frac{|A_{100}(\tau)|^2}{|\bar{A}_{100}|^4}. \quad (\text{A.18})$$

in good agreement with the numerics. The correlation of the undriven mode $g_{ss}^{(2)}(\tau)$ is calculated similarly. The unnormalized state after detection in the c_s mode is $c_s|\psi\rangle = \bar{A}_{011}|001\rangle + \bar{A}_{111}|101\rangle + \sqrt{2}\bar{A}_{022}|012\rangle$. Using this as the initial condition we solve Eqs. (2.41–2.43) for the amplitudes in the conditional state. In the limit of $\gamma \ll \kappa$ we obtain

$$g_{ss}^{(2)}(\tau) = \frac{|A_{012}(\tau)|^2}{|\bar{A}_{011}|^4}. \quad (\text{A.19})$$

Appendix B

Appendices for Chapter 3

B.1 Phonon nonlinearities

In Eq. (8) in the main text we have derived an effective master equation (ME) to describe the nonlinear interaction between two phonon modes. In the following we present an alternative, more rigorous, approach, which illustrates the individual approximations made in the derivation of the effective phonon nonlinearity in more detail. We first consider only a single mechanical mode, e.g. $b \equiv b_1$, which also allows us more easily to compare the results with exact numerical calculations of the full model.

B.1.1 Model

We start with the full ME for the two optical modes coupled to a single resonator mode, which in the frame of the driving frequency ω_L can be written as

$$\dot{\rho} = -i[H_0 + H_g + H_\Omega(t), \rho] + \mathcal{L}_{\text{diss}}\rho. \quad (\text{B.1})$$

Here

$$H_0 = \omega_m b^\dagger b - \Delta_s c_s^\dagger c_s - \Delta_a c_a^\dagger c_a, \quad (\text{B.2})$$

and

$$H_g = \frac{g_0}{2} (c_a c_s^\dagger b^\dagger + c_a^\dagger c_s b), \quad (\text{B.3})$$

are the free evolution and the OM coupling, respectively, $H_\Omega(t) = i\Omega_s(t)(c_s^\dagger - c_s)$ is the driving field for the symmetric mode with slowly varying amplitude $\Omega_s(t)$ and

$$\mathcal{L}_{\text{diss}}\rho = \sum_{\eta=s,a} \kappa \mathcal{D}[c_\eta]\rho + \frac{\gamma}{2} \mathcal{D}_{\text{th}}[b]\rho, \quad (\text{B.4})$$

accounts for dissipation. Here we have defined the superoperator $\mathcal{D}_{\text{th}}[b] = (N_{\text{th}} + 1)\mathcal{D}[b] + N_{\text{th}}\mathcal{D}[b^\dagger]$ to describe the coupling to a thermal bath.

B.1.2 Displaced frame

In contrast to the approach outlined in the main text, we now start our analysis with a unitary displacement $U(t)c_s U^\dagger(t) = c_s + \alpha(t)$ where the classical cavity field $\alpha(t)$ obeys

$$\dot{\alpha}(t) = (i\Delta_s - \kappa)\alpha(t) + \Omega_s(t). \quad (\text{B.5})$$

This unitary transformation eliminates the classical driving field and in the new frame the resulting ME can be written as

$$\dot{\rho} = -i[H_{\text{lin}} + H_g, \rho] + \mathcal{L}_{\text{diss}}\rho, \quad (\text{B.6})$$

where $H_\Omega(t)$ has disappeared, but the linear part of the Hamiltonian now contains an additional coupling between the resonator and the anti-symmetric cavity mode,

$$H_{\text{lin}} = H_0 + G(t)c_a b^\dagger + G^*(t)c_a^\dagger b, \quad (\text{B.7})$$

where $G(t) = g_0\alpha(t)/2$. Note that ME (B.6) is still exact and we will use this equation for our exact numerics below.

B.1.3 Hybridized modes

To proceed, we assume that $\alpha(t)$ is constant or slowly varying on the timescale set by the detunings $|\Delta_a + \omega_m^i|$. This allows us to write H_{lin} in its adiabatic eigenbasis

$$H_{\text{lin}} = -\Delta_s c_s^\dagger c_s - \tilde{\Delta}_a C^\dagger C + \tilde{\omega}_m B^\dagger B, \quad (\text{B.8})$$

where the C and B are bosonic operators for the hybridized mechanical and optical modes and $\tilde{\Delta}_a$ and $\tilde{\omega}_m$ are the new eigenfrequencies of H_{lin} for a given $G \equiv G(t)$. We obtain

$$C = \cos(\theta)c_a - \sin(\theta)b, \quad (\text{B.9})$$

$$B = \cos(\theta)b + \sin(\theta)c_a, \quad (\text{B.10})$$

where $\tan(2\theta) = -2|G|/\delta$ and $\delta = -(\Delta_a + \omega_m) = 2J - \omega_m - \Delta_s$. The shifted frequencies are given by

$$-\tilde{\Delta}_a = -\Delta_a - \frac{1}{2} \left(\delta - \sqrt{\delta^2 + 4|G|^2} \right), \quad (\text{B.11})$$

$$\tilde{\omega}_m = \omega_m - \frac{1}{2} \left(\delta + \sqrt{\delta^2 + 4|G|^2} \right). \quad (\text{B.12})$$

We see that by slowly increasing the classical control field $\alpha(t)$, the mechanical mode b is adiabatically converted into a polaronic mode B . For small mixing angles θ the mode still retains its mechanical character, while the finite photonic component is responsible for inducing an effective nonlinearity.

In terms of the hybridized mode operators the dissipative terms can be written as

$$\begin{aligned}\mathcal{L}_{\text{diss}} \simeq & \kappa \mathcal{D}[c_s] + \kappa \cos^2(\theta) \mathcal{D}[C] + \frac{\gamma}{2} \sin^2(\theta) \mathcal{D}_{\text{th}}[C] \\ & + \frac{\gamma}{2} \cos^2(\theta) \mathcal{D}_{\text{th}}[B] + \kappa \sin^2(\theta) \mathcal{D}[B].\end{aligned}\quad (\text{B.13})$$

In particular, we identify an additional optical decay channel with rate $\gamma' = 2\kappa \sin^2(\theta)$ for the B mode. In the following we define as

$$\tilde{\mathcal{L}}_{\gamma} = \frac{\gamma}{2} \cos^2(\theta) \mathcal{D}_{\text{th}}[B] + \frac{\gamma'}{2} \mathcal{D}[B], \quad (\text{B.14})$$

the modified mechanical dissipation Liouvillian. Note that in Eq. (B.13) we have already neglected cross-terms between C and B^\dagger . This is valid in the parameter regime considered below, where κ is small compared to the splitting of these two modes.

Finally, we also express the nonlinear interaction H_g in terms of the hybridized modes and write the result as

$$H_g = H_g^{(1)} + H_g^{(2)} + H_g'. \quad (\text{B.15})$$

Here, the first term is the one of interest

$$H_g^{(1)} = \frac{g_0}{4} \sin(2\theta) (c_s + c_s^\dagger) B^\dagger B, \quad (\text{B.16})$$

and describes the coupling of the c_s mode to the number operator of the B mode. The second term is given by

$$H_g^{(2)} = -\frac{g_0}{2} \sin^2(\theta) (B c_s^\dagger C^\dagger + B^\dagger c_s C), \quad (\text{B.17})$$

and leads to additional corrections. However, for small θ this term is small compared to $H_g^{(1)}$. It can be further reduced if $|\Delta_s - \delta| \gg \Delta_s$. Finally, the last term contains

interactions

$$H'_g = \frac{g_0}{2} \cos^2(\theta) (C c_s^\dagger B^\dagger + C^\dagger c_s B) - \frac{g_0}{4} \sin(2\theta) (c_s + c_s^\dagger) C^\dagger C, \quad (\text{B.18})$$

which can be neglected when either the c_s or the C mode are in the vacuum state.

B.1.4 Adiabatic elimination of the cavity mode

Our goal is now to derive an effective ME for the mechanical degrees of freedom only. To do so, we write the full ME as

$$\dot{\rho} = (\mathcal{L}_0 + \mathcal{L}_1) \rho, \quad (\text{B.19})$$

where

$$\mathcal{L}_0 \rho = -i[H_{\text{lin}} + H'_g, \rho] + \mathcal{L}_{\text{diss}} \rho, \quad (\text{B.20})$$

and

$$\mathcal{L}_1 \rho = -i[H_g^{(1)} + H_g^{(2)}, \rho]. \quad (\text{B.21})$$

The dynamics of \mathcal{L}_0 does not excite the cavity modes, and therefore, in the limit where $\tilde{g} = g_0 \sin(2\theta)/4 \rightarrow 0$ (either g_0 is small or the mixing angle θ is small) the density operator can to a good approximation be written as $\rho(t) = \rho_m(t) \otimes \rho_c^0$, where ρ_c^0 is the vacuum state of the c_s and the C mode. To account for the effects of a small $\mathcal{L}_1 \sim \tilde{g}$ up to second order in perturbation theory we define a projection operator onto this subspace,

$$\mathcal{P} \rho = \text{Tr}_c \{ \rho \} \otimes \rho_c^0, \quad (\text{B.22})$$

and its complement $\mathcal{Q} = \mathbb{1} - \mathcal{P}$. Then

$$\mathcal{P} \dot{\rho} = \mathcal{P} \mathcal{L}_0 \mathcal{P} \rho + \mathcal{P} \mathcal{L}_1 \mathcal{Q} \rho, \quad (\text{B.23})$$

$$\mathcal{Q} \dot{\rho} = \mathcal{Q} (\mathcal{L}_0 + \mathcal{L}_1) \mathcal{Q} \rho + \mathcal{Q} \mathcal{L}_1 \mathcal{P} \rho. \quad (\text{B.24})$$

Up to second order in \tilde{g} we can formally integrate the equation for $\mathcal{Q}\rho$ and obtain

$$\mathcal{P}\dot{\rho}(t) \simeq \mathcal{P}\mathcal{L}_0\mathcal{P}\rho(t) + \mathcal{P}\mathcal{L}_1 \int_0^\infty d\tau \mathcal{Q}e^{\mathcal{L}_0\tau} \mathcal{Q}\mathcal{L}_1\mathcal{P}\rho(t). \quad (\text{B.25})$$

We define by $\rho_m(t) = \text{Tr}_c\{\mathcal{P}\rho(t)\}$ the reduced density operator of the mechanical mode and write the final result as

$$\dot{\rho}_m(t) = (\mathcal{L}_m^{(0)} + \mathcal{L}_m^{(1)} + \mathcal{L}_m^{(2)}) \rho_m(t). \quad (\text{B.26})$$

The first term describes the linear part of the dynamics

$$\mathcal{L}_m^{(0)}\rho_m = -i[\tilde{\omega}_m B^\dagger B, \rho_m] + \tilde{\mathcal{L}}_\gamma \rho_m, \quad (\text{B.27})$$

with a modified frequency and modified decay rates for the B mode. The other two terms are given by

$$\mathcal{L}_m^{(1)}\rho_m = - \int_0^\infty d\tau \text{Tr}_c\{[H_g^{(1)}, e^{\mathcal{L}_0\tau} ([H_g^{(1)}, \rho_m \otimes \rho_c^0])]\}, \quad (\text{B.28})$$

and

$$\mathcal{L}_m^{(2)}\rho_m = - \int_0^\infty d\tau \text{Tr}_c\{[H_g^{(2)}, e^{\mathcal{L}_0\tau} ([H_g^{(2)}, \rho_m \otimes \rho_c^0])]\}. \quad (\text{B.29})$$

B.1.5 Simple perturbation theory

In deriving Eq. (B.26) we have so far only assumed that \tilde{g} is small compared to the typical frequency scales of the dynamics of the c_s mode. For now we will also assume that g_0 is small compared to δ and Δ_s . This allows us to neglect the term H'_g in \mathcal{L}_0 and the cavity correlation functions in Eqs. (B.28) and (B.29) can be evaluated in a straight forward manner. For the action of $\mathcal{L}_m^{(1)}$ we obtain

$$\mathcal{L}_m^{(1)}\rho_m = -i[\Lambda(B^\dagger B)^2, \rho_m] + \Gamma_\phi \mathcal{D}[B^\dagger B], \quad (\text{B.30})$$

where $\Lambda = \text{Im}\{S_{gg}^{(1)}(0)\}$, $\Gamma_\phi = \text{Re}\{S_{gg}^{(1)}(0)\}$ and

$$S_{gg}^{(1)}(\omega) = \tilde{g}^2 \int_0^\infty d\tau \text{Tr}_c \{c_s e^{\mathcal{L}_0 \tau} (c_s^\dagger \rho_c^0)\} e^{-i\omega\tau}. \quad (\text{B.31})$$

We find $S_{gg}^{(1)}(\omega) = \tilde{g}^2 / (-i(\Delta_s + \omega) + \kappa)$ and after inserting back the definition of \tilde{g} in the limit $|g_0\alpha/\delta| \ll 1$ we recover the expressions for Λ and Γ_ϕ given in Eq. (9) in the main text. Similarly we obtain

$$\mathcal{L}_m^{(2)} \rho_m = -i[\delta\omega_m^{(2)} B^\dagger B, \rho_m] + \frac{\gamma^{(2)}}{2} \mathcal{D}[B], \quad (\text{B.32})$$

where $\delta\omega_m^{(2)} = \text{Im}\{S_{gg}^{(2)}(\tilde{\omega}_m)\}$, $\gamma^{(2)} = \text{Re}\{S_{gg}^{(2)}(\tilde{\omega}_m)\}$ and

$$S_{gg}^{(2)}(\omega) = \frac{g_0^2 \sin^4(\theta)}{4} \int_0^\infty d\tau \text{Tr}_c \{c_s C e^{\mathcal{L}_0 \tau} (c_s^\dagger C^\dagger \rho_c^0)\} e^{-i\omega\tau}. \quad (\text{B.33})$$

The small frequency shift $\delta\omega_m^{(2)}$ can be absorbed into the definition of $\tilde{\omega}_m$ and, since $\gamma^{(2)} \approx \gamma' \sin^2(\theta) g_0^2 / (4\delta^2)$, for not too large mixing angles θ , $\gamma^{(2)}$ can always be neglected compared to γ' . All together the final effective phonon master equation is

$$\begin{aligned} \dot{\rho}_m = & -i[\tilde{\omega}_m B^\dagger B + \Lambda(B^\dagger B)^2, \rho_m] + \Gamma_\phi \mathcal{D}[B^\dagger B] \rho_m \\ & + \frac{\gamma}{2} \mathcal{D}_{\text{th}}[B] \rho_m + \frac{\gamma'}{2} \mathcal{D}[B] \rho_m, \end{aligned} \quad (\text{B.34})$$

which is the single resonator version of ME (8) given in the main text.

B.1.6 Corrections

Let us now extend the above result to the case where \tilde{g} is small compared to Δ_s and δ , but the bare interaction g_0 is not. In this case the general expressions in Eqs. (B.28) and (B.29) still apply, but the effect of H'_g must be taking into account when evaluating the correlation functions. To illustrate this, let us assume that g_0

is still small compared to δ . Then, by assuming that the C mode is initially in the ground state, we obtain approximately

$$H_{\text{lin}} + H'_g \approx -(\Delta_s - \Delta_B B^\dagger B) c_s^\dagger c_s, \quad (\text{B.35})$$

where the off-resonant frequency shift is

$$\Delta_B = \frac{g_0^2 \cos^4(\theta)}{4(\tilde{\Delta}_a + \tilde{\omega}_m - \Delta_s)}, \quad (\text{B.36})$$

and can be comparable to Δ_s . Therefore, we must evaluate the correlation function for each phonon number state $|n\rangle$ separately and write the resulting non-linear interaction as

$$\mathcal{L}_m^{(1)} \rho_m = \sum_n n^2 (-i [\Lambda(n)|n\rangle\langle n|, \rho_m] + \Gamma_\phi(n)\mathcal{D}[|n\rangle\langle n|]). \quad (\text{B.37})$$

Here $\Lambda(n)$ and $\Gamma_\phi(n)$ are the imaginary and real part of

$$S_{gg}^{(1)}(\omega = -n\Delta_B) = \frac{n^2 \tilde{g}^2}{-i(\Delta_s - n\Delta_B) + \kappa}. \quad (\text{B.38})$$

We see that in this parameter regime more complicated nonlinearities can occur, but the overall magnitude and the ratio between coherent and dephasing interactions remains the same. In principle, this analysis can be extended to the regime, where g_0 is comparable to δ . However, in this case no simple analytic expressions for $\lambda(n)$ and $\Gamma_\phi(n)$ can be derived and need to be evaluated numerically.

B.1.7 Numerical simulation

To assess the validity of the effective phonon ME we now compare our result with the dynamics of the full OMS. Since we are mainly interested in the relation between the phonon non-linearity and the corresponding dephasing and decay rates,

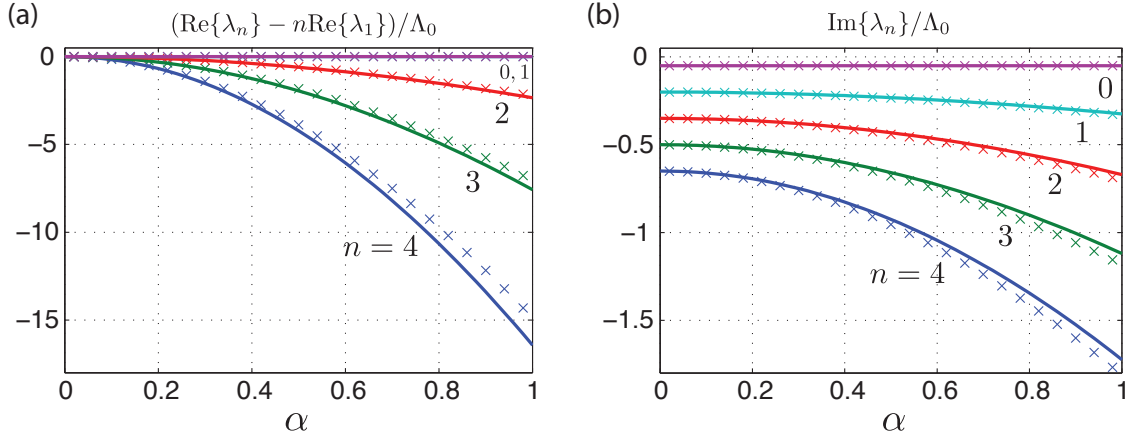


Figure B.1: Comparison of the effective analytic description (Eqs. (B.40), lines) with exact eigenvalues of the Hamiltonian in Eq. (B.39) (crosses) for different cavity field amplitudes α . All results are normalized to the scale $\Lambda_0 = g_0^4/(16 |\Delta_s| \delta^2)$ of the non-linearity. (a) Deviation of the real parts of the eigenvalues from the result expected for a linear oscillator, such that the splitting of the curves indicates an effective non-linearity. (b) Imaginary parts of the eigenvalues corresponding to decays. In both plots we used the parameters $\Delta_s/g_0 = -1$, $\delta/g_0 = 5$, $\kappa/g_0 = 2.5 \times 10^{-2}$, $\gamma_m/g_0 = 2.5 \times 10^{-4}$ and $N_{\text{th}} = 1$.

it is sufficient to evaluate the spectrum of the non-Hermitian Hamiltonian, which for the full model it is given by

$$\tilde{H}_{\text{full}} = H_{\text{lin}} + H_g - i\kappa c_s^\dagger c_s - i\kappa c_a^\dagger c_a - i\frac{\gamma}{2}(N_{\text{th}} + 1)b^\dagger b - i\frac{\gamma}{2}N_{\text{th}}bb^\dagger. \quad (\text{B.39})$$

In Fig. B.1 we plot the real and imaginary parts of the lowest eigenvalues λ_n of \tilde{H}_{full} , which correspond to the lowest number states $|n\rangle$ of the B mode. From the effective phonon model given in Eq. (B.34) and (B.37) we obtain the approximate analytic results

$$\text{Re}\{\lambda_n\} = n\tilde{\omega}_m + n^2\Lambda(n), \quad (\text{B.40a})$$

and

$$|\text{Im}\{\lambda_n\}| = \frac{\gamma}{2}N_{\text{th}} + n \left(\frac{\gamma}{2}(2N_{\text{th}} + 1) + \frac{\gamma'}{2} \right) + n^2\Gamma_\phi(n). \quad (\text{B.40b})$$

We see a good agreement between these results for the effective model and the exact numerics, both for the real and imaginary parts. Although there are some deviations due to higher-order effects, the effective non-linear splitting (Fig. B.1(a)) is much larger than the induced decoherence (Fig. B.1(b)), as is expected for the chosen parameters. Hence, we conclude that the effective model accurately describes the dynamics of the mechanical resonator, and that the effective phonon non-linearity may serve as a basis for gate operations as discussed in the main text and in the following section.

B.2 Phonon-phonon interactions

The derivation of the effective phonon nonlinearity, as outlined above for a single resonator, can be easily adapted to two resonators as discussed in the main text. In this case we have

$$H_0 = \sum_{i=1,2} \omega_m^i b_i^\dagger b_i - \Delta_s c_s^\dagger c_s - \Delta_a c_a^\dagger c_a, \quad (\text{B.41})$$

and

$$H_g = \frac{g_0}{2} \left[c_a c_s^\dagger (b_1^\dagger - b_2^\dagger) + c_a^\dagger c_s (b_1 - b_2) \right]. \quad (\text{B.42})$$

After changing into the displaced representation to eliminate the driving field we obtain the linearized Hamiltonian

$$H_{\text{lin}} = H_0 + \sqrt{2} (G(t) c_a b_a^\dagger + G^*(t) c_a^\dagger b_a), \quad (\text{B.43})$$

where $b_a = (b_1 - b_2)/\sqrt{2}$ and $G(t) = g_0 \alpha(t)/2$. For similar mechanical frequencies $\omega_m^1 \simeq \omega_m^2 = \omega_m$ the symmetric resonator mode is decoupled and we can simply repeat the analysis from above by identifying $b \equiv b_a$ and replacing g_0 by $\sqrt{2}g_0$.

For arbitrary ω_i , we write the linear part of the Hamiltonian in its diagonal form

$$H_{\text{lin}} = -\Delta_s c_s^\dagger c_s - \tilde{\Delta}_a C^\dagger C + \tilde{\omega}_1 B_1^\dagger B_1 + \tilde{\omega}_2 B_2^\dagger B_2. \quad (\text{B.44})$$

As in the single-resonator case the c_s mode is unaffected, but the c_a mode now couples to both b_1 and b_2 . The resulting hybridized modes C , B_\pm depend on the choice of parameters $\omega_m^{1,2}$, Δ_a and G . For the case of interest, i.e. for a symmetric detuning $\omega_m^{1,2} = -\Delta_a \mp \delta$, we obtain

$$C = \cos(2\Theta)c_a - \sin(2\Theta)(B_1 + B_2)/\sqrt{2}, \quad (\text{B.45})$$

$$B_1 = \cos^2(\Theta)b_1 + \sin(2\Theta)c_a/\sqrt{2} - \sin^2(\Theta)b_2, \quad (\text{B.46})$$

$$B_2 = \cos^2(\Theta)b_2 + \sin(2\Theta)c_a/\sqrt{2} - \sin^2(\Theta)b_1, \quad (\text{B.47})$$

where $\tan(2\Theta) = -\sqrt{2}|G|/\delta$. Therefore, for small Θ the modes $B_{1,2}$ correspond to the original mechanical resonator modes $b_{1,2}$ and $\tilde{\omega}_i \approx \omega_m^i$.

As above, we can now re-express the dissipation and the non-linear coupling H_g in terms of C and B_\pm . The modified mechanical dissipation terms are given

$$\tilde{\mathcal{L}}_\gamma = \sum_{i=1,2} \frac{\gamma}{2} \cos^2(2\Theta) \mathcal{D}_{\text{th}}[B_i] + \frac{\kappa}{2} \sin^2(2\Theta) \mathcal{D}[B_i], \quad (\text{B.48})$$

and for small Θ the optical decay rate $\gamma' = \kappa \sin^2(2\Theta)$ is the same as given above and in the main text. Using the decomposition of the non-linear coupling as done in Eq. (B.15), we obtain

$$H_g^{(1)} = \frac{g_0}{\sqrt{8}} \sin(2\Theta) (c_s + c_s^\dagger) (B_1^\dagger B_1 - B_2^\dagger B_2), \quad (\text{B.49})$$

the contribution $H_g^{(2)}$ vanishes and

$$H'_g = \frac{g_0}{2} \cos(2\Theta) (C c_s^\dagger (B_1^\dagger - B_2^\dagger) + \text{H.c.}) . \quad (\text{B.50})$$

We see that the structure and also the relative frequency scales are identical to the corresponding terms discussed for the single resonator above. Therefore, under the same conditions we can eliminate the cavity mode and obtain the effective phonon master equation

$$\begin{aligned}\dot{\rho}_m = & -i \left[\sum_i \tilde{\omega}_i B_i^\dagger B_i + \Lambda (B_1^\dagger B_1 - B_2^\dagger B_2)^2, \rho_m \right] \\ & + \Gamma_\phi \mathcal{D}[(B_1^\dagger B_1 - B_2^\dagger B_2)] \rho_m + \tilde{\mathcal{L}}_\gamma \rho_m.\end{aligned}\quad (\text{B.51})$$

For small Θ this equation reduces to ME (8) in the main text and higher-order corrections can be included in the same way as discussed for the single resonator case.

Appendix C

Appendices for Chapter 4

This appendix describes the details of the perturbation theory and the derivation of the effective Hamiltonian \hat{H}_{eff} and effective Lindblad operators. We describe the situation both with and without a two-photon drive. Furthermore, we present the results of a numerical simulation of the full dynamics of the gates to verify the results found with perturbation theory and address the question of how strong a drive we can allow for. In the end, this determines the gate time as described in the article. Finally we discuss of the additional errors described in the final part of the article.

C.1 Perturbation theory

We will now give the details of the perturbation theory and the derivation of the effective operators together with the success probabilitites, gate times and gate errors (see Tab. C.1). Our perturbation theory is based on the effective operator formalism described in Ref. [74].

Gate	Origin of error	Error	Probability	Time
CZ-gate	$\gamma_g = 0$	0	$\sim 1 - \frac{6}{\sqrt{C}}$	$\sim \frac{15\pi\sqrt{C}\gamma}{2\Omega^2}$
	$\gamma_g > 0$	$\sim \frac{\gamma_g}{\gamma\sqrt{C}}$		
Toffoli	$\Gamma_i \neq \Gamma_j$	$\lesssim \frac{0.3}{C}$	$\sim 1 - \frac{3}{\sqrt{C}}$	$\sim \frac{4\pi\sqrt{C}\gamma}{\Omega^2}$
	$\gamma_g > 0$	$\sim \frac{\gamma_g}{\gamma\sqrt{C}}$		

Table C.1: The errors, success probabilities and gate times of the N -qubit Toffoli gate and the CZ-gate considered in the article. Note that the branching fraction γ_g/γ can be made arbitrarily small using a far detuned two-photon driving as explained in below. Γ_i is the rate of detectable errors for the qubit state with i qubits in state $|1\rangle$. The success probability of the CZ-gate can be increased at the expense of an error scaling of $1/C$ as explained in the article.

First, we treat the simplest situation where the auxiliary atom is directly driven to an excited state $|E\rangle$ by a weak classical drive Ω as shown in Fig. C.1 (reproduced from Fig. 1 in the article). Note that we allow for some decay from $|E\rangle \rightarrow |g\rangle$ with decay rate γ_g as opposed to the situation in the article. We will later consider the situation where this decay rate is suppressed using a two-photon drive. The level structure of the qubit atoms are also shown in Fig. C.1.

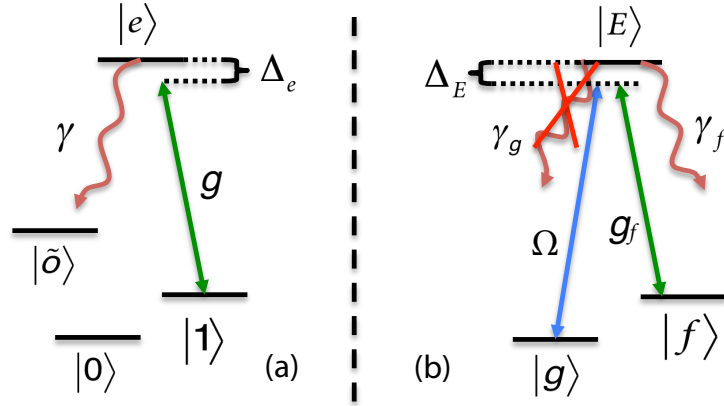


Figure C.1: (a) Level structure of the qubit atoms. Only state $|1\rangle$ couples to the cavity and we assume that the excited level decays to some level $|\tilde{o}\rangle$, possibly identical to $|f\rangle$ or $|0\rangle$. (b) Level structure of the auxiliary atom and the transitions driven by the weak laser (Ω) and the cavity (g_f). We allow for some decay from $|E\rangle \rightarrow |g\rangle$ with decay rate γ_g .

The Hamilton describing the system in a proper rotating frame is given by Eqs. (1)-(3) in the article and is reproduced here

$$\hat{H} = \hat{H}_e + \hat{V} + \hat{V}^\dagger, \quad (\text{C.1})$$

$$\begin{aligned} \hat{H}_e &= \Delta_E |E\rangle\langle E| + g_f (\hat{a}|E\rangle\langle f| + H.c) \\ &\quad + \sum_k \Delta_e |e\rangle_k\langle e| + g (\hat{a}|e\rangle_k\langle 1| + H.c), \end{aligned} \quad (\text{C.2})$$

$$\hat{V} = \frac{\Omega}{2} |E\rangle\langle g|, \quad (\text{C.3})$$

where we have assumed for simplicity that all couplings (g, Ω) are real and k labels the qubit atoms ($\hbar = 1$). We have defined $\Delta_E = \omega_E - \omega_g - \omega_L$, and $\Delta_e = \omega_e - \omega_g - \omega_L + \omega_f - \omega_1$ where ω_L is the laser frequency and otherwise ω_x is the frequency associated with level x . Note that we assume the cavity frequency to be $\omega_c = \omega_L + \omega_g - \omega_f$ such that we are on resonance with the $|g\rangle \rightarrow |E\rangle \rightarrow |f\rangle$ two-photon transition.

The dissipation in the system is assumed to be described by Lindblad operators

such that $\hat{L}_0 = \sqrt{\kappa}\hat{a}$ describes the cavity decay with decay rate κ , $\hat{L}_g = \sqrt{\gamma_g}|g\rangle\langle E|$, and $\hat{L}_f = \sqrt{\gamma_f}|f\rangle\langle E|$ describes the decay of the auxiliary atom and $\hat{L}_k = \sqrt{\gamma}|\tilde{o}\rangle_i\langle e|$ describes the decay of the qubit atoms ($k = 1, 2 \dots N$). As described in the article $|\tilde{o}\rangle$ may or may not coincide with $|0\rangle$ or $|1\rangle$. Assuming that Ω is weak ($\Omega^2/\Delta_E \ll \Delta_E$ and $\Omega \ll g$), we can treat the driving as a perturbation to the system. As shown in Ref. [74], the dynamics of the system is then governed by an effective master equation of the form

$$\dot{\rho} = i \left[\rho, \hat{H}_{\text{eff}} \right] + \sum_x \hat{L}_x^{\text{eff}} \rho (\hat{L}_x^{\text{eff}})^\dagger - \frac{1}{2} \left((\hat{L}_x^{\text{eff}})^\dagger \hat{L}_x^{\text{eff}} \rho + \rho (\hat{L}_x^{\text{eff}})^\dagger \hat{L}_x^{\text{eff}} \right), \quad (\text{C.4})$$

where ρ is the density matrix of the system, \hat{H}_{eff} is an effective Hamiltonian, and L_x^{eff} are effective Lindblad operators with $x = 0, g, f, k$. The effective operators are found from:

$$\hat{H}_{\text{eff}} = -\frac{1}{2} \hat{V}^\dagger \left(\hat{H}_{\text{NH}}^{-1} + (\hat{H}_{\text{NH}}^{-1})^\dagger \right) \hat{V} \quad (\text{C.5})$$

$$\hat{L}_x^{\text{eff}} = \hat{L}_x \hat{H}_{\text{NH}}^{-1} \hat{V}, \quad (\text{C.6})$$

where

$$\hat{H}_{\text{NH}} = \hat{H}_e - \frac{i}{2} \sum_x \hat{L}_x^\dagger \hat{L}_x, \quad (\text{C.7})$$

is the no-jump Hamiltonian. The Hilbert space of the effective operators can be described in the basis of $\{|g\rangle, |f\rangle\}$ of the auxiliary atom and the states $\{|0\rangle, |1\rangle, |\tilde{o}\rangle\}$ of the qubit atoms. To ease the notation, we define the projection operators \hat{P}_n which projects on to the states with n qubits in state $|1\rangle$. From Eq. (C.5) and (C.6) we

then find:

$$\begin{aligned}\hat{H}_{\text{eff}} &= \sum_{n=0}^N \frac{-\Omega^2}{4\gamma} \text{Re} \left\{ \frac{i\tilde{\Delta}_e/2 + nC}{\tilde{\Delta}_e(i\tilde{\Delta}_E/2 + C_f) + \tilde{\Delta}_E nC} \right\} |g\rangle\langle g| \otimes \hat{P}_n \\ &= \sum_{n=0}^N \Delta_n |g\rangle\langle g| \otimes \hat{P}_n\end{aligned}\quad (\text{C.8})$$

$$\begin{aligned}\hat{L}_0^{\text{eff}} &= \sum_{n=0}^N \frac{1}{2\sqrt{\gamma}} \frac{\sqrt{C_f}\tilde{\Delta}_e\Omega}{\tilde{\Delta}_e(i\tilde{\Delta}_E/2 + C_f) + n\tilde{\Delta}_E C} |f\rangle\langle g| \otimes \hat{P}_n \\ &= \sum_{n=0}^N r_{0,n}^{\text{eff}} |f\rangle\langle g| \otimes \hat{P}_n\end{aligned}\quad (\text{C.9})$$

$$\begin{aligned}\hat{L}_g^{\text{eff}} &= \sum_{n=0}^N \frac{1}{2} \frac{(i\tilde{\Delta}_e/2 + nC)\Omega}{\tilde{\Delta}_e(i\tilde{\Delta}_E/2 + C_f) + n\tilde{\Delta}_E C} \frac{\sqrt{\gamma_g}}{\gamma} |g\rangle\langle g| \otimes \hat{P}_n \\ &= \sum_{n=0}^N r_{g,n}^{\text{eff}} |g\rangle\langle g| \otimes \hat{P}_n\end{aligned}\quad (\text{C.10})$$

$$\begin{aligned}\hat{L}_f^{\text{eff}} &= \sum_{n=0}^N \frac{1}{2} \frac{(i\tilde{\Delta}_e/2 + nC)\Omega}{\tilde{\Delta}_e(i\tilde{\Delta}_E/2 + C_f) + n\tilde{\Delta}_E C} \frac{\sqrt{\gamma_f}}{\gamma} |f\rangle\langle g| \otimes \hat{P}_n \\ &= \sum_{n=0}^N r_{f,n}^{\text{eff}} |f\rangle\langle g| \otimes \hat{P}_n\end{aligned}\quad (\text{C.11})$$

$$\begin{aligned}\hat{L}_k^{\text{eff}} &= \sum_{n=1}^N -\frac{1}{2\sqrt{\gamma}} \frac{\sqrt{C_f}\sqrt{C}\Omega}{\tilde{\Delta}_e(i\tilde{\Delta}_E/2 + C_f) + n\tilde{\Delta}_E C} |f\rangle\langle g| \otimes |\tilde{o}\rangle_k \langle 1| \otimes \hat{P}_n \\ &= \sum_{n=1}^N r_n^{\text{eff}} |f\rangle\langle g| \otimes |\tilde{o}\rangle_k \langle 1| \otimes \hat{P}_n,\end{aligned}\quad (\text{C.12})$$

where we have defined the cooperativities $C_{(f)} = g_{(f)}^2/\gamma\kappa$ for the qubit (auxiliary) atoms and the complex detunings $\tilde{\Delta}_E\gamma = \Delta_E - i\gamma_f/2$ and $\tilde{\Delta}_e\gamma = \Delta_e - i\gamma/2$. Note that we have defined the parameters $r_{0,n}^{\text{eff}}$, $r_{g,n}^{\text{eff}}$, $r_{f,n}^{\text{eff}}$ and r_n^{eff} in Eqs. (C.9)-(C.12) to characterize the decays described by the Lindblad operators. Note that $r_0^{\text{eff}} = 0$. In our calculations we parametrize the difference between the auxiliary atom and the qubit atoms by $C_f = \alpha C$ and $\gamma_f = \beta\gamma$ to easier treat the limit of $C \gg 1$ that we are interested in.

C.1.1 Success probability and fidelity

Eqs. (C.9)-(C.12) show that the effect of all Lindblad operators, except \hat{L}_g^{eff} , is that the state of the auxiliary atom is left in state $|f\rangle$. All these errors are thus detectable by measuring the state of the auxiliary atom at the end of the gate. For the heralded gates where we condition on measuring the auxiliary atom in state $|g\rangle$ at the end of the gates, these detectable decays therefore do not effect the fidelity of the gates but only the success probability. The rate Γ_n of the detectable decays for a state with n qubits in state $|1\rangle$ is $\Gamma_n = |r_{0,n}^{\text{eff}}|^2 + |r_{f,n}^{\text{eff}}|^2 + |r_n^{\text{eff}}|^2$ and assuming an initial qubit state described by density matrix ρ_{qubit} the success probability of the gates is

$$P_{\text{success}} = \sum_{n=0}^N \text{Tr} \left\{ e^{-\Gamma_n t_{\text{gate}}} \rho_{\text{qubit}} \hat{P}_n \right\}, \quad (\text{C.13})$$

where t_{gate} is the gate time and Tr denotes the trace.

Having removed the detrimental effect of the detectable errors by heralding on a measurement of the auxiliary atom the fidelity of the gates will be determined by more subtle, undetectable errors (see below). We define the fidelity, F of the gate as

$$F = \frac{1}{P_{\text{success}}} \langle \psi | \langle g | \tilde{\rho}_{\text{qubit}} | g \rangle | \psi \rangle, \quad (\text{C.14})$$

where we have assumed that the ideal qubit state after the gate is a pure state $|\psi\rangle$ and $\tilde{\rho}_{\text{qubit}}$ is the actual density matrix of the qubits and the auxiliary atom after the gate operation.

C.1.2 N -qubit Toffoli gate

As shown in the article, the effective Hamiltonian in Eq. (C.8) is sufficient to make a Toffoli gate by putting the qubit atoms on resonance ($\Delta_e = 0$). We will now

treat the worst case and average fidelities of the general Toffoli gate referred to in the article. The undetectable errors limiting the fidelities are the following.

- As described in the article the energy shifts of the coupled qubit states are all $\Delta_{n>0} \sim \Omega^2/(4\gamma\sqrt{C})$ in the limit $C \gg 1$. However, to higher order in C , we find corrections on the order $\mathcal{O}(\Omega^2/C^{3/2})$ to the energy shifts, which depend on the number of qubits that couple. The gate time of the Toffoli gate is $t_T \sim 4\pi\sqrt{C}\gamma/\Omega^2$ and consequently, the higher order corrections give uneven phase shifts on the order of $\mathcal{O}(C^{-1})$ for the coupled qubit states at the end of the gate. This leads to a phase error in the fidelity of $\mathcal{O}(C^{-2})$.
- The difference between the rates of detectable errors (Γ_n) for different qubit states changes the relative weight of the qubit states during the gate. This error will be $\mathcal{O}(C^{-1})$ as shown below.
- For $\gamma_g > 0$ the undetectable decay from $|E\rangle \rightarrow |g\rangle$ in the auxiliary atom will destroy the coherence between the qubit states. We find that this error will be $\sim \frac{\gamma_g}{\gamma\sqrt{C}}$. For now, we will assume that $\gamma_g = 0$ and thus ignore this error since we will show that we can suppress the branching fraction γ_g/γ arbitrary close to zero by having a two photon driving.

Assuming that $\gamma_g = 0$, the dominating source of error limiting the performance of the Toffoli gate is thus the difference between the rates of the detectable errors for the qubit states. We tune Δ_E such that $\Gamma_0 = \Gamma_1$ and the largest difference between the detectable errors is thus between the completely uncoupled state and the state with all qubit atoms in state $|1\rangle$. As a result, we can find an upper bound on the fidelity

of the N qubit Toffoli gate, considering an initial state $|0\rangle^{\otimes N} + |1\rangle^{\otimes N}$ in the limit $N \rightarrow \infty$ because this state experiences the largest difference between the number of coupled and uncoupled qubits. We find that the upper bound on the fidelity and the corresponding success probability is

$$F_{\text{up}} \sim 1 - \frac{\pi^2 \alpha}{16(\alpha + \beta)} \frac{1}{C} \quad (\text{C.15})$$

$$P_{\text{success,up}} \sim 1 - \frac{(\alpha + 2\beta)\pi}{2\sqrt{\alpha}\sqrt{\alpha + \beta}} \frac{1}{\sqrt{C}}. \quad (\text{C.16})$$

. In general, the fidelity of the gate will, however, be larger than what is suggested above. Considering a generic input state $(|0\rangle + |1\rangle)^{\otimes N}$ with the same parameters as above, we find

$$F_{\text{gen}} \sim 1 - k(N) \frac{\alpha\pi^2}{\alpha + \beta} \frac{1}{C} \quad (\text{C.17})$$

$$P_{\text{success,gen}} \sim 1 - \frac{(d(N)\alpha + 2\beta)\pi}{2\sqrt{\alpha}\sqrt{\alpha + \beta}} \frac{1}{\sqrt{C}}, \quad (\text{C.18})$$

where $k(N), d(N)$ are scaling factors which depend on the number of qubits N . We calculate $k(N)$ and $d(N)$ numerically for $N = 1 - 100$ using the perturbation theory and find that they both decrease with N (see Fig. C.2). The upper bounded and generic fidelities and corresponding success probabilities are shown in Fig. C.2 for different number of qubits, N . As N increases we obtain higher generic fidelity, whereas the success probability is almost independent of N .

C.1.3 CZ-gate

In the special case of only two qubits the Toffoli gate is referred to as a control-phase (CZ) gate. As shown in the article, we can, in this case, completely remove the

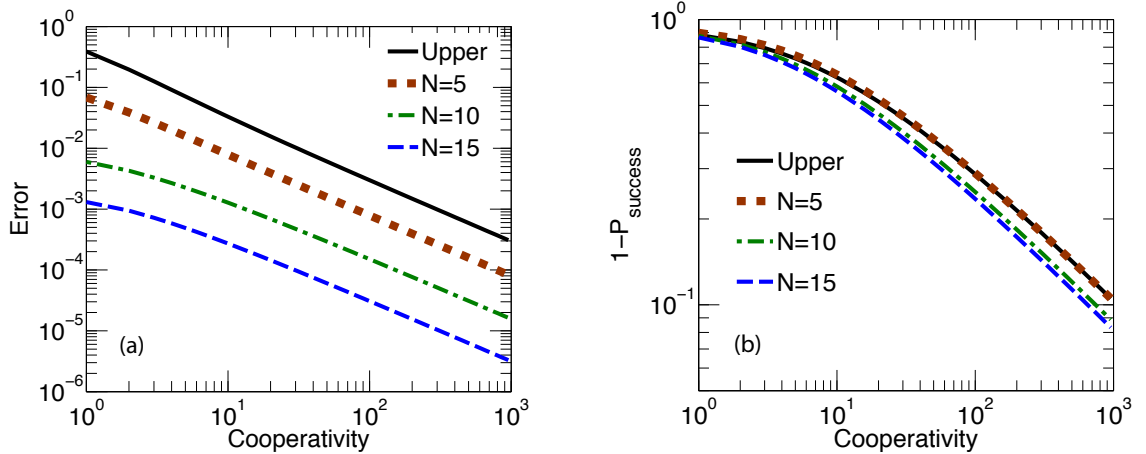


Figure C.2: (a) Gate error of the Toffoli for different initial states as a function of cooperativity. We have plotted the generic error for $N = 5, 10$, and 15 and the upper bound of the error. Note that the generic error decreases as N increases. We have fixed Δ such that $\Gamma_0 = \Gamma_1$ and have assumed that $\alpha = \beta = 1$. (b) The failure probabilities $1 - P_{\text{success,up}}$ and $1 - P_{\text{success,gen}}$ as a function of cooperativity. $1 - P_{\text{success,gen}}$ is plotted for $N = 5, 10, 15$. We have used the same assumptions as in (a). In general, the failure probability only have a weak dependence on N . Note that the line for $1 - P_{\text{success, gen}}, N = 5$ coincides with $1 - P_{\text{success,up}}$.

errors from the gate by choosing the detunings Δ_E and Δ_e such that $\Gamma_0 = \Gamma_1 = \Gamma_2$ and combining it with single qubit rotations we can ensure the right phase evolution. In the general case where $\alpha, \beta \neq 1$, the detunings Δ_e and Δ_E are

$$\Delta_E = \frac{\gamma}{2} \sqrt{\beta} \sqrt{4\alpha C + \beta} \quad (\text{C.19})$$

$$\Delta_e = \frac{\alpha C \gamma^2}{2\Delta_E}. \quad (\text{C.20})$$

The success probability of the gate is then

$$P_{\text{success}} \simeq 1 - \pi \frac{8\beta^2 + 6\beta\alpha + \alpha^2}{8\beta^{3/2}\sqrt{\alpha}} \frac{1}{\sqrt{C}}, \quad (\text{C.21})$$

and we find that the gate time is $t_{\text{CZ}} \simeq \frac{\gamma\pi\sqrt{\alpha}(\alpha+2\beta)(\alpha+4\beta)}{2\beta^{3/2}\Omega^2} \sqrt{C}$ in the limit $C \gg 1$.

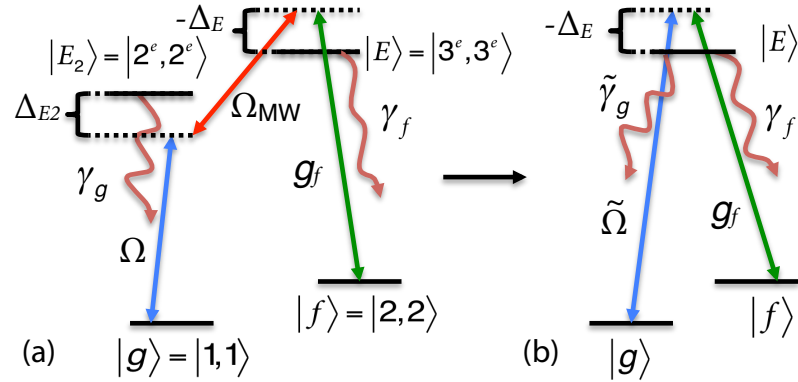


Figure C.3: (a) Level structure of the auxiliary atom and the transitions driven by a weak laser (Ω), a microwave field (Ω_{MW}) and the cavity (g_f). We assume that $|E\rangle \leftrightarrow |f\rangle$ is a closed transition and for simplicity we also assume that $|E_2\rangle \leftrightarrow |g\rangle$ is a closed transition but this is not a necessity. The figure also indicates how the levels could be realized in ^{87}Rb . Here $|r^{(e)}, r^{(e)}\rangle$ with $r = 1, 2, 3$ refers to state $|_{\text{F}}^{(e)} = r, {}_{\text{mF}}^{(e)} = r\rangle$ in ${}^2S_{1/2}$ (${}^2P_{3/2}$). (b) Effective three level atom realized by mapping the two-photon drive to an effective decay rate $\tilde{\gamma}_g$ and an effective drive $\tilde{\Omega}$

C.1.4 Two-photon driving

We now describe the details of the implementation where the auxiliary atoms is driven by a two-photon process as shown in Fig. C.3 (reproduced from Fig. 4(a) in the article) in order to suppress the dominant undetectable error caused by spontaneous decay of the auxilliary atom into the state $|g\rangle$ (\hat{L}_g).

The Hamiltonian in a proper rotating frame is

$$\hat{H} = \hat{H}_e + \hat{V} + \hat{V}^\dagger, \quad (\text{C.22})$$

$$\begin{aligned} \hat{H}_e &= \Delta_E |E\rangle\langle E| + \Delta_{E2} |E_2\rangle\langle E_2| + g_f (\hat{a}|E\rangle\langle f| + H.c.) \\ &\quad + \frac{\Omega_{\text{MW}}}{2} (|E\rangle\langle E_2| + H.c.) \\ &\quad + \sum_k \Delta_e |e\rangle_k\langle e| + g(\hat{a}|e\rangle_k\langle 1| + H.c.), \end{aligned} \quad (\text{C.23})$$

$$\hat{V} = \frac{\Omega}{2} |E_2\rangle\langle g|, \quad (\text{C.24})$$

where we have now defined $\Delta_E = \omega_E - \omega_g - \omega_{laser} - \omega_{\text{MW}}$, $\Delta_{E2} = \omega_{E2} - \omega_g - \omega_{laser}$ and $\Delta_e = \omega_e - \omega_g - \omega_{laser} - \omega_{\text{MW}} + \omega_f - \omega_1$. Here ω_{laser} is the frequency of the laser drive (Ω), ω_{MW} is the frequency of the microwave field (Ω_{MW}) and otherwise ω_x is the frequency associated with level x . We assume that the frequency of the cavity is $\omega_c = \omega_{laser} + \omega_{\text{MW}} + \omega_g - \omega_f$ such that the three photon Raman transition from $|g\rangle \rightarrow |f\rangle$ is resonant. We have assumed that Δ_{E2} is large and positive such that the rotating wave approximation is valid for the microwave field. The Lindblad operators describing the system are the same as described below Eq. (C.1) except that $\hat{L}_g \rightarrow \sqrt{\gamma_g}|g\rangle\langle E_2|$. Assuming a weak drive Ω , we can follow the same recipe as before to find the following effective operators describing the dynamics of the system.

$$\hat{H}_{\text{eff}}^{(2)} = \sum_{n=0}^N \Delta_n^{(2)} |g\rangle\langle g| \otimes \hat{P}_n \quad (\text{C.25})$$

$$\Delta_n^{(2)} = \frac{-\Omega^2}{4\gamma} \text{Re} \left[\frac{\tilde{\Delta}_e(i\tilde{\Delta}_E/2 + C_f) + n\tilde{\Delta}_E C}{\tilde{\Delta}_{E2}\tilde{\Delta}_e(i\tilde{\Delta}_E/2 + C_f) + n\tilde{\Delta}_E\tilde{\Delta}_{E2}C - i\tilde{\Delta}_e\tilde{\Omega}_{\text{MW}}^2/8 - n\tilde{\Omega}_{\text{MW}}^2C/4} \right]$$

$$\hat{L}_0^{\text{eff}(2)} = \sum_{n=0}^N r_{0,n}^{\text{eff}(2)} |f\rangle\langle g| \otimes \hat{P}_n \quad (\text{C.26})$$

$$r_{0,n}^{\text{eff}(2)} = \frac{-1}{4\sqrt{\gamma}} \frac{\sqrt{C_f}\tilde{\Delta}_e\Omega\tilde{\Omega}_{\text{MW}}}{\tilde{\Delta}_{E2}\tilde{\Delta}_e(i\tilde{\Delta}_E/2 + C_f) + n\tilde{\Delta}_{E2}\tilde{\Delta}_E C - i\tilde{\Delta}_e\tilde{\Omega}_{\text{MW}}^2/8 - n\tilde{\Omega}_{\text{MW}}^2C/4}$$

$$\hat{L}_g^{\text{eff}(2)} = \sum_{n=0}^N r_{g,n}^{\text{eff}(2)} |g\rangle\langle g| \otimes \hat{P}_n \quad (\text{C.27})$$

$$r_{g,n}^{\text{eff}(2)} = \frac{\Omega}{2} \frac{\tilde{\Delta}_e(i\tilde{\Delta}_E/2 + C_f) + n\tilde{\Delta}_E C}{\tilde{\Delta}_{E2}\tilde{\Delta}_e(i\tilde{\Delta}_E/2 + C_f) + n\tilde{\Delta}_{E2}\tilde{\Delta}_E C - i\tilde{\Delta}_e\tilde{\Omega}_{\text{MW}}^2/8 - n\tilde{\Omega}_{\text{MW}}^2C/4} \frac{\sqrt{\gamma_g}}{\gamma}$$

$$\hat{L}_f^{\text{eff}(2)} = \sum_{n=0}^N r_{f,n}^{\text{eff}(2)} |f\rangle\langle g| \otimes \hat{P}_n \quad (\text{C.28})$$

$$r_{f,n}^{\text{eff}(2)} = -\frac{\Omega}{4} \frac{(i\tilde{\Delta}_e/2 + nC)\tilde{\Omega}_{\text{MW}}}{\tilde{\Delta}_{E2}\tilde{\Delta}_e(i\tilde{\Delta}_E/2 + C_f) + n\tilde{\Delta}_{E2}\tilde{\Delta}_E C - i\tilde{\Delta}_e\tilde{\Omega}_{\text{MW}}^2/8 - n\tilde{\Omega}_{\text{MW}}^2C/4} \frac{\sqrt{\gamma_f}}{\gamma}$$

$$\hat{L}_k^{\text{eff}(2)} = \sum_{n=0}^{N-1} r_n^{\text{eff}(2)} |f\rangle\langle g| \otimes |\tilde{o}\rangle_k\langle 1| \otimes \hat{P}_n, \quad (\text{C.29})$$

$$r_n^{\text{eff}(2)} = \frac{1}{4\sqrt{\gamma}} \frac{\sqrt{C_f}\sqrt{C}\tilde{\Omega}_{\text{MW}}\Omega}{\tilde{\Delta}_{E2}\tilde{\Delta}_e(i\tilde{\Delta}_E/2 + C_f) + n\tilde{\Delta}_{E2}\tilde{\Delta}_EC - i\tilde{\Delta}_e\tilde{\Omega}_{\text{MW}}^2/8 - n\tilde{\Omega}_{\text{MW}}^2C/4}$$

where we have defined the complex detuning $\tilde{\Delta}_{E2}\gamma = \Delta_{E2} - i\gamma_g/2$ and the parameters $r_{0,n}^{\text{eff}(2)}$, $r_{g,n}^{\text{eff}(2)}$, $r_{f,n}^{\text{eff}(2)}$ and $r_n^{\text{eff}(2)}$ to characterize the decay described by the Lindblad operators.

We are interested in the limit of large detuning Δ_{E2} and large cooperativity C . In this limit, we find that the dynamics of the system can be mapped to a simple three level atom with effective driving $\tilde{\Omega} \sim \Omega\Omega_{\text{MW}}/(2\Delta_{E2})$ and an effective decay $\tilde{\gamma}_g \sim \gamma_g\Omega_{\text{MW}}^2/\Delta_{E2}^2$ as shown in Fig. C.3. In principle, the effective operator $\hat{L}_0^{\text{eff}(2)}$ leads to an effective decay rate of $\tilde{\gamma} = \gamma_g\Omega^2/\Delta_{E2}^2$ to lowest order in C but we find that this first order term do not destroy the coherence between the qubit states since it is independent of n . There is, therefore, no effect of these scattering events and the performance of the gate behaves as if there is an effective decay rate of $\tilde{\gamma}_g \sim \gamma_g\Omega_{\text{MW}}^2/\Delta_{E2}^2$. Note that we also have an AC stark shift imposed on the level $|g\rangle$ by the laser characterized by Ω . This will give an overall phase to the system, $\sim \Omega^2/(4\Delta_{E2})t$, which we can neglect since it does not influence the gates. Since we can do the mapping to the simple three level atom, we find similar results for the performance of the gates for the two-photon scheme as for the simple three level scheme only with effective decay $\tilde{\gamma}_g$ and drive $\tilde{\Omega}$ given by the two-photon process. Note, however, that we now assume $\gamma_g > 0$, which introduces an undetectable error as previously mentioned. We find that this introduces an error in the fidelity of both

gates of roughly

$$\sim \frac{(\alpha^2 - 4\alpha\beta - 6\beta^2)\pi^2}{128\beta^2} \frac{\gamma_g^4}{\gamma^4 \Delta_{E2}^4} + \frac{(\alpha^2 + 4\alpha\beta + 6\beta^2)\pi}{16\sqrt{\alpha\beta}(\alpha + 2\beta)(\alpha + 5\beta)} \frac{\gamma_g \Omega_{MW}^2}{\gamma \Delta_{E2}^2} \frac{1}{\sqrt{C}} \quad (\text{C.30})$$

Nonetheless, this error can be suppressed arbitrarily much by increasing Δ_{E2} , which enable us to have a heralded CZ-gate with arbitrarily small error in a realistic atomic setup using the two-photon drive.

C.2 Gate time

Here we address the question of how strongly we can drive the system and still maintain the validity of perturbation theory. We need to address this question since the gate time depends inversely on the driving strength as shown in the article and hence this limits the achievable gate time. A necessary criterion for our perturbation theory to be valid is that the energy shifts Δ_n (see Eq. (C.8) and Eq. (C.25)) are small compared to the driving, i.e. $\sim \Delta_n^2/\Omega^2 \ll 1$. From Eq. (C.8) we find that $\Delta_n^2/\Omega^2 \sim \Omega^2/(16\Delta_E^2)$ to leading order in the cooperativity C and this criterion is therefore met for $\Omega \ll 4\Delta_E$. Similarly, for the two-photon process, we find from Eq. (C.25) that $(\Delta_n^{(2)})^2/\Omega^2 \sim \Omega^2/(16\Delta_{E2}^2)$, to leading order in C . Here we thus need $\Omega \ll 4\Delta_{E2}$.

Another criterion needs to be met in order for our perturbative theory to be valid. If none of the qubits couple, we are effectively driving the auxiliary atom/cavity system into a dark state of the form $\cos(\theta)|0, g\rangle - \sin(\theta)|1, f\rangle$, where the mixing angle is $\theta \sim \Omega/g$. Here the number refers to the number of cavity photons. To adiabatically eliminate the state $|f, 1\rangle$ from the Hamiltonian as we have done in the

effective Hamiltonian requires that $\Omega/g \ll 1$. Mapping this criterion to the effective three level scheme realized in the two-photon scheme gives $\Omega\Omega_{\text{MW}}/(2\Delta_{E2}g) \ll 1$.

Finally, we need to consider the scattering of photons from the level $|E2\rangle$ in the two-photon scheme. If the number of scattering events, n_{scat} is large compared to $\Omega^2/(16\Delta_{E2}^2)$, the perturbation theory is not valid even though the other criterions are met. We find that $n_{scat} \sim \frac{12\sqrt{C}\gamma^2}{\Omega_{\text{MW}}^2}$ for the CZ-gate and we thus need to have $\frac{3\sqrt{C}\gamma^2\Omega^2}{\Delta_{E2}^2\Omega_{\text{MW}}^2} \ll 1$

The different criterions for the validity of the perturbation theory are summarized in Tab. C.2.

Simple scheme	Two-photon scheme
$\Omega/(4\Delta_E) \ll 1$	$\Omega/(4\Delta_{E2}) \ll 1$
$\Omega/g \ll 1$	$\Omega\Omega_{\text{MW}}/(\Delta_{E2}g) \ll 1$
-	$3\sqrt{C}\gamma^2\Omega^2/(\Delta_{E2}^2\Omega_{\text{MW}}^2) \ll 1$

Table C.2: The criterions for our perturbation theory to be valid.

For all the gate schemes, we have assumed that $\Delta_E \propto \sqrt{C}\gamma$. The first criterion for the simple scheme (see Tab. C.2) can thus be met with a driving of $\Omega = a\gamma\sqrt{C}$ where $a/4 \ll 1$. This driving results in a gate time that decreases as $1/\sqrt{C}$. The value of a will determine the size of the non-adiabatic error. The second criterion is also fulfilled for this driving as long as $\sqrt{\gamma/\kappa} \ll 1$. In realistic systems such as the nanocavity system described in Ref. [94, 96], the ratio κ/γ can be on the order of 100-1000. For the two-photon scheme, we find from Tab. C.2 that we can choose $\Omega = a_2\Delta_{E2}, \Omega_{\text{MW}} = b\gamma C^{1/4}$ where the constants a_2, b will determine the size of the

non-adiabatic errors as before. Similar to the situation in the simple scheme we assume that $\sqrt{\gamma/\kappa} \ll 1$.

C.3 Numerical simulation

In order to confirm our results, we numerically integrated the full Master equation, defined by the Hamiltonian \hat{H} and the Lindblad operators, $\hat{L}_j \in \{\hat{L}_0, \hat{L}_g, \hat{L}_f, \hat{L}_1, \hat{L}_2\}$,

$$\frac{d}{dt}\rho(t) = -\frac{i}{\hbar}[\hat{H}, \rho(t)] + \sum_j \frac{1}{2} \left[2\hat{L}_j\rho(t)\hat{L}_j^\dagger - \rho(t)\hat{L}_j^\dagger\hat{L}_j - \hat{L}_j^\dagger\hat{L}_j\rho(t) \right] \quad (\text{C.31})$$

We used the QuTiP 2 package [41], for Python, to set up the problem and used its 12th-order numerical integration algorithm to find the solution $\rho(t)$ as a time series. Then, we used the routines of the same package to analyze the results.

For each time series $\rho(t)$, we determined the gate time t_{gate} , the success probability P_{success} , and the fidelity F . We picked $|\psi_0\rangle_{12} = \frac{1}{\sqrt{2}}(|0\rangle + |1\rangle)_1 \otimes \frac{1}{\sqrt{2}}(|0\rangle + |1\rangle)_2$ as the initial state of the two qubits, $|g\rangle$ for the control atom, and zero photons in the cavity. Starting from here, we let the system evolve under the Master equation Eq. (C.31), and determined $P_g(t)$, the conditional state $\rho_g(t)$ and $F(t)$ as a function of time:

$$P_g(t) = \text{Tr}[\rho(t)|g\rangle\langle g|], \quad (\text{C.32})$$

$$\rho_g(t) = \frac{|g\rangle\langle g|\rho(t)|g\rangle\langle g|}{P_g(t)}, \quad (\text{C.33})$$

$$F(t) = \max_{\phi_1, \phi_2} \left\langle \psi_t^{\phi_1, \phi_2} \middle| \text{Tr}_{c, c}(\rho_g(t)) \middle| \psi_t^{\phi_1, \phi_2} \right\rangle \quad (\text{C.34})$$

where $\text{Tr}_{c, c}$ is the partial trace operation over the control atom and the cavity, and $|\psi_t^{\phi_1, \phi_2}\rangle$ is the target state transformed with two single qubit z -rotations:

$$|\psi_t^{\phi_1, \phi_2}\rangle = \hat{U}_1(\phi_1)\hat{U}_2(\phi_2)\frac{1}{2}(|00\rangle + |01\rangle + |10\rangle - |11\rangle), \quad (\text{C.35})$$

where $\hat{U}_k(\phi_k) = \exp [i|1\rangle_k\langle 1|_k\phi_k]$ is the z -rotation of qubit k ($= 1, 2$) by the angle ϕ_k . From these time series, we determined the gate time t_{gate} by finding the timepoint where $F(t)$ is maximal,

$$t_{\text{gate}} = \underset{t}{\operatorname{argmax}} F(t) \quad (\text{C.36})$$

The fidelity and the success probability of the gate is then defined as $F = F(t_{\text{gate}})$, $P_{\text{success}} = P_g(t_{\text{gate}})$.

Plots of Fig. C.4 show the gate time (t_{gate}) and the success probability (P_{success}) as a function of a , for $\gamma_g = 0$, $\gamma = 0.01\kappa$, $\Omega = a\gamma\sqrt{C}$ with $C \in \{10, 30, 100, 300, 1000\}$. The detunings, Δ_E and Δ_e were chosen to be close to their optimal value, determined from the adiabatic theory, and numerically optimized to result in identical effective $|g\rangle \rightarrow |f\rangle$ transition rates $\Gamma_0 = \Gamma_1 = \Gamma_2$ for the qubit sectors $|00\rangle, |01\rangle, |11\rangle$. The rates Γ_j were found by numerically diagonalizing the master equation for the qubit sectors separately, and finding the eigenvalue with the smallest (but non-zero) absolute real part. This numerical optimization yielded the maximal fidelity. The symbols correspond to the numerical result, whereas the solid lines show the theoretical values. The agreement of the results confirms the validity of the adiabatic theory for a driving $\Omega = a\gamma\sqrt{C}$ for $C \lesssim 1000$ and $a \lesssim 0.25$. Note, however, that Fig. C.4 shows how the success probability deviates from the adiabatic result for $a \gtrsim 0.25$. A weak increase of this deviation with the cooperativity is seen but from simulations at high C , we believe that this can be removed by gradually ramping Ω up and down to maintain adiabaticity at the beginning and end of the driving pulse. This was not included in the simulations behind Fig. C.4 for simplicity.

Fig. C.5 shows the conditional *infidelity* of the gate as a function of a for the same

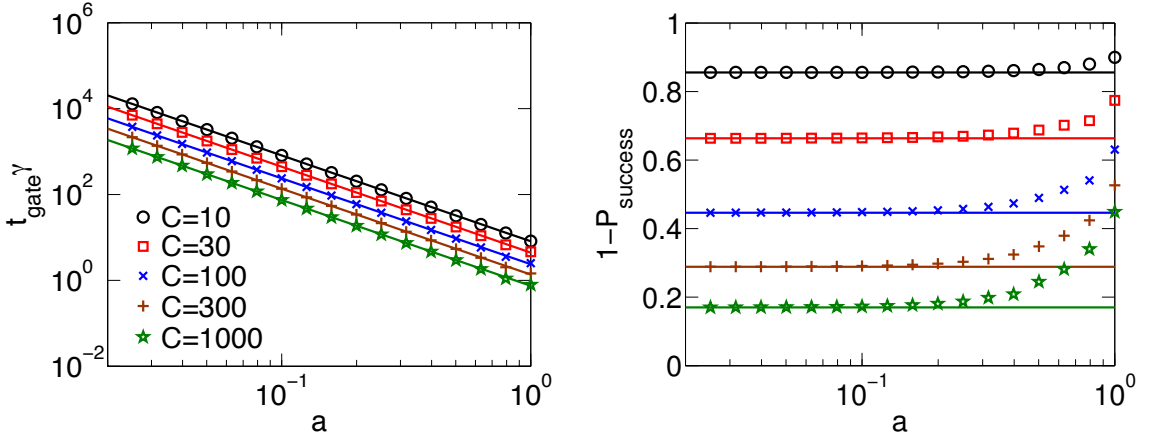


Figure C.4: Gate time (left) and failure probability (right) as a function of driving strength (a) for $\gamma/\kappa = 0.01$, $\gamma_g = 0$, and $C \in \{10, 30, 100, 300, 1000\}$. The driving strength was assumed to be $\Omega = a\gamma\sqrt{C}$.

parameters. The simulation confirms that using $a = 0.25$ is enough to push the (conditional) infidelity of the gate below $4 \cdot 10^{-5}$. The fidelity is limited by non-adiabatic effects, which can be suppressed by decreasing Ω as shown in the figure. Adiabatically ramping up and down at the beginning and end of the gate will also improve the adiabaticity but, for simplicity, we have not included this in the simulations described here. Note, however that for high C ($C > 1000$), we find that this gradual ramping of Ω significantly decreases the non-adiabatic error.

We repeated the above analysis for the two-photon-driving Hamiltonian in Eq. (C.22). We chose $\gamma = \gamma_g = \gamma_f = 0.01 \kappa$, $\Omega = \frac{\Delta_{E2}}{8C^{1/4}}$, and $\Omega_{\text{MW}} = 4\gamma C^{1/4}$, and chose Δ_E and Δ_e detunings again close to their adiabatic optimum, but numerically optimized them with the same procedure as previously. Plots of Fig.C.6 show the gate time and the success probability as a function of Δ_{E2} for $C \in \{10, 20, 50, 100\}$. Symbols indicate the numerical results while solid lines show the theoretical values. Fig. 2b in the article shows the conditional *infidelity* of the two-photon-driven gate as a function of C

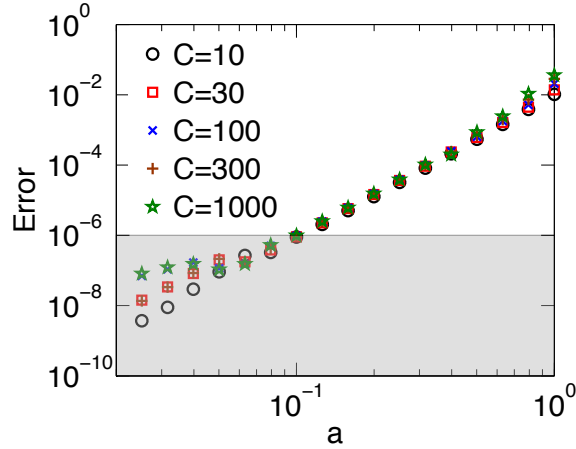


Figure C.5: Conditional infidelity of the gate as a function of the driving strength (a) for $\gamma/\kappa = 0.01$, $\gamma_g = 0$, and $C \in \{10, 30, 100, 300, 1000\}$. The shaded region (at $\sim 10^{-6}$) shows the limit of numerical accuracy. The driving strength was assumed to be $\Omega = a\gamma\sqrt{C}$.

for the same choice of parameters. With these results, we confirm that by increasing Δ_{E2} we can lower the infidelity error to an arbitrary small level. The gate time is a constant of the cooperativity since we have increased Ω_{MW} as $C^{1/4}$ in the simulations. We do see some deviation from the analytical results due to non-adiabatic effects, which could be suppressed by decreasing Ω at the expense of an increase in the gate time. Finally a gradual ramping of Ω could also decrease the non-adiabatic errors but for simplicity, we have not included this in the simulations.

C.4 Additional errors

There are some additional errors in a realistic atomic setup that we have not treated in detail so far. Here we estimate the dominant errors and determine under which conditions, they can be sufficiently suppressed such that they do not limit the performance of the gates. We assume a realistic atomic setup where ^{87}Rb atoms are

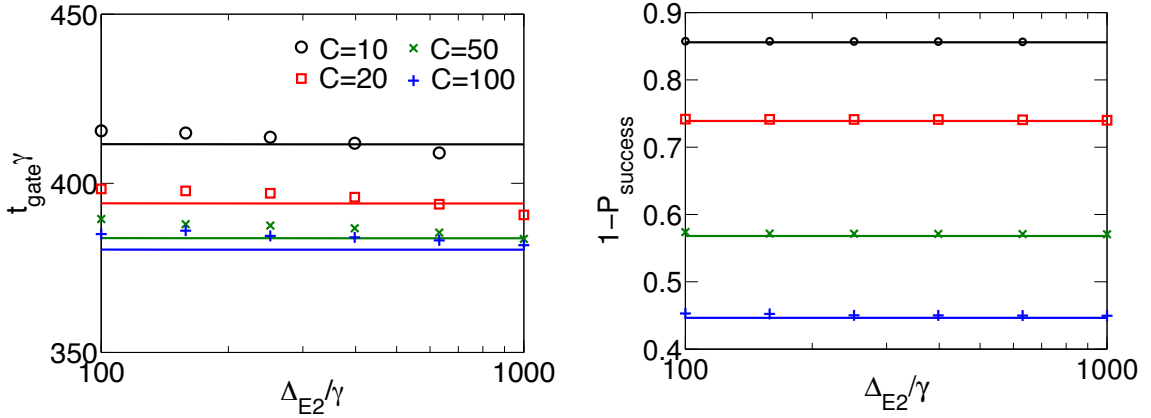


Figure C.6: Gate time (left) and failure probability (right) as a function of Δ_{E2} for $\gamma = \gamma_g = \gamma_f = 0.01\kappa$, $\Omega = \frac{\Delta_{E2}}{8C^{1/4}}$, $\Omega_{\text{MW}} = 4\gamma C^{1/4}$, $C = \{10, 20, 50, 100\}$.

used both for the auxiliary atom and the qubit atoms. In the ^{87}Rb atoms, we assume that $|g\rangle = |1, 1\rangle$, $|f\rangle = |2, 2\rangle$ and $|E_2\rangle = |2^e, 2^e\rangle$, $|E\rangle = |3^e, 3^e\rangle$ where $|r^{(e)}, r^{(e)}\rangle$ with $r = 1, 2, 3$ refers to state $|_{\text{F}}^{(e)} = r, {}_{\text{mF}}^{(e)} = r\rangle$ in $5^2S_{1/2}$ ($5^2P_{3/2}$). In this case, we estimate that the dominant errors are:

- In our perturbative theory, we have assumed that the laser field (Ω) only couple $|g\rangle \rightarrow |E_2\rangle$ in the auxiliary atom. However, for a large detuning Δ_{E2} it may also couple $|f\rangle \rightarrow |E\rangle$, which could lead to an undetectable error where the auxiliary atom is pumped back to $|E_2\rangle$ from, which it decays to $|g\rangle$. This error is, however, suppressed by the large frequency separation, Δ_g of $|g\rangle$ and $|f\rangle$, which is $\Delta_g \sim 1000\gamma$ for ^{87}Rb . We estimate the error using effective operators to find the decay rate back to $|g\rangle$, assuming that the auxiliary atom starts in $|E_2\rangle$ and treating the drive Ω as a perturbation while neglecting the cavity coupling. This is valid as long as $\Delta_g \gg \Delta_E$, which is fulfilled for $C \lesssim 10000$ since $\Delta_E \sim \sqrt{C}$. The error increases with Δ_{E2} but even for $\Delta_{E2} \approx 400\gamma$ we find that for $\Omega_{\text{MW}} = 4\gamma C^{1/4}$, $\Omega = \Delta_{E2}/8$ the error is $\lesssim 10^{-4}$.

- The microwave might also couple the ground states $|0\rangle - |1\rangle$ of the qubit atoms and the ground states $|g\rangle - |f\rangle$ of the auxiliary atom. The coupling of $|0\rangle - |1\rangle$ means that the qubit atoms also couple to the cavity even though they are in state $|0\rangle$. We estimate the error from this to be on the order of $\Omega_{\text{MW}}^2 / (\Delta_g - (\Delta_{E2} - \Delta_E + \Delta_{2 \rightarrow 3}))^2$ where $\Delta_{2 \rightarrow 3}$ is the splitting between $|E_2\rangle$ and $|E\rangle$. For ^{87}Rb , $\Delta_{2 \rightarrow 3} \approx 44\gamma$. Below we argue that we need $\Delta_E < 0$. Since $\Delta_E \approx -\sqrt{C}\gamma$ this error will increase slowly with cooperativity but it is suppressed by Δ_g . For $\Omega_{\text{MW}} = 4\gamma C^{1/4}$, we find that the error is $\lesssim 10^{-4}$ for $C \lesssim 1000$ even for $\Delta_{E2} \approx 400\gamma$. The errors from the coupling of the states $|g\rangle - |f\rangle$ in the auxiliary atom will likewise be suppressed by the large energy splitting Δ_g . These errors can also be further suppressed by decreasing Ω_{MW} at the cost of a larger gate time.

The above errors can be highly suppressed using e.g. ^{88}Sr , $^{138}\text{Ba}^+$ or $^{40}\text{Ca}^+$ instead of ^{87}Rb . For these atoms, the ground states can be encoded in the S_0 and P_0 manifolds for ^{88}Sr and the $S_{1/2}$ and $D_{3/2}$ manifolds for $^{138}\text{Ba}^+$ and $^{40}\text{Ca}^+$, which have separations at optical frequencies between the stable states.

A final error that we will consider is that the transition $|E\rangle \leftrightarrow |f\rangle$ will not be completely closed if the cavity is linearly polarized. This will, e.g. be the case for the system in Ref. [94]. Such a cavity also couples $|f\rangle$ to the states $|1^e, 1^e\rangle$, $|2^e, 1^e\rangle$ and $|3^e, 1^e\rangle$. From $|1^e, 1^e\rangle$ and $|2^e, 1^e\rangle$ there might be an undetectable decay back to $|g\rangle$, which will introduce an error $\propto 1/\sqrt{C}$ in the gates. The probability of an undetectable decay from these states should be compared to the probability of the detectable decays where the cavity photon is scattered off the qubit atoms instead.

For ^{87}Rb , we estimate this error by comparing the strengths of the effective couplings from $|f\rangle$ to $|1^e, 1^e\rangle$ and $|2^e, 1^e\rangle$ with a subsequent decay to $|g\rangle$ with the strength of the effective coupling from $|1\rangle$ to $|e\rangle$ in the qubit atoms with a subsequent decay back to $|1\rangle$. The latter process has a detuning of Δ_E while the first two are additional detuned by the energy gaps between $|3^e, 3^e\rangle$ and $|1^e, 1^e\rangle$ and $|3^e, 3^e\rangle$ and $|2^e, 1^e\rangle$ respectively, assuming that $\Delta_E < 0$. We find that since $|\Delta_E|$ grows as \sqrt{C} the error increases from $\sim 5 \cdot 10^{-5}$ at $C = 1$ to a maximum value of $\sim 2 \cdot 10^{-3}$ for $C \sim 3000$ for which Δ_E is comparable to the extra detunings of the $|1^e, 1^e\rangle$ and $|2^e, 1^e\rangle$ transitions compared to the $|e\rangle$ transition. For $C > 3000$ the error decreases as $1/\sqrt{C}$. Note that this error could be removed by making a 4 photon drive from $|g\rangle$ to $|E\rangle$ by letting $|g\rangle = |1, -1\rangle$. Another approach is to consider other atoms such as $^{40}\text{Ca}^+$, with more favorable levelstructures. The state $|g\rangle$ could be encoded in the $3^2D_{5/2}$ subspace while the state $|f\rangle$ could be encoded in the $4^2S_{1/2}$ subspace and similarly for the qubit states $|0\rangle$ and $|1\rangle$. In such a setup, we will have separations of optical frequencies between the qubit states and we can remove the decay from the excited state back to $|g\rangle$ by, e.g. driving from $3^2D_{5/2}$ to $4^2P_{1/2}$ through $3^2D_{3/2}$.

Appendix D

Appendices for Chapter 5

D.1 Error analysis of the single-photon scheme

The setup of the single-photon scheme is described in Sec. 5.3.1. The single photon detectors are assumed to have a dark count probability of P_{dark} and an efficiency of η_d while the transmission efficiency of the fibers is denoted η_f . As described in Sec. 5.2, the probability of an emitter to go from the excited state, $|e\rangle$ to the ground state $|1\rangle$ is P_{phot} while the excitation probability is ϵ^2 . The scheme is conditioned on a single click at the central station. Depending on which detector gave the click, a single qubit rotation can be employed such that ideally the state $|\Psi^+\rangle$ is created. Going through all the possibilities of obtaining a single click at the central station, we find that the density matrix following a single click, and possible subsequent single qubit rotations, is

$$\begin{aligned} \rho_{1click} = & F_1 |\Psi^+\rangle\langle\Psi^+| + \alpha_1 |\Phi^+\rangle\langle\Phi^+| + \alpha_1 |\Phi^-\rangle\langle\Phi^-| \\ & + \beta_1 |\Psi^-\rangle\langle\Psi^-| + \tilde{\alpha}_1 |00\rangle\langle 00| + \tilde{\beta}_1 |11\rangle\langle 11|, \end{aligned} \quad (\text{D.1})$$

with coefficients

$$\begin{aligned} F_1 = & \frac{1}{P_{\text{1click}}} \left[2\eta_d\eta_f P_p \epsilon^2 (1 - \epsilon^2) (1 - P_d) + 2\eta_f(1 - \eta_d) P_p \epsilon^2 (1 - \epsilon^2) P_d (1 - P_d) \right. \\ & + \frac{1}{2} \eta_d \eta_f P_p \epsilon^4 (1 - P_p) (1 - P_d) + 2(1 - \eta_f) P_p \epsilon^2 (1 - \epsilon^2) P_d (1 - P_d) \\ & \left. + (1 - \eta_d \eta_f) P_p \epsilon^4 (1 - P_p) P_d (1 - P_d) + (1 - \epsilon^2) \epsilon^2 (1 - P_p) P_d (1 - P_d) \right. \\ & \left. + \frac{1}{2} \epsilon^2 (1 - P_p)^2 P_d (1 - P_d) \right] \end{aligned} \quad (\text{D.2})$$

$$\alpha_1 = \frac{1}{P_{\text{1click}}} \left[\frac{1}{2} \epsilon^2 (1 - P_p)^2 P_d (1 - P_d) \right] \quad (\text{D.3})$$

$$\begin{aligned} \beta_1 = & \frac{1}{P_{\text{1click}}} \left[\frac{1}{2} \eta_d \eta_f P_p \epsilon^4 (1 - P_p) (1 - P_d) + 2(1 - \eta_f) P_p \epsilon^2 (1 - \epsilon^2) P_d (1 - P_d) \right. \\ & \left. + (1 - \eta_d \eta_f) P_p \epsilon^4 (1 - P_p) P_d (1 - P_d) + (1 - \epsilon^2) \epsilon^2 (1 - P_p) P_d (1 - P_d) \right. \\ & \left. + \frac{1}{2} \epsilon^2 (1 - P_p)^2 P_d (1 - P_d) + 2\eta_f(1 - \eta_d) P_p \epsilon^2 (1 - \epsilon^2) P_d (1 - P_d) \right] \end{aligned} \quad (\text{D.4})$$

$$\tilde{\alpha}_1 = \frac{1}{P_{\text{1click}}} \left[2(1 - \epsilon^2)^2 P_d (1 - P_d) + 2(1 - \epsilon^2) \epsilon^2 (1 - P_p) P_d (1 - P_d) \right] \quad (\text{D.5})$$

$$\begin{aligned} \tilde{\beta}_1 = & \frac{1}{P_{\text{1click}}} \left[\eta_d \eta_f P_p \epsilon^4 (1 - P_p) (1 - P_d) + 2(1 - \eta_d \eta_f) P_p \epsilon^4 (1 - P_p) P_d (1 - P_d) \right. \\ & \left. + 2(1 - \eta_d \eta_f)^2 P_p^2 \epsilon^4 P_d (1 - P_d) + 2(1 - \eta_d \eta_f) \eta_d \eta_f P_p^2 \epsilon^4 (1 - P_d)^2 \right], \end{aligned} \quad (\text{D.6})$$

where $P_d = P_{\text{dark}}$ and $P_p = P_{\text{phot}}$. Here we have assumed that with probability $\epsilon^2(1 - P_{\text{phot}})$, an emitter is excited but spontaneously decay to the ground states instead of emitting a cavity photon. Furthermore, we have assumed that the decay rates to the two ground states are equal such that the emitter ends up in $\frac{1}{2}(|0\rangle\langle 0| + |1\rangle\langle 1|)$. Note that the detectors are not assumed to be number resolving. P_{1click} is the total success probability given by

$$\begin{aligned} P_{\text{1click}} = & 2\eta_d\eta_f P_{\text{phot}} \epsilon^2 (1 - P_{\text{phot}} \epsilon^2) (1 - P_{\text{dark}}) + (2\eta_f\eta_d - \eta_f^2\eta_d^2) P_{\text{phot}}^2 \epsilon^4 \\ & + 2(1 - \epsilon^2 P_{\text{phot}})^2 P_{\text{dark}} (1 - P_{\text{dark}}) + 2(1 - \eta_d \eta_f)^2 P_{\text{phot}}^2 \epsilon^4 P_{\text{dark}} (1 - P_{\text{dark}}) \\ & + 4(1 - \eta_d \eta_f) P_{\text{phot}} \epsilon^2 (1 - \epsilon^2 P_{\text{phot}}) P_{\text{dark}} (1 - P_{\text{dark}}). \end{aligned} \quad (\text{D.7})$$

Assuming $P_{\text{dark}} \ll 1$, the dominant error is where both qubits are excited but only a single click is detected at the central station. This leaves the qubits in the state $|11\rangle\langle 11|$ and this error is efficiently detected by the purification scheme described in Ref. [?].

D.2 Error analysis of the two-photon scheme

For the two photon scheme described in Sec. 5.2, we condition on a click in two detectors. Once again we assume that appropriate single qubit rotations are employed depending on which detector combination clicked such that ideally the state $|\Phi^+\rangle$ is created. We find that the density matrix describing the qubit state after a successful event is

$$\rho_{2\text{click}} = F_2|\Phi^+\rangle\langle\Phi^+| + \alpha_2|\Psi^+\rangle\langle\Psi^+| + \alpha_2|\Psi^-\rangle\langle\Psi^-| + \beta_2|\Phi^-\rangle\langle\Phi^-|, \quad (\text{D.8})$$

where we have defined

$$\begin{aligned} F_2 &= \frac{(1 - P_{\text{dark}})^2}{P_{\text{2click}}} \left[\frac{1}{2} \eta_d^2 \eta_f^2 P_{\text{phot}}^2 + \eta_d (1 - \eta_d) \eta_f^2 P_{\text{dark}} P_{\text{phot}}^2 + \eta_f^2 (1 - \eta_d)^2 P_{\text{phot}}^2 P_{\text{dark}}^2 \right. \\ &\quad + P_{\text{dark}}^2 (1 - P_{\text{phot}})^2 + \eta_d (1 - \eta_f) \eta_f P_{\text{dark}} P_{\text{phot}}^2 + \eta_d \eta_f P_{\text{dark}} P_{\text{phot}} (1 - P_{\text{phot}}) \\ &\quad \left. + (1 - \eta_f)^2 P_{\text{phot}}^2 P_{\text{dark}}^2 + 2\eta_f (1 - \eta_d) (1 - \eta_f) P_{\text{phot}}^2 P_{\text{dark}}^2 \right. \\ &\quad \left. + 2(1 - \eta_d \eta_f) P_{\text{phot}} (1 - P_{\text{phot}}) P_{\text{dark}}^2 \right] \end{aligned} \quad (\text{D.9})$$

$$\begin{aligned} \alpha_2 &= \frac{(1 - P_{\text{dark}})^2}{P_{\text{2click}}} \left[\eta_d (1 - \eta_f) \eta_f P_{\text{dark}} P_{\text{phot}}^2 + P_{\text{dark}}^2 (1 - P_{\text{phot}})^2 + \right. \\ &\quad \eta_d \eta_f P_{\text{dark}} P_{\text{phot}} (1 - P_{\text{phot}}) + (1 - \eta_f)^2 P_{\text{phot}}^2 P_{\text{dark}}^2 \\ &\quad + 2\eta_f (1 - \eta_d) (1 - \eta_f) P_{\text{phot}}^2 P_{\text{dark}}^2 + 2(1 - \eta_d \eta_f) P_{\text{phot}} (1 - P_{\text{phot}}) P_{\text{dark}}^2 \\ &\quad \left. + \eta_d (1 - \eta_d) \eta_f^2 P_{\text{dark}} P_{\text{phot}}^2 + \eta_f^2 (1 - \eta_d)^2 P_{\text{phot}}^2 P_{\text{dark}}^2 \right] \end{aligned} \quad (\text{D.10})$$

$$\beta_2 = \alpha_2 + \frac{(1 - P_{\text{dark}})^2}{P_{\text{2click}}} \left[\eta_d (1 - \eta_d) \eta_f^2 P_{\text{dark}} P_{\text{phot}}^2 + \eta_f^2 (1 - \eta_d)^2 P_{\text{phot}}^2 P_{\text{dark}}^2 \right]. \quad (\text{D.11})$$

The success probability P_{2click} is

$$\begin{aligned} P_{\text{2click}} &= (1 - P_{\text{dark}})^2 \left[\frac{1}{2} \eta_d^2 \eta_f^2 P_{\text{phot}}^2 + 4\eta_d \eta_f (1 - \eta_d \eta_f) P_{\text{dark}} P_{\text{phot}}^2 + 4P_{\text{dark}}^2 (1 - P_{\text{dark}})^2 \right. \\ &\quad + 4\eta_d \eta_f P_{\text{dark}} P_{\text{phot}} (1 - P_{\text{phot}}) + 4(1 - \eta_d \eta_f)^2 P_{\text{phot}}^2 P_{\text{dark}}^2 \\ &\quad \left. + 8(1 - \eta_d \eta_f) P_{\text{phot}} (1 - P_{\text{phot}}) P_{\text{dark}}^2 \right] \end{aligned} \quad (\text{D.12})$$

As in the single-photon scheme, we have not assumed number resolving detectors and we have assumed that with probability $(1 - P_{\text{phot}})$, an emitter spontaneously decay to one of the ground states resulting in the state $\frac{1}{2}(|0\rangle\langle 0| + |1\rangle\langle 1|)$.

D.3 Deterministic CNOT gate

Here we describe the local entanglement generation scheme presented in Ref. [86], which can be used to make a deterministic CNOT gate as described in Section 5.3.3.

We assume that weak coherent light is continuously shined onto the cavity such that at most one photon is in the cavity at all times. A single-photon detector continuously monitors if any photons are reflected from the cavity and the coherent light is blocked if a click is recorded before n_{max} photons on average have been sent onto the cavity. If no click was recorded during this time, both atoms are interpreted as being in the g levels. The steps of the entangling scheme are the following.

1. Both atoms are initially prepared in the superposition $|g\rangle + |f\rangle$ by e.g. a $\pi/2$ -pulse.
2. Coherent light is sent onto the cavity. If a click is recorded before on average n_{max} photons have been sent onto the cavity, the levels of the atoms are flipped ($|g\rangle \leftrightarrow |f\rangle$). If no click is recorded, the atoms are interpreted as being in $|gg\rangle$ and the procedure is repeated from step 1.
3. Conditioned on the first click, another coherent light pulse is sent onto the cavity after the levels of the atoms have been flipped. If a click is recorded before $n = n_{max} - n_1$ photons on average have been sent onto the cavity, the entangling scheme is considered to be a success. Here n_1 is the average number of photons that had been sent onto the cavity before the first click. If no click is recorded, the atoms are interpreted as being in $|gg\rangle$ and the procedure is repeated from step 1.

As described above, the entangling scheme is repeated until it is successful leading to a deterministic creation of entanglement in the end. As described in Ref. [85] a series of non-destructive measurements of the atoms together with single qubit rotations

can be used to make a CNOT operation after the entanglement has been created. The non-destructive measurements can be performed using the same technique of monitoring reflected light as in the entangling scheme and we assume that we can effectively tune the couplings to the cavity such that possibly only a single atom couples.

D.4 Rate analysis

Here we analyse the rate of entanglement distribution for the different repeater architectures considered in the main text. The total rate of the repeater is set by the average time of entanglement creation, initial purification and entanglement swapping. Assuming that entanglement generation has a success probability, P_0 , we estimate the average time $\tau_{\text{pair},l;m}$ it takes to generate l entangled pairs in one elementary link using m qubits, which can be operated in parallel, as

$$\tau_{\text{pair},l;m} = \mathcal{Z}_{l;m}(P_0)(L_0/c + \tau_{\text{local}}). \quad (\text{D.13})$$

Here c is the speed of light in the fibers and τ_{local} is the time of local operations such as initialization of the qubits. The factor $\mathcal{Z}_{l;m}(P_0)$ can be thought of as the average number of coin tosses needed to get at least l tails if we have access to m coins, which we can flip simultaneously and the probability of tail is P_0 for each coin [?]. It is furthermore assumed that coins showing tail after a toss are kept and only the coins showing head are tossed again until l tails are obtained. In the repeater context, the coins are entanglement generation attempts and tail is successful entanglement generation. The time it takes per "toss" is $L_0/c + \tau_{\text{local}}$. To calculate the expressions

for $Z_{l;m}(P_0)$, we follow the lines of Ref. [?] where similar factors are derived. The expression for $\mathcal{Z}_{m;m}(p)$ is already derived in Ref. [?] and their result is stated below

$$\mathcal{Z}_{m;m} = \sum_{k=1}^m \binom{m}{k} \frac{(-1)^{k+1}}{1 - (1-p)^k}. \quad (\text{D.14})$$

For $\mathcal{Z}_{l;m}$ where $l \neq m$, we only need to find expressions for $\mathcal{Z}_{1;m}$ with $m = 1, 2, 3, 4$, $\mathcal{Z}_{2;m}$ with $m = 3, 4$ and $\mathcal{Z}_{3;4}$ since we have a maximum of 4 qubits pr. repeater station. For $\mathcal{Z}_{2;3}$, we have that

$$\begin{aligned} \mathcal{Z}_{2;3} = & \binom{3}{3} \sum_{k=1}^{\infty} k(q^3)^{k-1} p^3 + \binom{3}{2} \sum_{k=1}^{\infty} k(q^3)^{k-1} p^2 q \\ & + \binom{3}{1} \binom{2}{1} \sum_{k=1}^{\infty} \sum_{l=1}^{\infty} (k+l)[(q^3)^{k-1} pq^2][(q^2)^{l-1} pq] \\ & + \binom{3}{1} \binom{2}{2} \sum_{k=1}^{\infty} \sum_{l=1}^{\infty} (k+l)[(q^3)^{k-1} pq^2][(q^2)^{l-1} p^2], \end{aligned} \quad (\text{D.15})$$

where $q = 1 - p$. The first term in Eq. (D.15) describes the situations where three tails are obtained in a single toss after a given number of tosses, where all coins showed head. We will refer tosses where all coins show tail as failed tosses. The second term describes the situation where we get two tails in the same toss after a given number of failed tosses. The third and fourth terms are where we get a single tail after a given number of failed tosses. The coin showing tail is then kept and the two remaining coins are tossed until we obtain another tail (third term) or two tails simultaneously (fourth term). The geometric series in Eq. (D.15) can be solved to give

$$\mathcal{Z}_{2;3} = \frac{5 - (7 - 3p)}{(2 - p)p(3 + (p - 3)p)} \approx \frac{5}{6p}, \quad (\text{D.16})$$

where the approximate expression is for $p \ll 1$. Note that the factor of $\frac{5}{6}$ corresponds to a simple picture where it on average takes $\frac{1}{3} \frac{1}{p}$ attempts to get the first 'tail' using

3 coins and $\frac{1}{2} \frac{1}{p}$ attempts to get the second using the remaining 2 coins. In a similar manner, we find that

$$\mathcal{Z}_{1;2} = \frac{1}{2p - p^2} \approx \frac{1}{2p} \quad (\text{D.17})$$

$$\mathcal{Z}_{1;3} = \frac{1}{3p - 3p^2 + p^3} \approx \frac{1}{3p} \quad (\text{D.18})$$

$$\mathcal{Z}_{1;4} = \frac{1}{4p - 6p^2 + 4p^3 - p^4} \approx \frac{1}{4p} \quad (\text{D.19})$$

$$\mathcal{Z}_{2;4} = \frac{-7 + p(15 + p(4p - 13))}{(p - 2)p(3 + (p - 3)p)(2 + (p - 2)p)} \approx \frac{7}{12p} \quad (\text{D.20})$$

$$\mathcal{Z}_{3;4} = \frac{-13 + p(33 + p(22p - 6p^2 - 37))}{(p - 2)p(3 + (p - 3)p)(2 + (p - 2)p)} \approx \frac{13}{12p}. \quad (\text{D.21})$$

Here the approximate expressions are all for $p \ll 1$ and they correspond to the expressions one would get using simple pictures similar to the one described above in the discussion of $\mathcal{Z}_{2;3}$.

After creating a number of entangled pairs in an elementary link of the repeater, they may be combined to create a purified pair of higher fidelity. As previously mentioned, we assume an entanglement pumping scheme since this requires less qubit resources than a cascading scheme. Let $P_{\text{pur}}(F_0, F_0)$ denote the success probability of the purification operation, which depends on the fidelity of the two initial pairs (F_0) and the fidelity of the CNOT gate used in the purification operation. Note that P_{pur} also contains the success probability of the CNOT gate used in the purification for the heralded gate. We estimate the average time $\tau_{\text{pur},1}$, it takes to make one purified pair from two initial pairs of fidelity F_0 , using m qubits in parallel in the entanglement generation step, as

$$\tau_{\text{pur},1} = \frac{\tau_{\text{pair},2;m} + \tau_{\text{pur}}}{P_{\text{pur}}(F_0, F_0)}, \quad (\text{D.22})$$

where $\tau_{\text{pur}} \sim L_0/c + \tau_c$ is the time of the purification operation including the classical

communication time required to compare results. Here τ_c is the time of the CNOT operation and L_0/c is the communication time between the two repeater stations sharing the entangled pairs. To further pump the entanglement of the purified pair, a new entangled pair is subsequently created using $m - 1$ qubits operated in parallel. The average time it takes to make j rounds of purification is thus estimated as

$$\tau_{\text{pur},j} = \frac{\tau_{\text{pur},j-1} + \tau_{\text{pur}} + \tau_{\text{pair},1:m-1}}{P_{\text{pur}}(F_{j-1}, F_0)}, \quad (\text{D.23})$$

with $\tau_{\text{pur},0} = \tau_{\text{pair},2;m} - \tau_{\text{pair},1:m-1}$. Here F_{j-1} is the fidelity of the purified pair after $j-1$ purifications. The total rate of a repeater, consisting both of purification and entanglement swapping, depends on the specific repeater architecture. We will first consider the case of both a parallel and sequential repeater operated with deterministic gates and afterwards the same situations with probabilistic gates.

D.4.1 Deterministic gates

For a parallel repeater with n swap levels and deterministic gates, we first estimate the average time it takes to generate 2^n purified pairs, i.e. a purified pair in each elementary link. We assume that each pair is purified j times such that the time to generate one purified pair is

$$\begin{aligned} \tau_{\text{pur},j} &= \frac{\mathcal{Z}_{2;m}(P_0)(L_0/c + \tau_{\text{local}})}{P_{\text{pur}}(F_0, F_0) \cdots P_{\text{pur}}(F_{j-1}, F_0)} + \sum_{i=0}^{j-1} \frac{\tau_{\text{pur}}}{P_{\text{pur}}(F_i, F_0) \cdots P_{\text{pur}}(F_{j-1}, F_0)} \\ &\quad + \sum_{i=1}^{j-1} \frac{\mathcal{Z}_{1;m-1}(P_0)(L_0/c + \tau_{\text{local}})}{P_{\text{pur}}(F_i, F_0) \cdots P_{\text{pur}}(F_{j-1}, F_0)}, \end{aligned} \quad (\text{D.24})$$

where we have solved the recurrence in Eq. (D.23). We now wish to estimate the total time, $\tau_{\text{link},2^n}$ it takes to make purification in every elementary link, i.e. the time

it takes to make 2^n pairs. A lower limit of $\tau_{\text{link},2^n}$ is simply $\tau_{\text{pur},j}$ but this is a very crude estimate if the purification have a limited success probability since the time is not determined by the average time but by the average time for the last link to succeed. We therefore make another estimate of the average time by treating $\tau_{\text{pur},j}$ as consisting of $2j$ independent binomial events with probabilities

$$P_1 = \frac{P_{\text{pur}}(F_0, F_0) \cdots P_{\text{pur}}(F_{j-1}, F_0)}{\mathcal{Z}_{2;m}(P_0)} \quad (\text{D.25})$$

$$P_2^{(i)} = P_{\text{pur}}(F_i, F_0) \cdots P_{\text{pur}}(F_{j-1}, F_0) \quad (\text{D.26})$$

$$P_3^{(i)} = \frac{P_{\text{pur}}(F_i, F_0) \cdots P_{\text{pur}}(F_{j-1}, F_0)}{\mathcal{Z}_{1;m-1}(P_0)}. \quad (\text{D.27})$$

We then estimate the average time, $\tau_{\text{link},2^n}$ it takes to make 2^n purified pairs as

$$\begin{aligned} \tau_{\text{link},2^n} &= \mathcal{Z}_{2^n;2^n}(P_1)(L_0/c + \tau_{\text{local}}) + \sum_{i=0}^{j-1} \mathcal{Z}_{2^n,2^n}(P_2^{(i)})\tau_{\text{pur}} \\ &\quad + \sum_{i=1}^{j-1} \mathcal{Z}_{2^n,2^n}(P_3^{(i)})(L_0/c + \tau_{\text{local}}). \end{aligned} \quad (\text{D.28})$$

Eq. (D.28) is a better estimate for the average time than $\tau_{\text{pur},j}$ in the limit of small success probabilities since it takes into account that we need success in all links. This is contained in the factors $\mathcal{Z}_{2^n;2^n}$. However, it overestimates the average distribution time when the purification has a large success probability. How much it overestimates depends on n and j . Comparing $\tau_{\text{pur},j}$ to Eq. (D.28) we find numerically that for $n \leq 5$ and $j \leq 2$ there is a factor $\lesssim 2$ between the two estimates, in the limit of large success probability for the purification operation. As discussed in Sec. 5.4 we never consider more than 5 swap levels in our optimization and since we have a limited number of qubits pr. repeater station, we will never have to consider more than 2 rounds of purification. We can therefore use the estimate for $\tau_{\text{link},2^n}$ given in Eq. (D.28).

To get the average time it takes to distribute one entangled pair over the total distance, L_{tot} , of the repeater, we need to add the time of the entanglement swapping, $\tau_{swap,nd}$ to $\tau_{link,2^n}$. We estimate $\tau_{swap,n}$ as

$$\tau_{swap,n} = (2^n - 1)L_0/c + n\tau_c, \quad (\text{D.29})$$

where the first term is the time of the classical communication and τ_c is the time of the CNOT operation involved in the swap procedure. The average distribution rate, of a parallel repeater with deterministic gates, is thus $r = 1/(\tau_{link,2^n} + \tau_{swap,n})$.

For a repeater using sequential entanglement creation with deterministic gates, we estimate the time it takes to generate purified pairs in all 2^n pairs as

$$\tau_{link,2^n}^{(s)} = (\tau_{link,2^{n-1}})|_{m \rightarrow 2m} + (\tau_{link,2^{n-1}})|_{m \rightarrow 2m-1}. \quad (\text{D.30})$$

Here we have indicated that the number of qubits, which can be operated in parallel is $2m$ for the first 2^{n-1} pairs and $2m - 1$ for the next 2^{n-1} pair compared to the parallel repeater, where only m qubits can be used in all 2^n pairs. Note, that we have assumed that first entanglement is established in half of the links and only when this is completed, entanglement is created in the remaining half of the links. This is clearly not the fastest way of operating the repeater but it gives an upper limit of the average distribution time and hence a lower limit on the rate. The entanglement swapping of the sequential repeater is exactly the same as for the parallel repeater and the average total rate, of the sequential repeater with deterministic gates, is thus $r = 1/(\tau_{link,2^n}^{(s)} + t_{swap,n})$.

D.4.2 Probabilistic gates

To estimate the total, average distribution time of a repeater using parallel entanglement creation with n swap levels and probabilistic gates, we will again treat $\tau_{\text{pur},j}$ as consisting of $2j$ independent binomial events, as we did for the deterministic gates. The time it takes to make a single swap can be estimated as

$$\begin{aligned}\tau_{\text{swap},1} &= \frac{\mathcal{Z}_{2;2}(P_1)(L_0/c + \tau_{\text{local}})}{P_{\text{swap}}} + \frac{L_0/c}{P_{\text{swap}}} + \frac{\tau_c}{P_{\text{swap}}} \\ &+ \sum_{i=0}^{j-1} \frac{\mathcal{Z}_{2;2}(P_2^{(i)})\tau_{\text{pur}}}{P_{\text{swap}}} + \sum_{i=1}^j \frac{\mathcal{Z}_{2;2}(P_3^{(i)})(L_0/c + \tau_{\text{local}})}{P_{\text{swap}}},\end{aligned}\quad (\text{D.31})$$

where P_{swap} is the probability of the swap operation, i.e. the probability of the CNOT gate. Eq. (D.31) can be iterated such that the average time it takes to make n swap levels is estimated as

$$\begin{aligned}\tau_{\text{swap},n} &= \frac{\tilde{\mathcal{Z}}_{n;1}(P_{\text{swap}}, P_1)(L_0/c + \tau_{\text{local}})}{P_{\text{swap}}} + \sum_{i=1}^n \frac{\tilde{\mathcal{Z}}_{n;i}(P_{\text{swap}}, P_{\text{swap}})(2^{i-1}L_0/c + \tau_c)}{P_{\text{swap}}} \\ &+ \sum_{i=0}^{j-1} \frac{\tilde{\mathcal{Z}}_{n;1}(P_{\text{swap}}, P_2^{(i)})\tau_{\text{pur}}}{P_{\text{swap}}} + \sum_{i=1}^{j-1} \frac{\tilde{\mathcal{Z}}_{n;1}(P_{\text{swap}}, P_3^{(i)})(L_0/c + \tau_{\text{local}})}{P_{\text{swap}}},\end{aligned}\quad (\text{D.32})$$

where

$$\tilde{\mathcal{Z}}_{n;i}(P_{\text{swap}}, P) = \mathcal{Z}_{2;2} \left(\frac{P_{\text{swap}}}{\tilde{\mathcal{Z}}_{n-1;i}(P_{\text{swap}}, P)} \right), \quad (\text{D.33})$$

$$\tilde{\mathcal{Z}}_{i;i}(P_{\text{swap}}, P) = \mathcal{Z}_{2;2}(P) \quad (\text{D.34})$$

$$\tilde{\mathcal{Z}}_{i;i}(P_{\text{swap}}, P_{\text{swap}}) = 1. \quad (\text{D.35})$$

Here P is either P_1 , $P_2^{(i)}$ or $P_3^{(i)}$. In the limit of $P_0, P_{\text{swap}} \ll 1$ and assuming no initial purification, Eq. (D.32) reduces to the well-known formula [?, ?]

$$\tau_{\text{swap},n} = \frac{(3/2)^n (L_0/c + \tau_{\text{local}})}{P_0 P_{\text{swap}}^n}, \quad (\text{D.36})$$

since $\mathcal{Z}_{2;2}(P \ll 1) \approx 3/(2P)$ and the time of local operations in the swaps can be neglected in this limit. However, for higher success probabilities, Eq. (D.32) more accurately estimates the average distribution time. The average rate of a parallel repeater with probabilistic gates and n swap levels is then $r = 1/\tau_{\text{swap},n}$. From a numerical study, we again find that for $P_{\text{swap}} \approx 1$ and $P_0 \ll 1$, Eq. (D.32) underestimates the average distribution rate with a factor that increases with the number of swap levels, n . However, for $n \leq 5$ and $j \leq 2$, we find that this factor is $\lesssim 2$.

The operation of a sequential repeater with probabilistic gates is not straightforward since it is unclear how the sequential generation of entanglement should take place after a failed swap operation. We therefore choose to assume that initially, entanglement is generated in all 2^n links sequentially. When this is completed the first round of entanglement swapping is performed. If a swap fails, entanglement is restored in a parallel manner in this section, i.e. the sequential operation is only employed in the initial generation of entanglement. Thus if i 'th swaps fail in the first swap level an extra waiting time of

$$\begin{aligned} & \mathcal{Z}_{i;i} \left(\frac{P_{\text{swap}}}{\mathcal{Z}_{2;2}(P_1)} \right) (L_0/c + \tau_{\text{local}}) + \mathcal{Z}_{i;i}(P_{\text{swap}})(L_0/c + \tau_c) \\ & + \sum_{k=0}^{j-1} \mathcal{Z}_{i;i} \left(\frac{P_{\text{swap}}}{\mathcal{Z}_{2;2}(P_2^{(k)})} \right) \tau_{\text{pur}} + \sum_{k=1}^{j-1} \mathcal{Z}_{i;i} \left(\frac{P_{\text{swap}}}{\mathcal{Z}_{2;2}(P_3^{(k)})} \right) (L_0/c + \tau_{\text{local}}) \end{aligned} \quad (\text{D.37})$$

is needed to restore entanglement in the $2i$ 'th links in a parallel manner and swap them successfully. Eq. (D.37) is very similar to Eq. (D.31), which estimates the time needed for a single swap at the first swap level. Nonetheless, the functions $\mathcal{Z}_{i;i}$, which appears in Eq. (D.37) takes into account that we need i successful swaps instead of only a single swap. Furthermore, we assume that the swap operations of a swap level is only initiated when all swap operations in the preceeding level have been successful.

The average time, it takes for all swap operations in the first level to succeed, is then estimated as

$$\begin{aligned} \tau_{\text{swap},1}^{(s)} = & \sum_{i=0}^{2^{n-1}} P_{\text{swap}}^{2^{n-1}-i} (1 - P_{\text{swap}})^i \left[\mathcal{Z}_{i;i} \left(\frac{P_{\text{swap}}}{\mathcal{Z}_{2;2}(P_1)} \right) (L_0/c + \tau_{\text{local}}) \right. \\ & + \mathcal{Z}_{i;i}(P_{\text{swap}})(L_0/c + \tau_c) + \sum_{k=0}^{j-1} \mathcal{Z}_{i;i} \left(\frac{P_{\text{swap}}}{\mathcal{Z}_{2;2}(P_2^{(k)})} \right) \tau_{\text{pur}} \\ & \left. + \sum_{k=1}^{j-1} \mathcal{Z}_{i;i} \left(\frac{P_{\text{swap}}}{\mathcal{Z}_{2;2}(P_3^{(k)})} \right) (L_0/c + \tau_{\text{local}}) + (L_0/c + \tau_c) \delta_{i,0} \right], \quad (\text{D.38}) \end{aligned}$$

where $\delta_{i,0}$ is the Kronecker delta symbol and $\mathcal{Z}_{0;0} = 0$. It is seen that in the limit $P_{\text{swap}} \rightarrow 1$, Eq. (D.38) correctly reduces to $\tau_{\text{swap},1}^{(s)} = L_0/c + \tau_c$, which simply is the time of the classical communication of the results of the bell measurements and the time of the local operations. Eq. (D.38) can be generalized such that the time it takes to perform the l 'th swap level is

$$\begin{aligned} \tau_{\text{swap},l}^{(s)} = & \sum_{i=0}^{2^{n-l}} P_{\text{swap}}^{2^{n-l}-i} (1 - P_{\text{swap}})^i \left[\mathcal{Z}_{i;i} \left(\frac{P_{\text{swap}}}{\tilde{\mathcal{Z}}_{l;1}(P_{\text{swap}}, P_1)} \right) (L_0/c + \tau_{\text{local}}) \right. \\ & + \sum_{k=1}^l \mathcal{Z}_{i;i} \left(\frac{P_{\text{swap}}}{\tilde{\mathcal{Z}}_{l;k}(P_{\text{swap}}, P_{\text{swap}})} \right) (2^{k-1}L_0/c + \tau_c) \\ & + \sum_{k=0}^{j-1} \mathcal{Z}_{i;i} \left(\frac{P_{\text{swap}}}{\tilde{\mathcal{Z}}_{l;1}(P_{\text{swap}}, P_2^{(k)})} \right) \tau_{\text{pur}} \\ & + \sum_{k=1}^{j-1} \mathcal{Z}_{i;i} \left(\frac{P_{\text{swap}}}{\tilde{\mathcal{Z}}_{l;1}(P_{\text{swap}}, P_3^{(k)})} \right) (L_0/c + \tau_{\text{local}}) \\ & \left. + (2^{l-1}L_0/c + \tau_c) \delta_{i,0} \right], \quad (\text{D.39}) \end{aligned}$$

which can be compared to Eq. (D.32) which estimates the time to make a successful swap at the n 'th level (let $n \rightarrow l$ for comparison). Once again the functions $\mathcal{Z}_{i;i}$ takes into account that we need i 'th successful swaps instead of just a single successful swap. The total rate of a sequential repeater with probabilistic gates and n swap

levels can then be estimated as $r = 1/(\tau_{\text{link},2^n}^{(s)} + \tau_{\text{swap},1}^{(s)} + \dots + \tau_{\text{swap},n}^{(s)})$.

Bibliography

- [1] U Akram, N Kiesel, M Aspelmeyer, and G J Milburn. Single-photon optomechanics in the strong coupling regime. *New Journal of Physics*, 12(8):083030, 2010.
- [2] O. Arcizet, P.-F. Cohadon, T. Briant, M. Pinard, and A. Heidmann. Radiation-pressure cooling and optomechanical instability of a micromirror. *Nature*, 444:71–74, 2006.
- [3] Markus Aspelmeyer and Keith Schwab. Focus on mechanical systems at the quantum limit. *New Journal of Physics*, 10(9):095001, 2008.
- [4] S Basiri-Esfahani, U Akram, and G J Milburn. Phonon number measurements using single photon opto-mechanics. *New Journal of Physics*, 14(8):085017, 2012.
- [5] Almut Beige, Daniel Braun, Ben Tregenna, and Peter L. Knight. Quantum computing using dissipation to remain in a decoherence-free subspace. *Phys. Rev. Lett.*, 85:1762–1765, Aug 2000.
- [6] J Borregaard, P. Kómár, E. M. Kessler, M. D. Lukin, and A. S. Sørensen. Long-distance entanglement distribution using individual atoms in optical cavities. *Physical Review A*, 92(1):012307, July 2015.
- [7] R. J. Brecha, P. R. Rice, and M. Xiao. n two-level atoms in a driven optical cavity: Quantum dynamics of forward photon scattering for weak incident fields. *Phys. Rev. A*, 59:2392–2417, Mar 1999.
- [8] Ferdinand Brennecke, Stephan Ritter, Tobias Donner, and Tilman Esslinger. Cavity optomechanics with a bose-einstein condensate. *Science*, 322(5899):235–238, 2008.
- [9] H.-J. Briegel, W. Dür, J. I. Cirac, and P. Zoller. Quantum repeaters: The role of imperfect local operations in quantum communication. *Phys. Rev. Lett.*, 81:5932–5935, Dec 1998.

- [10] Michael J. Burek, Yiwen Chu, Madelaine S. Z. Liddy, Parth Patel, Jake Rochman, Srujan Meesala, Wooyoung Hong, Qimin Quan, Mikhail D. Lukin, and Marko Loncar. High quality-factor optical nanocavities in bulk single-crystal diamond. *Nature Communications*, 5:5718, 2014.
- [11] H.J. Carmichael, R.J. Brecha, and P.R. Rice. Quantum interference and collapse of the wavefunction in cavity {QED}. *Optics Communications*, 82(12):73 – 79, 1991.
- [12] Tal Carmon and Kerry J. Vahala. Modal spectroscopy of optoexcited vibrations of a micron-scale on-chip resonator at greater than 1 ghz frequency. *Phys. Rev. Lett.*, 98:123901, Mar 2007.
- [13] Jasper Chan, T. P. Mayer Alegre, Amir H. Safavi-Naeini, Jeff T. Hill, Alex Krause, Simon Gröblacher, Markus Aspelmeyer, and Oskar Painter. Laser cooling of a nanomechanical oscillator into its quantum ground state. *Nature*, 478:89–92, 2011.
- [14] Jasper Chan, Amir H. Safavi-Naeini, Jeff T. Hill, Sen Meenehan, and Oskar Painter. Optimized optomechanical crystal cavity with acoustic radiation shield. *Applied Physics Letters*, 101(8):081115, 2012.
- [15] D E Chang, A H Safavi-Naeini, M Hafezi, and O Painter. Slowing and stopping light using an optomechanical crystal array. *New Journal of Physics*, 13(2):023003, 2011.
- [16] Darrick E. Chang, Anders S. Sørensen, Eugene A. Demler, and Mikhail D. Lukin. A single-photon transistor using nanoscale surface plasmons. *Nature Physics*, 3:807–812, 2007.
- [17] H. K. Cheung and C. K. Law. Nonadiabatic optomechanical hamiltonian of a moving dielectric membrane in a cavity. *Phys. Rev. A*, 84:023812, Aug 2011.
- [18] Lilian Childress, Ronald Walsworth, and Mikhail Lukin. Atom-like crystal defects: From quantum computers to biological sensors. *Physics Today*, 67:38, 2014.
- [19] J. I. Cirac, P. Zoller, H. J. Kimble, and H. Mabuchi. Quantum state transfer and entanglement distribution among distant nodes in a quantum network. *Phys. Rev. Lett.*, 78:3221–3224, Apr 1997.
- [20] Thomas Corbitt, Christopher Wipf, Timothy Bodiya, David Ottaway, Daniel Sigg, Nicolas Smith, Stanley Whitcomb, and Nergis Mavalvala. Optical dilution and feedback cooling of a gram-scale oscillator to 6.9 mk. *Phys. Rev. Lett.*, 99:160801, Oct 2007.

- [21] Marcelo Davanço, Jasper Chan, Amir H. Safavi-Naeini, Oskar Painter, and Kartik Srinivasan. Slot-mode-coupled optomechanical crystals. *Opt. Express*, 20(22):24394–24410, Oct 2012.
- [22] L. Ding, C. Baker, P. Senellart, A. Lemaitre, S. Ducci, G. Leo, and I. Favero. Wavelength-sized gaas optomechanical resonators with gigahertz frequency. *Applied Physics Letters*, 98(11):113108, 2011.
- [23] J. M. Dobrindt and T. J. Kippenberg. Theoretical analysis of mechanical displacement measurement using a multiple cavity mode transducer. *Phys. Rev. Lett.*, 104:033901, Jan 2010.
- [24] L.-M. Duan and H. J. Kimble. Scalable photonic quantum computation through cavity-assisted interactions. *Phys. Rev. Lett.*, 92:127902, Mar 2004.
- [25] L.-M. Duan and H. J. Kimble. Scalable photonic quantum computation through cavity-assisted interactions. *Phys. Rev. Lett.*, 92:127902, Mar 2004.
- [26] L.-M. Duan, M. D. Lukin, J. I. Cirac, and P. Zoller. Long-distance quantum communication with atomic ensembles and linear optics. *Nature*, 414:413–418, 2001.
- [27] L.-M. Duan, B. Wang, and H. J. Kimble. Robust quantum gates on neutral atoms with cavity-assisted photon scattering. *Phys. Rev. A*, 72:032333, Sep 2005.
- [28] Matt Eichenfield, Jasper Chan, Ryan M. Camacho, Kerry J. Vahala, and Oskar Painter. Optomechanical crystals. *Nature*, 462:78–82, 2009.
- [29] Ivan Favero and Khaled Karrai. Optomechanics of deformable optical cavities. *Nature Photonics*, 3:201–205, 2009.
- [30] Richard P. Feynman. Simulating physics with computers. *International Journal of Theoretical Physics*, 21(6-7):467–488, 1982.
- [31] Victor Fiore, Yong Yang, Mark C. Kuzyk, Russell Barbour, Lin Tian, and Hailin Wang. Storing optical information as a mechanical excitation in a silica optomechanical resonator. *Phys. Rev. Lett.*, 107:133601, Sep 2011.
- [32] C. Gardiner and P. Zoller. *Quantum Noise*. Springer, 2004.
- [33] C. Genes, A. Mari, D. Vitali, and P. Tombesi. Chapter 2 quantum effects in optomechanical systems. In *Advances in Atomic Molecular and Optical Physics*, volume 57 of *Advances In Atomic, Molecular, and Optical Physics*, pages 33 – 86. Academic Press, 2009.

- [34] S. Gigan, H. R. Bhm, M. Paternostro, F. Blaser, G. Langer, J. B. Hertzberg, K. C. Schwab, D. Buerle, M. Aspelmeyer, and A. Zeilinger. Self-cooling of a micromirror by radiation pressure. *Nature*, 444:67–70, 2006.
- [35] V. Giovannetti, D. Vitali, P. Tombesi, and A. Ekert. Scalable quantum computation with cavity qed systems. *Phys. Rev. A*, 62:032306, Aug 2000.
- [36] M. Grassl, Th. Beth, and T. Pellizzari. Codes for the quantum erasure channel. *Phys. Rev. A*, 56:33–38, Jul 1997.
- [37] Simon Gröblacher, Klemens Hammerer, Michael R. Vanner, and Markus Aspelmeyer. Observation of strong coupling between a micromechanical resonator and an optical cavity field. *Nature*, 460:724–727, 2009.
- [38] Ivan S. Grudinin, Hansuek Lee, O. Painter, and Kerry J. Vahala. Phonon laser action in a tunable two-level system. *Phys. Rev. Lett.*, 104:083901, Feb 2010.
- [39] Subhadeep Gupta, Kevin L. Moore, Kater W. Murch, and Dan M. Stamper-Kurn. Cavity nonlinear optics at low photon numbers from collective atomic motion. *Phys. Rev. Lett.*, 99:213601, Nov 2007.
- [40] Jeff T. Hill, Amir H. Safavi-Naeini, Jasper Chan, and Oskar Painter. Coherent optical wavelength conversion via cavity optomechanics. *Nature Communications*, 3:1196, 2012.
- [41] J.R. Johansson, P.D. Nation, and Franco Nori. Qutip 2: A python framework for the dynamics of open quantum systems. *Computer Physics Communications*, 184(4):1234 – 1240, 2013.
- [42] M. J. Kastoryano, F. Reiter, and A. S. Sørensen. Dissipative preparation of entanglement in optical cavities. *Phys. Rev. Lett.*, 106:090502, Feb 2011.
- [43] E. M. Kessler, P. Kómár, M. Bishof, L. Jiang, a. S. Sørensen, J. Ye, and M. D. Lukin. Heisenberg-limited atom clocks based on entangled qubits. *Physical Review Letters*, 112(May):190403, 2014.
- [44] H. J. Kimble. The quantum internet. *Nature*, 453:1023–1030, 2008.
- [45] T. J. Kippenberg and K. J. Vahala. Cavity optomechanics: Back-action at the mesoscale. *Science*, 321(5893):1172–1176, 2008.
- [46] Dustin Kleckner and Dirk Bouwmeester. Sub-kelvin optical cooling of a micromechanical resonator. *Nature*, 444:75–78, 2006.
- [47] E. Knill, R. Laflamme, and G. J. Milburn. A scheme for efficient quantum computation with linear optics. *Nature*, 409:46–52, 2001.

- [48] P. Kómár, E. M. Kessler, M. Bishof, L. Jiang, a. S. Sørensen, J. Ye, and M. D. Lukin. A quantum network of clocks. *Nature Physics*, 10(June):582–587, 2014.
- [49] Andreas Kronwald, Max Ludwig, and Florian Marquardt. Full photon statistics of a light beam transmitted through an optomechanical system. *Phys. Rev. A*, 87:013847, Jan 2013.
- [50] Axel Kuhn, Markus Hennrich, and Gerhard Rempe. Deterministic single-photon source for distributed quantum networking. *Phys. Rev. Lett.*, 89:067901, Jul 2002.
- [51] T. D. Ladd, F. Jelezko, R. Laflamme, Y. Nakamura, C. Monroe, and J. L. O'Brien. Quantum computers. *Nature*, 464:45–53, 2010.
- [52] Jie-Qiao Liao and C. K. Law. Correlated two-photon scattering in cavity optomechanics. *Phys. Rev. A*, 87:043809, Apr 2013.
- [53] Max Ludwig, Bjrn Kubala, and Florian Marquardt. The optomechanical instability in the quantum regime. *New Journal of Physics*, 10(9):095013, 2008.
- [54] Max Ludwig, Amir H. Safavi-Naeini, Oskar Painter, and Florian Marquardt. Enhanced quantum nonlinearities in a two-mode optomechanical system. *Phys. Rev. Lett.*, 109:063601, Aug 2012.
- [55] M. D. Lukin. *Colloquium : Trapping and manipulating photon states in atomic ensembles*. *Rev. Mod. Phys.*, 75:457–472, Apr 2003.
- [56] Florian Marquardt, Joe P. Chen, A. A. Clerk, and S. M. Girvin. Quantum theory of cavity-assisted sideband cooling of mechanical motion. *Phys. Rev. Lett.*, 99:093902, Aug 2007.
- [57] Florian Marquardt and Steven M. Girvin. Trend: Optomechanics. *Physics*, 2:40, 2009.
- [58] William Marshall, Christoph Simon, Roger Penrose, and Dik Bouwmeester. Towards quantum superpositions of a mirror. *Phys. Rev. Lett.*, 91:130401, Sep 2003.
- [59] P. C. Maurer, G. Kucsko, C. Latta, L. Jiang, N. Y. Yao, S. D. Bennett, F. Pastawski, D. Hunger, N. Chisholm, M. Markham, D. J. Twitchen, J. I. Cirac, and M. D. Lukin. Room-temperature quantum bit memory exceeding one second. *Science*, 336(6086):1283–1286, 2012.
- [60] Constanze Hhberger Metzger and Khaled Karrai. Cavity cooling of a microlever. *Nature*, 432:1002–1005, 2004.

- [61] Haixing Miao, Stefan Danilishin, Thomas Corbitt, and Yanbei Chen. Standard quantum limit for probing mechanical energy quantization. *Phys. Rev. Lett.*, 103:100402, Sep 2009.
- [62] M. Notomi, E. Kuramochi, and H. Taniyama. Ultrahigh-q nanocavity with 1d photonic gap. *Opt. Express*, 16(15):11095–11102, Jul 2008.
- [63] A. Nunnenkamp, K. Børkje, and S. M. Girvin. Single-photon optomechanics. *Phys. Rev. Lett.*, 107:063602, Aug 2011.
- [64] A. D. OConnell, M. Hofheinz, M. Ansmann, Radoslaw C. Bialczak, M. Lenander, Erik Lucero, M. Neeley, D. Sank, H. Wang, M. Weides, J. Wenner, John M. Martinis, and A. N. Cleland. Quantum ground state and single-phonon control of a mechanical resonator. *Nature*, 464:697–703, 2010.
- [65] Jiannis Pachos and Herbert Walther. Quantum computation with trapped ions in an optical cavity. *Phys. Rev. Lett.*, 89:187903, Oct 2002.
- [66] T. Pellizzari, S. A. Gardiner, J. I. Cirac, and P. Zoller. Decoherence, continuous observation, and quantum computing: A cavity qed model. *Phys. Rev. Lett.*, 75:3788–3791, Nov 1995.
- [67] S Perseguers, G J Lapeyre Jr, D Cavalcanti, M Lewenstein, and A Acín. Distribution of entanglement in large-scale quantum networks. *Reports on Progress in Physics*, 76(9):096001, 2013.
- [68] T. P. Purdy, D. W. C. Brooks, T. Botter, N. Brahms, Z.-Y. Ma, and D. M. Stamper-Kurn. Tunable cavity optomechanics with ultracold atoms. *Phys. Rev. Lett.*, 105:133602, Sep 2010.
- [69] P. Rabl. Photon blockade effect in optomechanical systems. *Phys. Rev. Lett.*, 107:063601, Aug 2011.
- [70] J. M. Raimond, M. Brune, and S. Haroche. Manipulating quantum entanglement with atoms and photons in a cavity. *Rev. Mod. Phys.*, 73:565–582, Aug 2001.
- [71] T. C. Ralph, A. J. F. Hayes, and Alexei Gilchrist. Loss-tolerant optical qubits. *Phys. Rev. Lett.*, 95:100501, Aug 2005.
- [72] C A Regal and K W Lehnert. From cavity electromechanics to cavity optomechanics. *Journal of Physics: Conference Series*, 264(1):012025, 2011.
- [73] Andreas Reiserer, Norbert Kalb, Gerhard Rempe, and Stephan Ritter. A quantum gate between a flying optical photon and a single trapped atom. *Nature*, 508:237–240, 2014.

- [74] Florentin Reiter and Anders S. Sørensen. Effective operator formalism for open quantum systems. *Phys. Rev. A*, 85:032111, Mar 2012.
- [75] P.R. Rice and H.J. Carmichael. Single-atom cavity-enhanced absorption. i. photon statistics in the bad-cavity limit. *Quantum Electronics, IEEE Journal of*, 24(7):1351–1366, Jul 1988.
- [76] Stephan Ritter, Christian Nölleke, Carolin Hahn, Andreas Reiserer, Andreas Neuzner, Manuel Uphoff, Martin Mücke, Eden Figueroa, Joerg Bochmann, and Gerhard Rempe. An elementary quantum network of single atoms in optical cavities. *Nature*, 484:195–200, 2012.
- [77] Jacob T. Robinson, Christina Manolatou, Long Chen, and Michal Lipson. Ultrasmall mode volumes in dielectric optical microcavities. *Phys. Rev. Lett.*, 95:143901, Sep 2005.
- [78] A. H. Safavi-Naeini, T. P. Mayer Alegre, J. Chan, M. Eichenfield, M. Winger, Q. Lin, J. T. Hill, D. E. Chang, and O. Painter. Electromagnetically induced transparency and slow light with optomechanics. *Nature*, 472:69–73, 2011.
- [79] Amir H Safavi-Naeini and Oskar Painter. Proposal for an optomechanical traveling wave phononphoton translator. *New Journal of Physics*, 13(1):013017, 2011.
- [80] S. Schiemann, A. Kuhn, S. Steuerwald, and K. Bergmann. Efficient coherent population transfer in no molecules using pulsed lasers. *Phys. Rev. Lett.*, 71:3637–3640, Nov 1993.
- [81] A. Schliesser, R. Rivière, G. Anetsberger, O. Arcizet, and T. J. Kippenberg. Resolved-sideband cooling of a micromechanical oscillator. *Nature Physics*, 4:415–419, 2008.
- [82] Michael Schmidt, Max Ludwig, and Florian Marquardt. Optomechanical circuits for nanomechanical continuous variable quantum state processing. *New Journal of Physics*, 14(12):125005, 2012.
- [83] R. J. Schoelkopf and S. M. Girvin. Wiring up quantum systems. *Nature*, 451:664–669, 2008.
- [84] Peter W. Shor. Polynomial-time algorithms for prime factorization and discrete logarithms on a quantum computer. *SIAM Journal on Computing*, 26(5):1484–1509, 1997.
- [85] Anders S. Sørensen and Klaus Mølmer. Measurement induced entanglement and quantum computation with atoms in optical cavities. *Phys. Rev. Lett.*, 91:097905, Aug 2003.

- [86] Anders S. Sørensen and Klaus Mølmer. Probabilistic generation of entanglement in optical cavities. *Phys. Rev. Lett.*, 90:127903, Mar 2003.
- [87] Dan M. Stamper-Kurn. Cavity optomechanics with cold atoms. page arXiv:1204.4351, 2012.
- [88] K. Stannigel, P. Komar, S. J. M. Habraken, S. D. Bennett, M. D. Lukin, P. Zoller, and P. Rabl. Optomechanical quantum information processing with photons and phonons. *Phys. Rev. Lett.*, 109:013603, Jul 2012.
- [89] K. Stannigel, P. Rabl, A. S. Sørensen, P. Zoller, and M. D. Lukin. Optomechanical transducers for long-distance quantum communication. *Phys. Rev. Lett.*, 105:220501, Nov 2010.
- [90] Y. Tanaka, T. Asano, and S. Noda. Design of photonic crystal nanocavity with q -factor of $\sim 10^9$. *Lightwave Technology, Journal of*, 26(11):1532–1539, June 2008.
- [91] J. M. Taylor, A. S. Sørensen, C. M. Marcus, and E. S. Polzik. Laser cooling and optical detection of excitations in a lc electrical circuit. *Phys. Rev. Lett.*, 107:273601, Dec 2011.
- [92] J. D. Teufel, T. Donner, Dale Li, J. W. Harlow, M. S. Allman, K. Cicak, A. J. Sirois, J. D. Whittaker, K. W. Lehnert, and R. W. Simmonds. Sideband cooling of micromechanical motion to the quantum ground state. *Nature*, 475:359–363, 2011.
- [93] J. D. Teufel, Dale Li, M. S. Allman, K. Cicak, A. J. Sirois, J. D. Whittaker, and R. W. Simmonds. Circuit cavity electromechanics in the strong-coupling regime. *Nature*, 471:204–208, 2011.
- [94] J. D. Thompson, T. G. Tiecke, N. P. de Leon, J. Feist, A. V. Akimov, M. Gullans, A. S. Zibrov, V. Vuletić, and M. D. Lukin. Coupling a single trapped atom to a nanoscale optical cavity. *Science*, 340(6137):1202–1205, 2013.
- [95] J. D. Thompson, B. M. Zwickl, A. M. Jayich, Florian Marquardt, S. M. Girvin, and J. G. E. Harris. Strong dispersive coupling of a high-finesse cavity to a micromechanical membrane. *Nature*, 452:72–75, 2007.
- [96] T. G. Tiecke, J. D. Thompson, N. P. de Leon, L. R. Liu, V. Vuletić, and M. D. Lukin. Nanophotonic quantum phase switch with a single atom. *Nature*, 508:241–244, 2014.
- [97] E. Togan, Y. Chu, A. S. Trifonov, L. Jiang, J. Maze, L. Childress, M. V. G. Dutt, A. S. Sørensen, P. R. Hemmer, A. S. Zibrov, and M. D. Lukin. Quantum

- entanglement between an optical photon and a solid-state spin qubit. *Nature*, 466:730–734, 2010.
- [98] Michael Varnava, Daniel E. Browne, and Terry Rudolph. Loss tolerance in one-way quantum computation via counterfactual error correction. *Phys. Rev. Lett.*, 97:120501, Sep 2006.
- [99] E. Verhagen, S. Deléglise, S. Weis, A. Schliesser, and T. J. Kippenberg. Quantum-coherent coupling of a mechanical oscillator to an optical cavity mode. *Nature*, 482:63–67, 2012.
- [100] Stefan Weis, Rmi Rivire, Samuel Delglise, Emanuel Gavartin, Olivier Arcizet, Albert Schliesser, and Tobias J. Kippenberg. Optomechanically induced transparency. *Science*, 330(6010):1520–1523, 2010.
- [101] D. J. Wilson, C. A. Regal, S. B. Papp, and H. J. Kimble. Cavity optomechanics with stoichiometric sin films. *Phys. Rev. Lett.*, 103:207204, Nov 2009.
- [102] I. Wilson-Rae, N. Nooshi, W. Zwerger, and T. J. Kippenberg. Theory of ground state cooling of a mechanical oscillator using dynamical backaction. *Phys. Rev. Lett.*, 99:093901, Aug 2007.
- [103] Chi Xiong, Wolfram H P Pernice, Xiankai Sun, Carsten Schuck, King Y Fong, and Hong X Tang. Aluminum nitride as a new material for chip-scale optomechanics and nonlinear optics. *New Journal of Physics*, 14(9):095014, 2012.
- [104] Jing Zhang, Kunchi Peng, and Samuel L. Braunstein. Quantum-state transfer from light to macroscopic oscillators. *Phys. Rev. A*, 68:013808, Jul 2003.
- [105] Mian Zhang, Gustavo S. Wiederhecker, Sasikanth Manipatruni, Arthur Barnard, Paul McEuen, and Michal Lipson. Synchronization of micromechanical oscillators using light. *Phys. Rev. Lett.*, 109:233906, Dec 2012.
- [106] Shi-Biao Zheng. Implementation of toffoli gates with a single asymmetric heisenberg xy interaction. *Phys. Rev. A*, 87:042318, Apr 2013.